Cavity Enhanced Atom Interferometry

by

Rustin Nourshargh

A thesis submitted to
the University of Birmingham
for the degree of
DOCTOR OF PHILOSOPHY

Ultracold Atoms Group
School of Physics and Astronomy
College of Engineering and Physical Sciences
the University of Birmingham

May 2021

Abstract

Atom Interferometry is a technique offering unparalleled sensitivity to a wide range of applications. Their sensitivity is currently limited by the available laser power and flatness of the optical wavefronts. We explore two solutions to these problems, high power high bandwidth operation and optical cavity enhancement.

We have demonstrated a laboratory based, high bandwidth atom interferometer instrument and have performed an incipient gravity measurement with a fractional statistical uncertainty of $\sigma_g/g = 4.4 \times 10^{-6}$ where g is the acceleration due to gravity. We have designed, constructed, and optimised a powerful Raman laser (12 W at 780 nm) which will allow large momentum transfer beamsplitters to be implemented at high bandwidth for the first time.

Cavity enhancement offers the ability to dramatically increase the laser power available for experiments, as well as filtering the spatial modes, thus improving the wavefront flatness. Difficulties in simultaneously realising large modes and spatial mode filtering, and accommodating Doppler shifts have limited the use of cavity enhancement thus far. We have designed and demonstrated a Doppler compensated optical cavity for atom interferometer enhancement. This cavity circumvents the Doppler shift limit whilst enabling mode filtering, power enhancement, and a large beam diameter simultaneously. Our novel design combines a magnified linear cavity with an intracavity Pockels cell. The Pockels cell introduces a voltage tunable birefringence, which is used to match the cavity resonances to the laser frequencies as they chirp to track Doppler shifts in the interferometer. The magnified linear geometry produces a large, 5.04 mm $1/e^2$, diameter beam waist in a 0.69 m long cavity and allows the Gouy phase to be tuned, suppressing higher order spatial modes and avoiding regions of instability. These improvements address central limitations of current cavity enhanced systems. We propose refinements to this design, further improving performance, and allowing cavity enhancement of high bandwidth systems.

The remaining limitation on cavity systems is the lifetime limit. Long, high finesse cavities have long photon lifetimes, causing severe distortion of short pulses. In proposed large scale atom interferometer based gravitational wave detectors, this appears to preclude the use of cavity enhancement. We propose a scheme for optical cavity enhanced atom interferometry, using circulating, spatially resolved pulses, and intracavity frequency modulation to overcome the cavity lifetime limit. We present parameters for the experimental realisation of the target $10^4\hbar k$ momentum separation in a 1 km interferometer using the 698 nm clock transition in ^{87}Sr, and describe potential performance enhancements in 10 m scale devices operating on the

689 nm intercombination line in ^{87}Sr. Our scheme satisfies the most challenging requirements of these sensors and paves the way for the next generation of high sensitivity, large momentum transfer atom interferometers.

Through these advancements we have laid the foundations for cavity enhancement over the full size and performance range of atom interferometers.

“Stop Wishing. Start Aligning”

ACKNOWLEDGEMENTS

Through the course of this research I have had the opportunity to work with and learn from many talented scientists. I'd like to thank my supervisors Kai Bongs and Michael Holynski for their support and advice throughout my doctorate. I am deeply indebted to Sam Hedges for his help both in and out of the lab as well as on the papers. Special thanks to all of my coauthors on both the papers Mehdi Langlois and particularly Samuel Lellouch.

I would like to thank the Cold Atoms and Interferometry teams at the University of Birmingham for making it such an interesting, friendly, and welcoming place to work with particular thanks to: Ben Stray, Farzad Hayati, Luuk Earl, Peter Hobson, Jonathan Winch, Yuhung Lien. I am grateful to Stephen Brookes and the mechanical workshop team. I'd like to thank Simon Branford for his help with computing. I'd like to thank Teressa and Agathe for all of there help in project management and navigating the university administrative functions.

I'd like to thank my supervisor at Sandia, Grant Biedermann for both his expertise and generosity with his time. I am indebted to my colleague Adrian Orozco for his significant efforts, and for making me welcome in his city. I'd also like to thank Jongmin Lee and Michael Martin for insightful discussions. I'd like to thank Shanalyn Kemme for guiding this thesis through export control.

I'd like to thank Chris Ballance, Tom Harty, and Laurent Stephenson from the University of Oxford Ion Trapping group for all of their help and support in setting up the experimental control system, and encouragement during the thesis writing. I am deeply indebted to my friend Zebedee Nichols for teaching me how to program and providing some much needed perspective.

I'd like to thank my brother Camron for giving up his summer vacation to provide engineering support in the lab. Finally I'd like to thank my parents for their continued unwavering support with everything from proof reading my thesis to technical chats about new ideas. The constant encouragement to learn new things and the opportunity to discuss them over the dinner table has made me the scientist I am today.

DECLARATION

Chapter 3 along with appendices E D F C are an adapted version of my report submitted to the university of Birmingham as a mid-course assessment, Rustin Nourshargh, "A Laboratory Atom Interferometer Instrument", 2018 [1]. The experimental work was carried out between myself and Adrian Orozco, supervised by Grant Biedermann in 2017. "The work was carried out at Sandia National Laboratories and was funded in part by Sandia through the Laboratory Directed Research and Development program. This research exchange was enabled through a collaboration between the University of Birmingham and Sandia National Laboratories[1]."

Chapters 5 and 6 are based on my first author paper: Rustin Nourshargh, Sam Hedges, Mehdi Langlois, Kai Bongs, and Michael Holynski, "Doppler compensated cavity for atom interferometry", 2020 [2]. The experimental work and modelling was conducted primarily by myself with assistance on the laser and control systems from Sam Hedges for the final three months of experimental work. I wrote the first draft of the manuscript. Figures 5.4, 6.1, 6.2, and 6.6 were modified from figures produced by Sam Hedges for the publication, all other figures are my own work. All authors contributed to reviewing and assessing the results and to the development and review of the manuscript.

Chapter 8 is based on my lead author paper with co-lead author Samuel Lellouch: Rustin Nourshargh, Samuel Lellouch, Sam Hedges, Mehdi Langlois, Kai Bongs, and Micheal Holynski, "Circulating pulse cavity enhancement as a method for extreme momentum transfer atom interferometry", 2020 [3]. I devised the circulating pulse scheme, S.L. derived the theoretical framework and code, and performed the calculations. S.H. and M.L. contributed to the LMT sequence design and Doppler shifts compensation techniques. K.B. and M.H. contributed throughout and supervised the research. All authors contributed to reviewing and assessing the results, and to the development and review of the manuscript.

---

[1] Sandia National Laboratories is a multimission laboratory managed and operated by National Technology & Engineering Solutions of Sandia, LLC, a wholly owned subsidiary of Honeywell International Inc., for the U.S. Department of Energy's National Nuclear Security Administration under contract DE-NA0003525. This document is approved for public release; further dissemination is unlimited. SAND2018-9859 R

CONTENTS

CHAPTER 1

INTRODUCTION

Atom interferometers are highly sensitive devices with a wide range of practical applications [4–6] including gravitational measurements [7–9], rotation and acceleration [10, 11], and metrology [12–14]. Current experiments are also pushing the boundaries of fundamental physics with weak equivalence principle [15–17], fine structure constant [18], gravitational constant [19–21], and dark energy [22, 23]. There are also proposals for atom interferometers based gravitational wave detectors [24–30] as they enable exploration of currently inaccessible frequency bands.

Light pulse atom interferometry exploits the quantum mechanical nature of atoms to make extremely sensitive measurements. Louis de Broglie postulated that all matter has both particle and wave properties [31]. For a cloud of laser cooled atoms, these wave-like properties can be observed and controlled though their interactions with coherent pulses of light. In an atom interferometer we use these pulses to manipulate matter waves in the same way as beamsplitters and mirrors manipulate light in an optical interferometer. The first pulse transfers every atom into a superposition of states (often atomic energy levels), imparting momentum as it does so. Each atom can now only be described as the sum of two states with differing momenta, causing them to spatially separate. These two paths are the arms in an atom interferometer. Further pulses are used to reflect and recombine the atomic superposition, whereupon these two paths interfere. This interference manifests in the state of the atoms at the output of the interferometer, oscillating between the states in original superposition as the phase difference between the two arms varies. The phase is set by a combination of the laser pulses, and the environment in which the atomic paths evolve [32, 33], resulting in an output state that is a highly sensitive probe of the environment. The output state is determined by observing the fluorescence from the atoms, under the illumination of a further laser.

The sensitivity of these instruments is maximised when the laser pulses are completed with high fidelity;

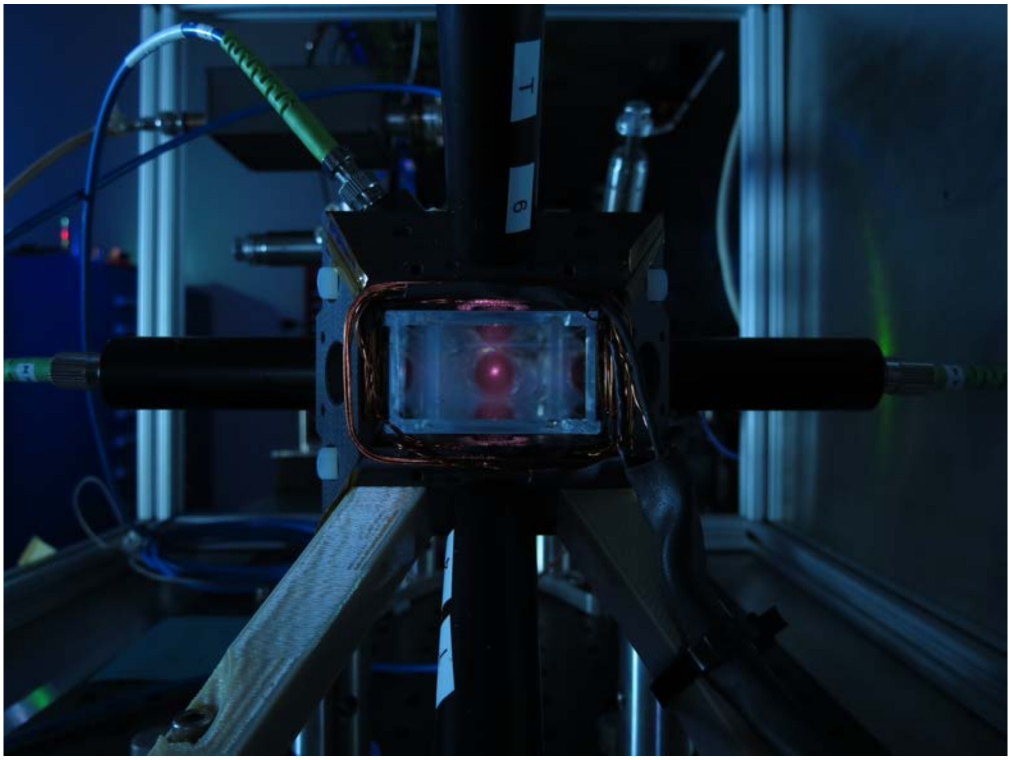

Figure 1.1: A cloud of 10^7 rubidium atoms laser cooled to $\simeq 150\ \mu$K in a magneto-optical trap at the centre of the atom interferometer presented in chapter 3.

i.e. when the pulse transfers the atoms into the target superposition. This requires high intensity laser beams with a large diameter compared to the size of the atom cloud. Both of these requirements demand high laser powers, which in experiments are limited by the cost, size, weight, and power consumption of such laser systems. For atom interferometer based sensors to substantially displace classical sensors outside of the laboratory, these optical power requirements must be addressed. High pulse fidelities also require aberration-free optical wavefronts, which are a leading cause of uncertainty in current devices [34–38].

Instrument sensitivity is improved by increasing space-time area of the interferometer [39]; that is the area enclosed between the paths through the interferometer. This is realised through longer interferometry times and increasing the momentum transferred to the atoms. As the atoms are in free-fall during interferometry, the available time is typically limited by the available free-fall distance [40], and the thermal expansion of the cloud. Increasing this distance results in larger devices, and is not a practical route to increase sensitivity in many real world applications.

Increasing the momentum transferred to the atoms (known as large momentum transfer schemes or LMT) also increases the space-time area of the interferometer, without a direct increase in the size of the device.

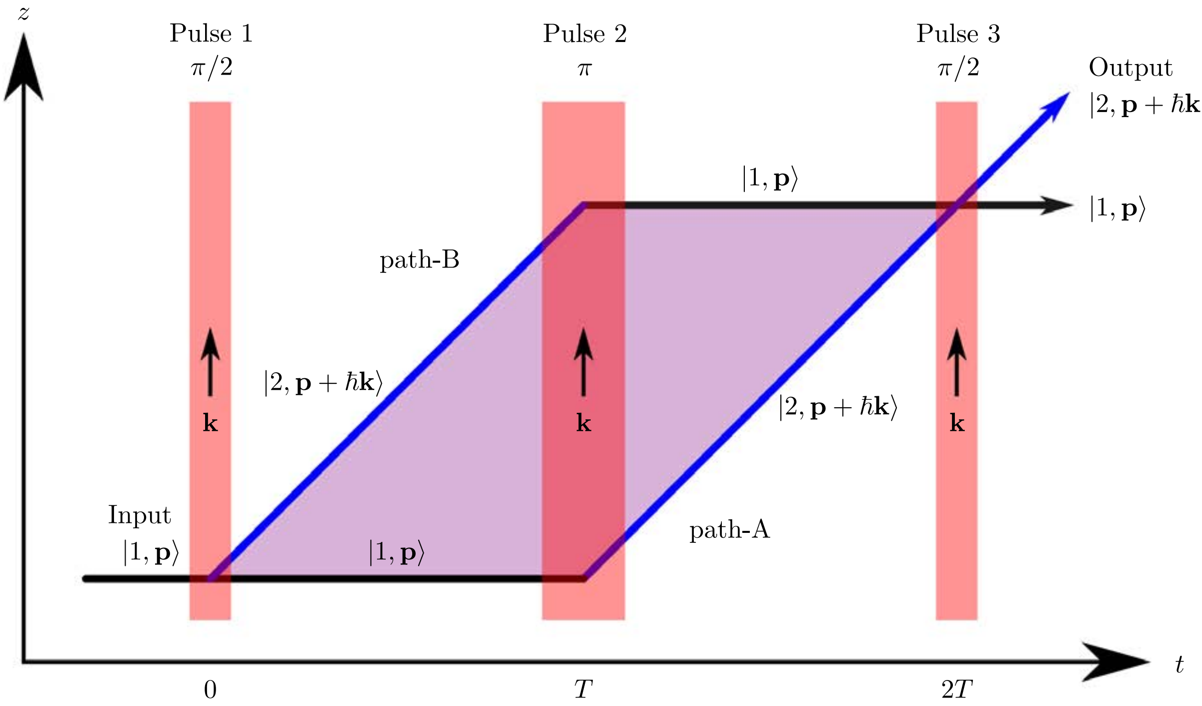

Figure 1.2: A spacetime diagram showing two paths through a three pulse atom interferometer. The enclosed space-time area is shaded in purple and laser pulses are shown in red. A detailed discussion of interferometer sensitivity is presented in chapter 2.

Momentum transfer is limited by the fidelity of the laser pulses, which as we have seen depends on the flatness of the beam profile, and the available laser power [41]. Future gravitational wave sensors will require kilometre scale baselines and momentum separations of order $10^4\hbar k$, more than an order of magnitude increase over the current state of the art [42]. This will demand larger increases in laser power and wavefront performance. The sensitivity of atom interferometers is discussed in chapter 2.

In dynamically varying environments, restrictions on interferometry times are even more severe. With time varying accelerations in multiple axes, measurements must be taken before the free-falling atoms fall out of the interferometry beams or impinge on the walls of the chamber. High bandwidth operation avoids this issue but the dramatic reduction in interferometry time significantly limits sensitivity. In chapter 3 we present the development of a laboratory based, high bandwidth atom interferometer for gravimetry. This instrument includes the unique combination of powerful laser systems, paving the way for LMT operation, and high bandwidth optimisations, improving sensitivity with cloud recapture and reduced dead time. This system will allow new operating regimes to be explored.

Whilst the high power laser in this system offers a route to improved performance in the laboratory, the size and power consumption of the laser make it impractical in the majority of field applications. Even where size, weight, and power are not an issue, the increase in cost and system complexity associated with high power lasers makes them impractical to scale by orders of magnitude to meet the demands of the most challenging future applications.

Optical cavities show considerable promise in solving the problems facing atom interferometers. An optical cavity is an arrangement of mirrors and other optics capable of supporting a circulating optical field within [43]. Resonant power enhancement allows the circulating field to dramatically exceed the input field providing an increase in the available optical power for a fixed input laser. These cavities only support certain electric field profiles and through appropriate cavity design this can be used to filter the circulating field producing flat optical wavefronts. If the technical challenges to their implementation can be addressed, the potential improvements in interferometer performance are substantial. We examine the properties of optical cavities in chapter 4.

Previous work has demonstrated cavity enhanced atom interferometry [44], and used a cavity enhanced system to place constraints on dark energy [22, 45]. Further progress has refined these techniques demonstrating large momentum transfer beamsplitters and gradiometry within an optical cavity [46], optimised experimental parameters to increase contrast [47], and demonstrated a new approach to atom interferometry suspending the atoms within a cavity enhanced optical latice [48]. Development in cavities for interferometer enhancement has yielded a large mode ($\simeq 1$ cm diameter) marginally stable cavity [49] and theoretical work has derived limits on the performance that can be obtained with conventional cavity enhancement schemes [50]. This work has demonstrated the exciting potential of cavity enhanced atom interferometry, but several key problems remain: the Doppler limit, cavity lifetime limit, and producing large modes without higher order mode degeneracy.

In chapters 5 and 6 we propose and demonstrate a cavity design that avoids the Doppler limit with an intracavity Pockels cell [2]. The Doppler limit occurs because atoms accelerate within the interferometry sequence both under the influence of gravity, and due to photon recoils. This acceleration results in Doppler shifted laser beams in the atom's inertial frame. Accurate control of the interferometer phase requires compensation of this shift by chirping the laser frequency. However, operation within an optical cavity restricts the usable frequencies to narrow bands around the cavity resonances. As a result, the laser frequencies cannot be simultaneously resonant with the cavity and compensate the Doppler shift at significant free-fall times. This limits the achievable space-time area and sensitivity for cavity enhanced atom interferometry and has placed limits on the performance of existing cavity enhanced interferometers [49–51]. The intracavity Pockels cell demonstrated in chapter 6 introduces voltage controlled birefringence to the cavity, splitting the resonance in two and allowing the separation of these resonance peaks to be controlled through the applied voltage. This removes the Doppler limit and enables much longer cavities of higher finesse to be used for atom interferometer enhancement.

The cavity in chapters 5 and 6 also demonstrates a large mode diameter whilst maintaining geometric stability, through the use of an intracavity telescope. Cavity enhanced atom interferometry with conventional two mirror cavities has been limited by small mode diameters, comparable to the millimetre scale of the atom cloud. This causes dephasing as atoms in the cloud sample different laser intensities at different locations across the cavity mode, causing a loss of contrast in the atom interferometer output. Realising large modes in an optical cavity is a challenging but tractable problem. Recent advancements have yielded a marginally stable cavity with a mode diameter of 1 cm [49] but marginal stability causes higher order mode degeneracy preventing effective spatial mode filtering, one of the key benefits sought through cavity enhancement.

By overcoming the two main limitations in cavity enhanced atom interferometry, we have enabled cavity enhancement to be applied to the vast majority of existing atom interferometers. We present further refinements to this design in chapter 7 with the magnified bow tie, which offers increased power enhancement and enables high bandwidth cavity operation, whilst retaining the large mode and Doppler compensation.

The final limitation on the largest proposed cavity enhanced systems is the effect of the cavity lifetime; parameterised by the bandwidth limit [50]. In chapter 8, we present a scheme based on circulating, spatially resolved pulses to overcome this limit and satisfy the challenging pulse requirements for $10^4\hbar k$ LMT [3]. The lifetime limit occurs because circulating fields within a cavity persist for some time after the input light has been removed. This causes the input pulse to be elongated and distorted. Where the cavity lifetime is comparable to the pulse duration, this distortion can be significant, resulting in elongation and the failure to achieve maximum power enhancement. This bandwidth limit restricts the maximum length-finesse product that can be achieved without significant pulse elongation. For metre scale lab systems and cavities of moderate finesse, such as those described thus far, the cavity lifetime is sufficiently short that this effect is not significant. However, for a kilometre scale cavity in an atom interferometer based gravitational wave detector, the bandwidth limit restricts the maximum finesse to $\mathcal{F} \leq 10$, significantly reducing the mode filtering and power enhancement benefits. The circulating pulse scheme presented here uses a pair of circulating, spatially resolved pulses of light, each producing a beamsplitter pulse once per round trip, removing the need to couple a new pulse into the cavity for each beamsplitter. This avoids cavity lifetime pulse elongation and overcomes the bandwidth limit, dramatically increasing the possible lengths and cavity finesses that can be exploited. We present parameters for the operation of such a system.

Through these innovations we have removed the key technical limitations on cavity enhanced atom interferometry. This has laid the foundations for cavity enhancement over the full spectrum of interferometers from high bandwidth compact devices up to future kilometre scale gravitational wave detectors.

CHAPTER 2

INTERFEROMETRY THEORY

An atom interferometer is a device exploiting superposition, and interference of matter waves controlled by pulses of light. The superposition and interference serve to make the output of the interferometer a sensitive probe of the phase of the light fields used to generate the beamsplitter pulses. All systems of interest can be treated as a 2-level quantum system and the behaviour of the interferometer can be analysed in a general way.

In real physical implementations the differences are in the way the light fields couple the two states. This effects the strength of the coupling, the momentum imparted by the light field in a beamsplitter pulse, and the phase reference for the beamsplitters. We shall analyse two implementations of an atom interferometer with light pulses, one using a single photon transition to a long lived excited state, and the other using two-photon Raman transitions to couple long lived ground states. The properties and scaling of each of these coupling mechanisms will be discussed, particularly with the implications on experimental design. Other types of beamsplitters have been used successfully, including Bragg transitions [52–54], Bloch oscillations [55], and stimulated Raman adiabatic passage [56], but details of these mechanisms are beyond the scope of this work.

We shall first discuss a general treatment of interferometry on a 2-level quantum system, following the treatment by Foot [57] before looking at the detail of single photon and Raman beamsplitters. This will motivate the use of these in the different types of interferometers described in this thesis, and inform the design of these systems.

2.1 Two-Level System

We shall consider a system with eigenstates of a Hamiltonian $|n\rangle$ such that:

$$\hat{H}_0 \left|n\right\rangle = E_n \left|n\right\rangle \tag{2.1}$$

As this Hamiltonian has no time dependence, we see that the state evolves as follows, where $\omega_n = E_n/\hbar$:

$$\Psi_n(\mathbf{r},t) = \psi_n(\mathbf{r})e^{-iE_nt/\hbar} = e^{-i\omega_n t}\left|n\right\rangle \tag{2.2}$$

A general state can be a written as a sum of the eigenstates, with time dependent coefficients c_n, where normalisation requires $\sum_n \left|c_n\right|^2 = 1$.

$$\Psi(\mathbf{r},t) = \sum_n c_n(t)e^{-i\omega_n t}\left|n\right\rangle \tag{2.3}$$

We now introduce a perturbing electric field $\mathbf{E}\cos(\omega t + \phi)$ where ϕ is the initial phase of this field, ω is the frequency. This field produces a perturbing Hamiltonian:

$$\hat{H}_I = e\mathbf{r}\cdot\mathbf{E}\cos(\omega t + \phi) \tag{2.4}$$

Applying the time-dependent-Schrodinger-equation to the general state in eq 2.3 with the full Hamiltonian $\hat{H} = \hat{H}_0 + \hat{H}_I$ and simplifying gives

$$i\hbar\sum_n \dot{c_n}e^{-i\omega_n t}\left|n\right\rangle = \sum_n c_n\cos(\omega t + \phi)e^{-i\omega_n t}e\mathbf{r}\cdot\mathbf{E}\left|n\right\rangle \tag{2.5}$$

Taking an inner product with state $\left\langle k\right|$, and recalling that $\left\langle k|n\right\rangle = \delta_{kn}$:

$$i\hbar\dot{c_k}e^{-i\omega_k t} = \sum_n c_n\cos(\omega t + \phi)e^{-i\omega_n t}\left\langle k\right|e\mathbf{r}\cdot\mathbf{E}\left|n\right\rangle \tag{2.6}$$

We define the Rabi frequency as:

$$\Omega_{kn} = \frac{\left\langle k\right|e\mathbf{r}\cdot\mathbf{E}\left|n\right\rangle}{\hbar} \tag{2.7}$$

Symmetry considerations reveal that $\left\langle k\right|\mathbf{r}\cdot\mathbf{E}\left|n\right\rangle = 0$ if $k = n$. $\left\langle n|n\right\rangle$ is even and $\left\langle k\right|\mathbf{r}\left|k\right\rangle$ is therefore odd and integrates to 0. Substituting this and rearranging for clarity yields:

$$i\dot{c_k} = \sum_n c_n\cos(\omega t + \phi)e^{-i(\omega_n - \omega_k)t}\Omega_{kn} \tag{2.8}$$

We now restrict ourselves to the 2 level systems of interest here, and define $\omega_0 = \omega_2 - \omega_1$. We can now characterise the behaviour with a pair of coupled differential equations.

$$i\dot{c_1} = \Omega_{12}\cos(\omega t + \phi)e^{-i\omega_0 t}c_2 \tag{2.9}$$

$$i\dot{c_2} = \Omega_{21}\cos(\omega t + \phi)e^{i\omega_0 t}c_1 \tag{2.10}$$

Making the rotating wave approximation we can rewrite these as:

$$i\dot{c_1} = \frac{\Omega_{12}}{2}e^{i(\omega-\omega_0)t+i\phi}c_2 \tag{2.11}$$

$$i\dot{c_2} = \frac{\Omega_{21}}{2}e^{-i(\omega-\omega_0)t-i\phi}c_1 \tag{2.12}$$

From the definition of Ω_{12} it is clear that $\Omega_{21} = \Omega_{12}^*$. If we further note that for bound states Ω_{21} is real, then $\Omega_{21} = \Omega_{12} = \Omega$. We can combine and solve equations 2.11 and 2.12 yielding a second order equation in c_2:

$$0 = \ddot{c_2} + i(\omega - \omega_0)\dot{c_2} + \left|\frac{\Omega}{2}\right|^2 c_2 \tag{2.13}$$

This has a general solution of the form:

$$c_2 = e^{-i(\omega-\omega_0)t/2}\left(Ae^{iWt/2} + Be^{-iWt/2}\right) \tag{2.14}$$

where the oscillation frequency for off resonant excitation is given by:

$$W = \sqrt{|\Omega|^2 + (\omega - \omega_0)^2} \tag{2.15}$$

If we assume the system starts in state $|1\rangle$ at $t = 0$ i.e. $c_2(0) = 0$ $c_1(0) = 1$

$$c_2 = -i\frac{\Omega}{W}e^{-i(\omega-\omega_0)t/2}e^{-i\phi}\sin\left(Wt/2\right) \tag{2.16}$$

and the probability of observing the system in state $|2\rangle$ is given by:

$$|c_2|^2 = \frac{\Omega^2}{W^2}\sin^2\left(\frac{Wt}{2}\right) \tag{2.17}$$

On resonance ($\omega = \omega_0$) the probability of being found in an excited state evolves according to:

$$|c_2(t)|^2 = \sin^2\left(\frac{\Omega t}{2}\right) \tag{2.18}$$

$$|c_1(t)|^2 = \cos^2\left(\frac{\Omega t}{2}\right) \tag{2.19}$$

For resonant excitation the population oscillates between states $|1\rangle$ and $|2\rangle$ with a frequency of Ω and an amplitude of unity. Off resonant excitation reduces the amplitude and increases the frequency to W. These are called Rabi oscillations and the behaviour is known as Rabi-flopping.

2.1.1 Beamsplitter Pulses

For the rest of the discussion we will assume that the radiation is resonant with the transition $\omega - \omega_0 = 0$. This simplifies the expressions for c_1 and c_2. If we again take $c_2(0) = 0$ we find:

$$c_1 = \cos\left(\frac{\Omega t}{2}\right) \tag{2.20}$$

$$c_2 = -ie^{-i\phi}\sin\left(\frac{\Omega t}{2}\right) \tag{2.21}$$

The population oscillates between the two states at the Rabi frequency Ω. There are some pulse durations of particular interest, those creating an equal superposition between states and those that flip the state. If we consider a $\frac{\pi}{2}$-pulse, i.e. a pulse duration of $\Omega t_{\pi/2} = \frac{\pi}{2}$, substituting we find:

$$\frac{\hat{\pi}}{2}|1\rangle = \frac{|1\rangle - ie^{-i\phi}|2\rangle}{\sqrt{2}} \tag{2.22}$$

That is a $\pi/2$-pulse puts the initial state in an equal superposition of the two states, with the phase factors shown. Now we consider a π-pulse, i.e. $\Omega t_\pi = \pi$:

$$\hat{\pi}|1\rangle = -ie^{-i\phi}|2\rangle \tag{2.23}$$

So a π-pulse transfers an initial state $|1\rangle$ to $|2\rangle$. We repeat the above analysis with an initial state $|2\rangle$ and find:

$$\frac{\hat{\pi}}{2}|2\rangle = \frac{-ie^{i\phi}|1\rangle + |2\rangle}{\sqrt{2}} \tag{2.24}$$

$$\hat{\pi}|2\rangle = -ie^{i\phi}|1\rangle \tag{2.25}$$

We have now calculated the effect of an electric field resonant with the 2-level system with an initial phase ϕ on both of the eigenstates of the system. We now have all of the tools we need to analyse an atom interferometer.

2.2 Symmetric Ramsey-Bordé Atom interferometry

By combining these beamsplitter pulses we can separate, recombine, and interfere the atoms, equivalently to the way light is interfered in an optical Mach-Zehnder interferometer. The pulse scheme to implement this is $\pi/2$-π-$\pi/2$ and this is called a symmetric Ramsey-Bordé interferometer. The first $\pi/2$-pulse acts as a beamsplitter creating a superposition between the two atomic states and transferring $\hbar\mathbf{k}$ of momentum to arm-B $|2\rangle$. After the interrogation time T has elapsed a π-pulse acts as a mirror and transfers the atoms into the opposite state. $\hbar\mathbf{k}$ of momentum is imparted to arm-A $|1\rangle$ and the $\hbar\mathbf{k}$ originally transferred to arm-B $|2\rangle$ is imparted back into the light field. The final $\pi/2$-pulse closes the interferometer. The state of the atoms is measured, typically with fluorescence, and the fraction of atoms in each of the two states is found. The pulse scheme is shown in the spacetime diagram figure 2.1. We shall now calculate the output of this interferometer using the beamsplitters we have analysed so far.

The first beamsplitter is a $\pi/2$-pulse with phase ϕ_1. This put the atoms in a superposition between the two states and imparts momentum $\hbar\mathbf{k}$ to the state that changes in this case $|2\rangle$.

$$\frac{\hat{\pi}}{2}|1\rangle = \frac{1}{\sqrt{2}}\left(|1,\mathbf{p}\rangle - ie^{-i\phi_1}|2,\mathbf{p}+\hbar\mathbf{k}\rangle\right) \tag{2.26}$$

We will now consider the two trajectories separately, first considering arm-A containing the atoms that remain in $|1\rangle$.

The population in state $|1\rangle$ evolves freely for a time T which from equation 2.2 adds a phase factor $\exp(-i\omega_1 T)$. We then apply the π-pulse, which at the location of arm-A at the time the pulse is applied has phase ϕ_{2A}.

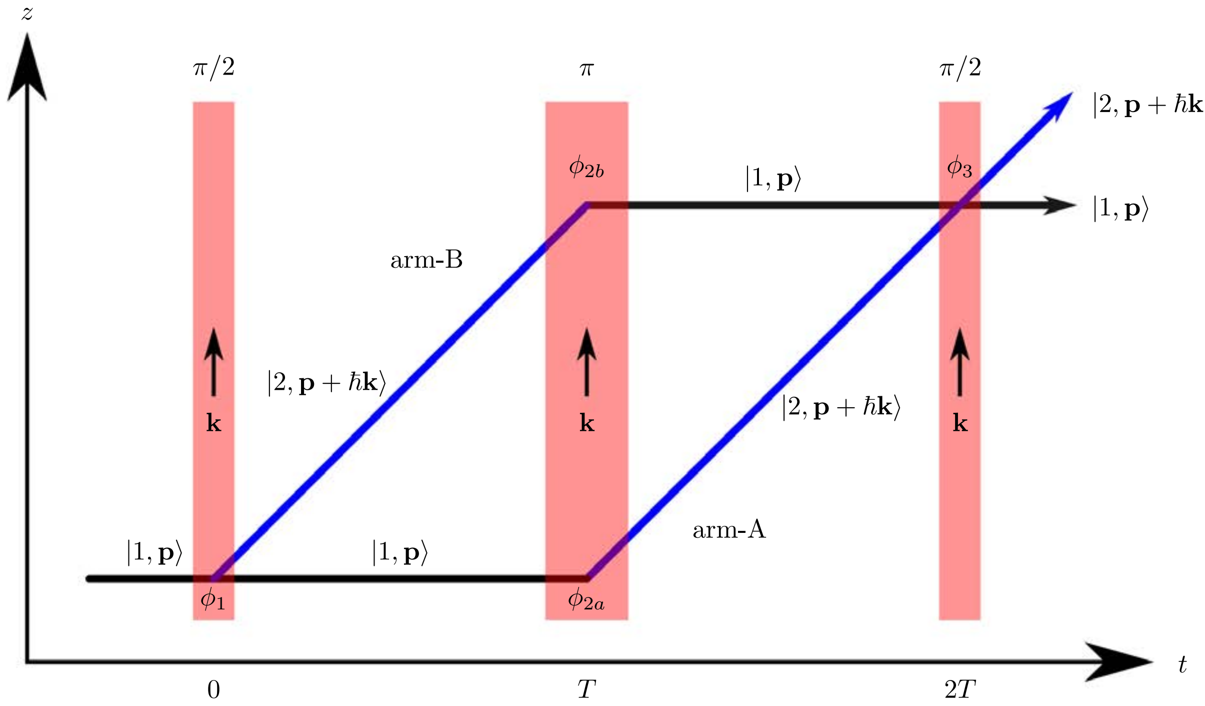

Figure 2.1: This diagram illustrates the atomic and momentum states for the two paths through the interferometer. Laser pulses are shown in red, with phases during the beamsplitters labelled.

$$\hat{\pi}\Phi_A = \frac{-ie^{-i\omega_1 T}e^{-i\phi_{2A}}\,|2,\mathbf{p}+\hbar\mathbf{k}\rangle}{\sqrt{2}} \tag{2.27}$$

Once again the state freely evolves for a time T acquiring an additional phase shift:

$$\Phi_A = \frac{-ie^{-i(\omega_1+\omega_2)T}e^{-i\phi_{2A}}\,|2,\mathbf{p}+\hbar\mathbf{k}\rangle}{\sqrt{2}} \tag{2.28}$$

Then we apply the final $\pi/2$-pulse generating the following output state from arm-A. Due to the equal time spent in each momentum state by each arm, the trajectories meet after the end of the sequence. The phase of pulse-3 (ϕ_3) is common to both arms. The output state of arm-A is:

$$\Phi_A = -\frac{1}{2}ie^{-i(\omega_1+\omega_2)T}e^{-i\phi_{2A}}\left(-ie^{i\phi_3}\,|1,\mathbf{p}\rangle + |2,\mathbf{p}+\hbar\mathbf{k}\rangle\right) \tag{2.29}$$

We now consider the evolution of arm-B of the interferometer and find:

$$\Phi_B = -\frac{1}{2} e^{-i(\omega_1+\omega_2)T} e^{i(\phi_{2B}-\phi_1)} \left(|1, \mathbf{p}\rangle - i e^{-i\phi_3} |2, \mathbf{p} + \hbar\mathbf{k}\rangle \right) \tag{2.30}$$

The state of the system at the end of the interferometer is found by summing the contributions from these arms:

$$|\Psi\rangle = \frac{-e^{-i(\omega_1+\omega_2)T}}{2} \left[\left(e^{i(\phi_{2B}-\phi_1)} + e^{-i(\phi_{2A}-\phi_3)} \right) |1, \mathbf{p}\rangle - i \left(e^{i(\phi_{2B}-\phi_1-\phi_3)} + e^{-i\phi_{2A}} \right) |2, \mathbf{p} + \hbar\mathbf{k}\rangle \right] \tag{2.31}$$

We can now find the probability of observing an atom in the two output states: $P(|1\rangle) = |\langle 1|\Psi\rangle|^2$ and $P(|2\rangle) = |\langle 2|\Psi\rangle|^2$. We find the following expressions, where $\Delta\phi = \phi_1 + \phi_3 - \phi_{2b} - \phi_{2a}$:

$$P(|1\rangle) = \frac{1}{2} (1 + \cos \Delta\phi) \tag{2.32}$$

$$P(|2\rangle) = \frac{1}{2} (1 - \cos \Delta\phi) \tag{2.33}$$

There is no contribution from the free evolution, because both arms spend the same amount of time in each of the two states.

2.2.1 Phase in Atom Interferometry

The output state of the interferometer is an extremely sensitive measure of the phase of the beamsplitter fields. We are going to examine the case of gravity measurement, and see how the strength of the gravitational field manifests itself in the phase and is measured by the atom interferometer.

The time and spatial dependence of the phase of an EM wave is given by $\phi(\mathbf{r}, t) = (\mathbf{k} \cdot \mathbf{r} - \omega t)$. We are free to set the initial phase to any value we choose, and for convenience we set $\phi_1 = 0$. To find the other phase contributions we need to calculate the location of the atoms during the beamsplitter pulse. Arm-A initially follows a ballistic trajectory with initial momentum $\mathbf{p_0}$. We calculate the location at time T, and the phase ϕ_{2a}:

$$\mathbf{r}_{2a} = \frac{\mathbf{p_0}}{m} T - \frac{1}{2} \mathbf{g} T^2 \tag{2.34}$$

$$\phi_{2a} = \mathbf{k} \cdot \left(\frac{\mathbf{p_0}}{m} T - \frac{1}{2} \mathbf{g} T^2 \right) - \omega T \tag{2.35}$$

Arm-B has an additional momentum from the photon recoil in the initial beamsplitter, taking a total $\mathbf{p} = \mathbf{p_0} + \hbar \mathbf{k}$. The phase at the second beamsplitter is given by:

$$\phi_{2b} = \mathbf{k} \cdot \left(\frac{\mathbf{p_0} + \hbar \mathbf{k}}{m} T - \frac{1}{2} \mathbf{g} T^2 \right) - \omega T \tag{2.36}$$

Considering the trajectory of either arm yields ϕ_3:

$$\phi_3 = \mathbf{k} \cdot \left(\frac{2\mathbf{p_0} + \hbar \mathbf{k}}{m} T - 2\mathbf{g} T^2 \right) - 2\omega T \tag{2.37}$$

Summing these phase contributions to find the argument of the cosine in equation 2.32:

$$\Delta\phi = -\mathbf{k} \cdot \mathbf{g} T^2 \tag{2.38}$$

To maximise the phase contribution arising from gravity we align the $\mathbf{k}$-vector with the direction of the gravitational field $\hat{\mathbf{g}}$. We find $\Delta\phi = kgT^2$ and see that the output phase is proportional to the square of the freefall time T and the k-vector of the beamsplitter field.

More rigorous derivations include the phase shifts caused by finite pulse durations and those without chirping [58]. This is important when the pulse duration t_π is comparable to the interrogation time T such as in high bandwidth systems. An expression for the phase difference arising from these contributions (neglecting terms $\sim t_\pi^2$) is given by equation 2.39.

$$\Delta\phi = -\mathbf{k_{eff}} \cdot \mathbf{g} \left[T^2 + t_\pi \left(1 + \frac{2}{\pi} \right) T \right] \tag{2.39}$$

2.2.2 Detection

At the end of the interferometry sequence we detect the relative atomic populations in each of the output states. This is typically based on state dependent fluorescence and the ability to determine the output state is limited by the atom number [59]. For interferometers obeying classical statistics, this is a shot noise limited process (noise goes with $N^{-1/2}$ where N is the number of atoms in the interferometer). For a given detection fidelity, the sensitivity of the interferometer increases with the total phase difference of the interferometer. This motivates the use of long T-times and large k-vectors.

The quadratic dependence in T in the interferometer phase in equation 2.38 suggests that longer T times make interferometers more sensitive. Everything else being equal sensitivity would increase with $T^{3/2}$. In a fixed observation period (τ) one can take N measurements of duration T, giving a sensitivity of $R \propto \sqrt{N}T^2$ (averaging of uncorrelated noise increases sensitivity as $\sqrt{N}$). $N \propto \tau/T$ (at constant duty cycle) so the sensitivity scales with $R \propto \sqrt{\tau T^3}$, which for a fixed measurement window gives $R \propto T^{3/2}$. Whilst the most sensitive instruments do exploit T times in excess of a second, this requires several metres of free fall, highly optimised laser cooling, and generally results in small numbers of atoms at low duty cycle. Systems operating at high bandwidth (>10 Hz) necessarily have short T-times but as we shall see in chapter 3 there are several strategies that allow these systems to make up some of the loss in sensitivity.

2.2.3 Chirp

In the preceding discussion we neglected the effect of the Doppler shift on the accelerating atom clouds. This is inconsistent with our previous assumption that the driving field is resonant with the atoms. For a change of velocity $\mathbf{\Delta v}$ the Doppler shift is:

$$\Delta\omega = -\mathbf{k} \cdot \Delta\mathbf{v} \tag{2.40}$$

$$\Delta\omega = -\mathbf{k} \cdot \mathbf{g}\Delta t \tag{2.41}$$

This is the rate of change of frequency which compensates for the gravitationally induced Doppler shift. We will now consider the effect of a chirp on the phase shift of the interferometer. We consider the effect a general chirp rate α on the phase. In expressions 2.35, 2.36, 2.37 we introduce a chirp onto the frequency of the radiation $\omega(t) = \omega_0 + \alpha t$, and note the time dependence in the phase is the integral of this:

$$\phi(t) = \omega_0 t + \frac{1}{2}\alpha t^2 \tag{2.42}$$

With this substitution we find:

$$\Delta\phi = -(\mathbf{k} \cdot \mathbf{g} + \alpha)T^2 \tag{2.43}$$

If $\alpha = -\mathbf{g} \cdot \mathbf{k}$ then the chirp rate compensates for the gravitationally induced phase shift and $\Delta\phi = 0$. This is the value calculated initially based on simple Doppler shift considerations. A gravity measurement can be implemented by tuning the chirp rate to that which results in $\Delta\phi = 0$ for all values of T.

2.2.4 Cloud Temperature

In the preceding discussion we neglected any effects caused by finite cloud temperature. A finite temperature results in a distribution of atom velocities and a corresponding distribution of Doppler shifted frequencies. It is no longer possible to have all the atoms on resonance simultaneously. Off resonant drive results in an increased oscillation frequency and a reduced oscillation amplitude (equation 2.17). At the output of the interferometer this manifests as reduced contrast. The degree of this reduction scales with W, see equation 2.15. Finite temperatures also result in cloud expansion, causing atoms to sample different areas of the interferometry beam in successive beamsplitter pulses. Any inhomogeneity in phase across the beam, or variations in intensity will result in reduced contrast. For this reason we operate atom interferometers with laser cooled atom clouds reaching temperatures in the microkelvin range; see appendix E for a discussion of laser cooling. Considering the effect across the entire cloud, a π-pulse has a Doppler limited temperature bandwidth given by the following [60]:

$$T_{\text{Doppler}} \propto \Omega^2 \tag{2.44}$$

For a given cloud temperature, increasing the Rabi frequency allows a broader velocity class of atoms to be addressed, increasing contrast. This requires increased optical power. The velocity selection of these pulses is used to measure the temperature of atom cloud in chapter 3.6.

2.2.5 Beam Size

The analysis presented so far makes no reference to the size of the beam, treating the radiation as a uniform electric field with a single phase over the extent of the atom. For a single atom this is an excellent approximation. In an atom interferometer the atoms are typically sourced from a cloud of cold atoms. This cloud has finite size typically of order millimetres, yet we still assume that the intensity and phase are constant across the cloud.

Satisfying this condition requires large beams (with correspondingly large optical power) with a flat phase front across the beam. Initially neglecting cloud temperature, the variation in intensity will result in different Rabi frequencies for different atoms within the cloud. This reduces the contrast of the interferometer, reducing sensitivity. Including cloud temperature produces several effects. Firstly, the atom cloud experiences a range of Doppler shifts due to the finite atomic velocity distribution within it. This causes different atoms to experience different detunings, as discussed in section 2.2.4. Secondly, the transverse motion of atoms across the beam causes them to sample different intensities for the different pulses, further reducing contrast. If the beam contains wavefront aberrations, then different phases at different points in the beam will be sampled during the pulses. These parasitic phase shifts introduce a source of bias uncertainty and instability in the interferometer measurement. Atom interferometers must take precautions to ensure that the phase fronts of beamsplitters are as uniform as possible, with high quality optics, deformable mirrors, and recently optical cavities all offering solutions to this problem [34, 37, 44].

2.2.6 Excited State Lifetime

For atom interferometry we require strong coupling that imparts momentum between two long lived states. The examination of the Einstein A and B coefficients reveal that these are contradictory requirements: [57,61]

$$A_{21} = \frac{\hbar\omega^3}{\pi^2 c^3}\frac{g_1}{g_2}B_{12} \tag{2.45}$$

The A coefficient is the rate of spontaneous emission from the excited state, whilst the B coefficients describe the rate of stimulated emission and absorption. The frequency of the transition is given by ω and g_i is the degeneracy of level i. These coefficients are proportional and scale with the cube of the transition frequency. Therefore, higher frequency transitions have shorter excited state lifetimes for a given coupling strength. This link between the coupling strength, transition frequency, and excited state lifetime is key to understanding the choice of transitions used in atom interferometry.

This inherent conflict is resolved in two different ways. Raman transitions coupling low lying ground state transitions, which have a long excited state lifetime due to the small frequency difference $\omega \simeq$ GHz, through two photon optical transitions allowing an exchange of momentum. Coupling these states directly with microwaves would impart 10^5 times less momentum and reduce interferometer performance commensurately. The other approach considered here uses single photons on forbidden transitions having very low rates of spontaneous emission. This resolves the problem of excited state lifetime but results in weak coupling, and makes achieving useful Rabi frequencies difficult. With intense lasers, these transitions can be driven but at reduced rates compared to Raman transitions.

2.2.7 K-Vector

The overall phase of the interferometer is proportional to the k-vector of the beamsplitter pulse. For a single photon the magnitude of this vector is given by $2\pi/\lambda$ where λ is the photon wavelength.

We maximise sensitivity by increasing this and the most obvious way to do this is to reduce the wavelength of the radiation we are using. The shortest wavelengths of radiation that can be conveniently generated and controlled in a phase stable way are visible photons generated by lasers. Whilst developments in laser technology is opening up UV-wavelengths, this is unlikely to offer more than a factor of two increase in the near term. Shorter wavelengths significantly increase experimental complexity. Optical flatness constraints for a given phase performance increase, optical fibre performance decreases, and laser power, performance, and operating lifetime all tend to decrease. A more fundamental problem with shorter wavelengths can be inferred from equation 2.45. The Einstein A coefficient is proportional to $\omega^3 \propto \lambda^{-3}$, so moving to shorter wavelengths reduces the excited state lifetime and increases spontaneous emission as a source of decoherence.

Instead we combine multiple photons in composite pulses to increase the total momentum separation. Such sequences generate a large momentum transfer to the atoms and are generally known as LMT. Typically the initial $\pi/2$-pulse is followed by sequential π-pulses each in alternating directions each of which impart momentum to the sequence and the total momenta sum. The fidelity of each individual pulse must be high to maintain overall sequence fidelity as the number of pulses increases.

2.3 Single Photon

We can implement the two level system described in section 2.1 directly with resonant excitation of a single photon transition between two long lived states. The challenge of this approach is achieving strong coupling to a state with long excited state lifetime. This is essential as spontaneous emission is a source of decoherence. As we saw in section 2.2.6 these are contradictory properties. We shall revisit the strength of coupling in single photon transmissions, before examining how the phase of the transitions ϕ and the $\mathbf{k}$-vectors manifest in these systems. We will then examine some specific implementations of single photon interferometry and compare the approaches.

2.3.1 Rabi Frequency

As we found in section 2.1 the strength of a coupling between two states is characterised by the Rabi frequency and is given by equation 2.7. Transitions of interest are in the optical frequency regime and are coupled with laser beams. The strength of these fields is measured by the intensity:

$$I = \frac{c\epsilon_0}{2}|E|^2 \tag{2.46}$$

For single photon transitions the Rabi frequency is proportional to the root of the input intensity with a constant of proportionality depending on the atomic species and transition in question.

$$\Omega = \alpha\sqrt{I} \tag{2.47}$$

Long lived excited states are required to maintain coherence in the interferometer allowing long interrogation times (T-times) maximising interferometer sensitivity which scales with T^2. As we established in section 2.2.6, states with long excited state lifetimes necessarily have weak coupling, so we should expect α to be small in systems of interest. Strong coupling requires high intensities.

2.3.2 Single Photon K-vector and LMT

For a single photon beamsplitter the **k**-vector is simply given by the **k**-vector for the EM wave, and the momentum exchanged in an interaction is $\hbar\mathbf{k}$ where $k = 2\pi/\lambda$ and λ is the wavelength. This motivates the use of the shortest possible wavelengths to maximise phase sensitivity.

In experiments we are constrained by the availability of lasers and most transitions demonstrated so far are in the visible or near IR. We instead increase the effective k-vector by replacing our single photon transition with multiple single photon transitions each imparting momentum $\hbar k$. By alternating the k-vector of these photons the momentum contributions of successive pulses sum and a momentum separation of $(2N-1)\hbar k$ can be achieved, where N is the number of pulses in the sequence. These techniques for increasing the momentum separation of the two arms are known as large momentum transfer (LMT). The full interferometer is assembled from LMT-pulses and the overall phase is given by: $\Delta\phi = -\mathbf{k}_{\text{eff}} \cdot \mathbf{g}T^2$ where $\mathbf{k}_{\text{eff}} = (2N-1)k$. A pulse sequence for LMT with single photon beamsplitters is shown in figure 2.2.

2.3.3 Phase in Single Photon Interferometry

The phase of the light field is imparted onto the atomic state during the beamsplitter pulse. The laser is the phase reference for the interferometer and as a result the coherence time must exceed the total interferometer duration. Achieving phase stability on optical signals is challenging experimentally as phase noise induced from changing optical paths between the laser and the atoms, along with phase noise in the laser itself all

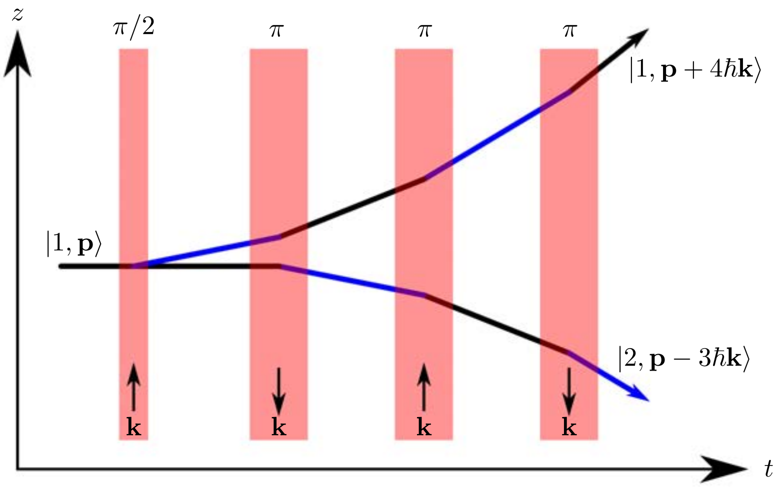

Figure 2.2: A single photon LMT sequence containing four pulses. The momentum separation at the end of this sequence is $7\hbar\mathbf{k}$.

contribute. Developments in optical atomic clocks have produced lasers with sub-Hz linewidth which can operate on such single photon transitions.

One implementation that avoids these demanding phase stability requirements is gradiometry. Any phase fluctuations are common mode between the two interferometers (provided they are only separated by a vacuum). The output signal is the phase difference between the two interferometers, and can be inferred by plotting the output as an ellipse. In this configuration the requirement on phase stability is ensuring the laser remains resonant with the transition, $\omega = \omega_0$. The relevant comparison is between Rabi frequency and detuning, see equation 2.15 so this relaxes $<$ Hz requirement for a 1s interferometer to $\simeq$ kHz for an interferometer with a 10 kHz Rabi frequency; this performance is routinely achieved with commercially available systems.

This gradiometer configuration shows particular promise for proposed kilometre scale atom interferometers proposed for gravitational wave detection and scalar dark matter surveys [29, 62]. In these systems the travel time between the atom clouds is significant, so having a common phase reference between the two clouds is critical. Single photon beamsplitters readily achieve this.

2.4 Single Photon Experimental Implementation

Several species and states have been used in single photon interferometry. Here we will focus on two important states in Strontium. Strontium has been successfully laser cooled and trapped [63] and has a narrow line transition that has been successfully exploited in atomic clocks [64]. These along with the convenient wavelengths for lasers make strontium a promising species for atom interferometry.

2.4.1 Strontium 698 nm Clock Transition

A promising transition for single photon atom interferometry is the 698 nm clock transition between $5s\,^1S_0$ and $5s5p\,^3P_0$. This exists in both the fermionic ^{87}Sr and bosonic ^{88}Sr isotopes of strontium. This is forbidden for both the change in spin, and angular momentum, $\Delta S = 1$ and $J = 0 \rightarrow J = 0$. Interferometry has been demonstrated in the bosonic ^{88}Sr where the transition is induced by the application of a magnetic field [65]. Difficulty producing high uniformity magnetic fields over large experimental volumes make the fermionic isotope a promising candidate for future large interferometers for gravitational wave detection. We will restrict our discussion to ^{87}Sr for the remainder of this discussion and in the circulating pulse scheme presented in chapter 8.

In fermionic ^{87}Sr the coupling of this forbidden transition is caused by state mixing of $^3P_0$ through the interaction with the nuclear spin, no longer requiring the uniform magnetic field. This results in a transition with mHz linewidth and an excited state lifetime of approximately 150 s [66–68]. The Rabi frequency is given by equation 2.48 where $I_s \simeq 0.4$ pWcm^{-2} and $\Gamma_{87} \simeq 2\pi \times 1$ mHz [69].

$$\Omega_{87} = \Gamma_{87}\sqrt{\frac{I}{2I_s}} \tag{2.48}$$

As with other single photon transitions this scales with $\sqrt{I}$ and due to the narrow linewidth this transition is a very weak coupling. To get the 100 kHz Rabi frequencies commonly achieved in 2-photon interferometry requires a laser intensity of 8 kWcm^{-2}. This is an incredibly high intensity, and with typical beam diameters of $\simeq$ cm requires lasers with kilowatt output powers. Typical output powers of lasers used in atom interferometry are at the few watt level, with some exceptionally high power systems with 40 W [41, 70]. If we want high Rabi frequencies on this transition we need to address this. One possible approach to realising these power requirements is discussed in chapter 8.

2.4.2 Strontium-88 Intercombination Line

The intercombination line in ^{88}Sr couples $^1S_0 - ^3P_1$ at a wavelength of 689 nm. This transition has an excited state lifetime of only 21.6 μs and a linewidth 7.4 kHz [66, 71]. This permits much higher Rabi frequencies with 3.1 MHz demonstrated with an intensity of only 3 Wcm^{-2}. Such high Rabi frequencies allow LMT to be implemented, and result in pulses that address a very broad velocity class of the atom cloud with high fidelity.

The short excited state lifetime requires a more complex interferometry sequence to maintain coherence at reasonable interrogation times. After initial beamsplitters have been performed the excited state population is transferred back to the ground state to minimise spontaneous emission losses. Spontaneous emission is still a significant source of loss and that can only be reduced by reducing the time spent in the excited state. [71]

Future interferometers may use some combination of high Rabi frequency broader line transitions and narrow line, long coherence time transitions to exploit the benefits of both.

2.5 Raman Transitions

The two level system described in section 2.1 can also be implemented with stimulated Raman transitions coupling two ground state levels. Stimulated Raman transitions are coherent two-photon processes that allow long lived ground states to be coupled through the use of a virtual excited state. With appropriate choice of virtual state this can be accomplished with high fidelity and the resulting system behaves like an ideal two level system [72]. Losses due to spontaneous emission from the ground state are negligible. By controlling the duration, power, and detuning of these photons a coherent superposition of the two states can be generated. The two photon process imparts momentum to the atoms allowing an atom interferometer to be constructed. Raman transitions are the most popular scheme for implementing atom interferometry. The experimental implementations described in chapters 3 and 6 both use Raman beamsplitters. In the following section we will examine the properties of Raman transitions, particularly focusing on the scaling rules that inform experiment design.

2.5.1 Rabi Frequency

The Rabi frequency for a Raman transition with $\delta = 0$, Ω_{eff} is given by equation 2.49:

$$\Omega_{\text{eff}} = \frac{\Omega_{1i}\Omega_{2i}}{2\Delta} \tag{2.49}$$

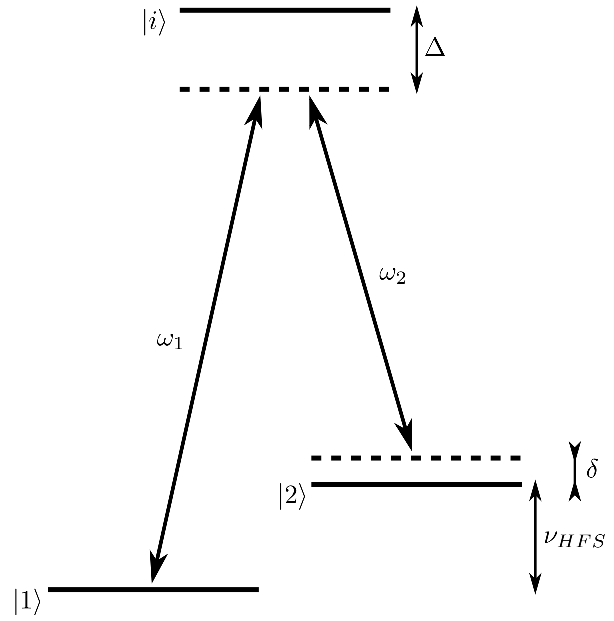

Figure 2.3: Stimulated Raman transitions coherently couple the two ground state levels through the use of an intermediate excited state. The intermediate state is shown as a dashed line, detuned from $|i\rangle$ by the single-photon detuning Δ. The two-photon detuning is labelled δ.

Where Δ is the single-photon detuning, and Ω_{ij} is the single photon Rabi frequency coupling states $|i\rangle$ and $|j\rangle$, defined in equation 2.7. In this case $|i\rangle$ is the virtual excited state level and $|j\rangle$ represents either of the two ground state levels.

For an electromagnetic wave, the intensity is proportional to the square of the electric field:

$$I = \frac{c\epsilon_0}{2}|E|^2 \tag{2.50}$$

Recalling that $\Omega_{ij} \propto \sqrt{I_{ij}}$ we can see that the effective Rabi frequency for a Raman transition is proportional to the root of the intensity in each of the two Raman beams.

$$\Omega_{\text{eff}} \propto \frac{\sqrt{I_1 I_2}}{\Delta} \tag{2.51}$$

For a fixed total optical power the highest Rabi frequency is achieved when the intensities of two beams are equal. In this equal power mode $\Omega_{\text{eff}} \propto I$ is proportional to total laser power. This scaling is favourable compared to the $\sqrt{I}$ scaling on single photon transitions.

2.5.2 Detuning and Scatter

From equation 2.49 we can see that the Rabi frequency is inversely proportional to the detuning Δ. This suggests that small detunings will result in higher Rabi frequencies, and from the discussion on pulse duration, higher fidelity beamsplitters. This neglects the effect of scattering from the excited state, which we expect to be an important mechanism for Raman Pulse fidelity. In the following section we will consider the scattering rate of a single photon at a given detuning (Δ) from a single transition, under a strong driving field in equilibrium [57]. This is a gross simplification of the Raman case with two photons and a manifold of excited state levels, but still captures how scattering rate scales with experimental parameters. A more detailed analysis or Raman transitions and scattering can be found in the following references [73–75]. Considering a laser beam detuned from the excited state by Δ the scattering rate is given by the following:

$$\mathcal{R}_s = \frac{\Gamma}{2}\frac{\Omega_{ij}^2}{2\Delta^2 + \Omega_{ij}^2 + \Gamma^2/2} \tag{2.52}$$

The Rabi frequency Ω_{ij} takes its previous definition, and Γ^{-1} is the lifetime of the excited state.

For Raman transitions we operate in the limit where $\Delta \gg \Omega, \Gamma$ so:

$$\mathcal{R}_S \propto \frac{\Omega_{ij}^2}{\Delta^2} \propto \frac{I_{ij}}{\Delta^2} \tag{2.53}$$

As the effective Rabi frequency for the Raman transition $\Omega_{eff} \propto \Delta^{-1}$ and the scattering rate $\mathcal{R}_s \propto \Delta^{-2}$ we can reduce scatter and improve the fidelity of our Raman pulses by increasing the detuning. This can be achieved at constant Rabi frequency by increasing the intensity to compensate. This is another reason why high intensity lasers are essential for high performance atom interferometry.

Incoherent scattering of the kind discussed here causes an atom to be lost from the interferometer and reduces overall pulse efficiencies. For a standard 3-pulse interferometry sequence this is not usually a limitation as even 60% π-pulse efficiency still results in 36% of atoms at the output of the interferometer. This can be achieved with modest detunings ~GHz. As this loss scales arithmetically with the number of laser pulses, large momentum transfer interferometers (utilising many pulses) require much higher efficiencies and they operate at correspondingly large detunings. In practice the optimum detuning is a trade off between Rabi frequency and pulse fidelity and will depend on the specifics of the system, free fall time, and available optical power.

2.5.3 Phase

In Raman transitions it is not the absolute phase of the light (as in the single photon case) but the relative phase between the two Raman beams, that forms the phase reference for the interferometer. This is a huge simplification in laser requirements, as implementing a phase lock at the Hertz level is far simpler than implementing a laser with Hertz level frequency stability. The two Raman beams are often generated from a single seed laser by electro-optic modulation, and it is then the phase stability of the RF modulator that requires the <Hz performance, not the seed laser itself. This is readily achievable with commercially available components.

We maximise momentum transfer by making the beams counter propagate when they reach the atoms. This is generally achieved by delivering both beams together (co-propagating), and then retroreflecting the beams from a mirror after passing through the atoms. The Doppler shift of the moving atoms is used to lift the degeneracy between these two counterpropagating directions, with one beam in each direction forming the Raman pair. The mirror becomes the inertial reference for the system, with any motion of the mirror producing a path difference and changing the relative phase of the two beams.

In large scale systems such as those proposed for gravitational wave detection, the propagation time between atom clouds is large. This places an extreme constraint on the relative phase stability of the two beams at the propagation time and implies an unfeasible frequency stability. Single photon transitions are the preferred option in this case [29].

2.5.4 Raman K-vector and LMT

Conservation of momentum in the Raman transition shows that the process imparts momentum to the atomic transition. If $\hbar\mathbf{k_i}$ is the momentum of one photon the total momentum transfer in the two photon transition is given by:

$$\hbar\mathbf{k_{eff}} = \hbar(\mathbf{k_1} - \mathbf{k_2}) \tag{2.54}$$

We can see that the momentum is maximised when the two k-vectors are anti-parallel, meaning the beams are counterpropagating. For most systems the frequency difference between the two Raman beams is very small (GHz in optical frequencies) so $|\mathbf{k_1}| \simeq |\mathbf{k_2}|$ and the total momentum exchanged with the atoms by counterpropagating Raman beams is $2\hbar k$.

The momentum exchange can be increased beyond this by combining multiple Raman beamsplitters to increase the total momentum separation in a LMT pulse. A $\pi/2$-pulse with LMT would follow a traditional $\pi/2$-pulse with a series of π-pulses flipping the propagation directions of $\mathbf{k_1}$ and $\mathbf{k_2}$ for each successive pulse such that contributions add constructively. An interferometer with N-LMT pulses will produce a momentum separation between arms of $(4N + 2)\hbar k$ [39]. As with other pulse types, the individual pulse fidelity must be high to maintain fidelity through an LMT sequence.

CHAPTER 3

HIGH BANDWIDTH ATOM INTERFEROMETRY

In the following chapter I present the results of the high-bandwidth atom interferometer constructed at Sandia National Laboratories[2] in the Biedermann group in 2017[3]. We discuss high bandwidth interferometry and then characterise the atom interferometer. We first consider the efficacy of our optical pumping with a microwave π-pulse, and the use of this technique for measuring and cancelling stray magnetic fields. We consider Doppler free Raman pulses and their efficiencies as a further validation of this measurement and of our Raman beam alignment. We combine Doppler sensitive Raman pulses in a $\frac{\pi}{2} \rightarrow \pi \rightarrow \frac{\pi}{2}$ (Mach-Zehnder type) sequence to demonstrate an atom interferometer and measure the projection of $\mathbf{g}$ along the Raman beam axis. We exploit the Doppler sensitivity of the Raman pulses to measure the temperature of the sub-Doppler cooled atomic sample. Finally we consider how our powerful Raman beams can be used to enhance sensitivity. Details of the system design, laser systems, cooling and trapping, and the experimental sequence are presented in appendices C, D, E, and F respectively.

3.1 Introduction to High Bandwidth Interferometry

The bias stability of atom interferometers makes them highly attractive for applications requiring accurate acceleration and gravity measurement. Inertial navigation systems have these demands and are often operated in dynamically varying environments. Atom interferometers in these environments must measure the output state before accelerations have caused the atoms to fall out of laser beams or impact the walls of the chamber,

---

[2] Sandia National Laboratories is a multimission laboratory managed and operated by National Technology & Engineering Solutions of Sandia, LLC, a wholly owned subsidiary of Honeywell International Inc., for the U.S. Department of Energy's National Nuclear Security Administration under contract DE-NA0003525. This material along with appendicies B,C,D,E,F were approved for public release in 2018 as "A Laboratory Atom Interferometer Instrument", SAND2018-9859 R; further dissemination is unlimited.

[3] This work was funded in part by Sandia through the Laboratory Directed Research and Development program.

making high bandwidth operation essential. The primary challenge in realising sensitive, high bandwidth atom interferometry is the T^2 dependence on interferometer phase; see chapter 2. High bandwidth sensors necessarily have short T times, and everything else being equal there would be little interest in pursuing such devices. With a high bandwidth T-time of 10 ms, compared to 100 ms in a modest lab system with an equivalent atom number and detection fidelity, the sensitivity would be 100 times less. Fortunately high bandwidth operation offers some unique advantages which allow some of this performance to be recovered.

The instrument described in this chapter operates at > 40 Hz and this offers some key advantages. At short T times the atoms cannot travel a large spatial distance; this allows efficient recapture of the atoms and results in a significant reduction in dead time between measurements. The instrument is also physically compact with 10ms freefall only travelling 0.5 mm compared with the 1.25 m required for a 0.5 s drop. The short T-time relaxes the constraints on atomic cloud temperature. A higher temperature cloud will remain within the Raman beams during the interferometry sequence simply because it has insufficient time to leave. This reduces the requirements on laser cooling and allows us to address a broader velocity class of atoms. Atom interferometers typically have to employ velocity selection and blow-away pulses to retain contrast during interferometry; short T times make this unnecessary. With sufficiently powerful Raman beams, a significant fraction of the atoms within the MOT are able to participate. All interferometers are fundamentally limited by atom shot noise, and if the technical challenges can be met to allow the instrument to operate at that limit, then these large increases in atom number will allow high bandwidth systems to achieve high sensitivities [76]. Large atom numbers, short dead times, and compact sizes all make high bandwidth interferometry a promising technique for future sensors.

3.2 Optical Pumping

After laser cooling is complete, the depump laser initialises the atoms into the $|F = 2, m_F = 0\rangle$ sublevel. We verify that this is successful with a scan in frequency of a π-pulse delivered by a microwave horn, shown in figure 3.1. The microwave frequency is scanned about its resonance at 6.83468 GHz. The pulse length is adjusted to realise a π-pulse at 0 detuning, and this pulse length is used for the entire spectroscopy measurement. At larger microwave detunings the difference in π-pulse length will reduce the transfer efficiency but that is not a significant effect here. Each data point represents a separate experiment comprising cooling, optical pumping, a microwave pulse, and detection. The $m_f = 0 \rightarrow 0$ transition (located at 0 detuning) transfers 93% of the population from the $F = 2$ state. This means that at least 93% of the atoms must be initialised into this state, greatly exceeding the 20% expected from a randomly distributed sample. The transitions at ±0.186 MHz correspond to $m_f = 0 \to \pm 1$ and occur because the polarisation of the microwaves is not purely π. The peaks at ±0.372 MHz correspond to $m_f = -1 \to -1$ and $m_f = 1 \to 1$. Both transitions show 3% transfer indicating that 3% of the atoms are in each of these states. This is consistent with the optical pumping efficiency determined from the $m_f = 0 \to 0$ transition.

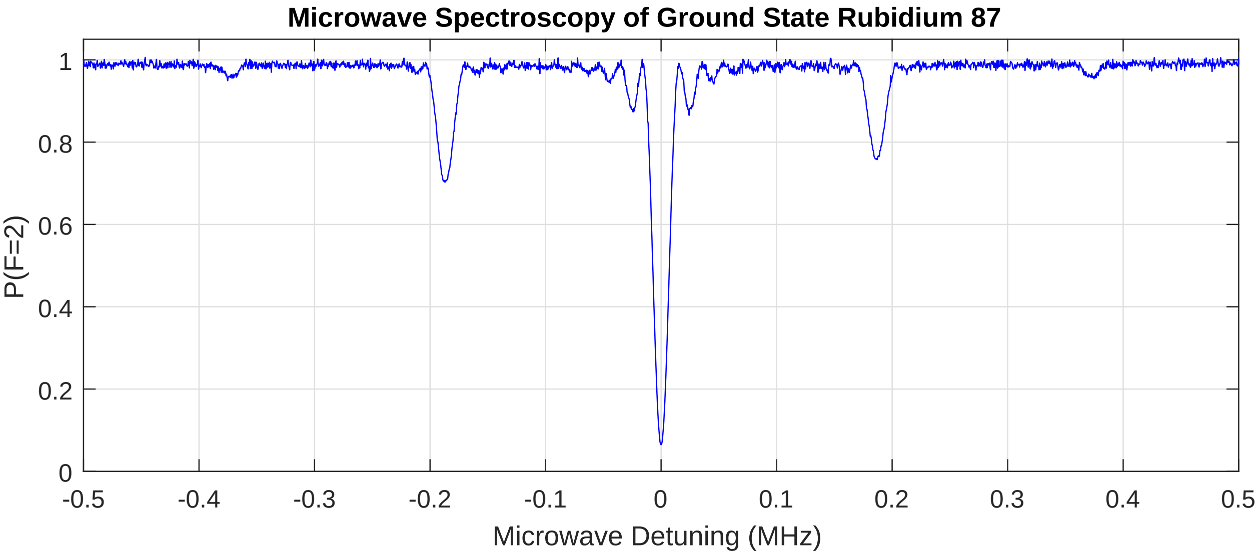

Figure 3.1: This plot shows the probability of finding an atom in the $F = 2$ ground state of ^{87}Rb after the application of a microwave π-pulse. The microwave frequency is scanned around resonance at 6.83468 GHz. The 93% transfer efficiency on resonance indicates that optical pumping is working efficiently.

The magnetic field applied to the experiment during this spectroscopy can be easily determined from the spacing of these peaks. The Zeeman sensitivity of these levels is 0.7 MHz G^{-1}, therefore the magnetic field applied during this microwave interferometry is 0.265 Gauss. For optical pumping to succeed it is essential that a bias field is applied to set a quantisation axis for the atoms, and in turn ensure that the $|F = 2, m_F = 0\rangle$ sublevel is dark. When optimising the bias fields to null any background, RF spectroscopy can be employed in an identical way. A spectroscopy measurement is taken, the splitting measured, the current supplied to a bias field varied, and the spectroscopy repeated. A reduction in peak spacing indicates that the residual fields have decreased. By iterating through the coils, it is possible to reduce the residual field to the point where all the Zeeman sublevels are degenerate, at which point the background fields have been nulled.

3.3 Doppler Free Raman Pulses

High bandwidth operation is difficult to achieve with Raman beam retroreflection. For retroreflection to succeed the atoms must be at sufficient velocity for the Doppler effect to discriminate between the original and reflected beams. In practice this means that the Doppler shift must be at least as large as the linewidth of the Raman transition. For a Raman pulse length $t_\pi = 8$ μs this condition is achieved after 9 ms of freefall. This limits the bandwidth to 111 Hz without allowing any time for atom loading or interrogation. In the 25 ms cycle time we ultimately use, this delay would reduce our bandwidth by 36% without considering the reduction in recapture efficiency caused by the increased freefall distance. Using shorter t_π times to address a larger velocity class of atoms (one of the key advantages of high bandwidth interferometry) would cause this free-fall delay to increase. Future experiments may use a launch to break the Doppler symmetry more quickly, but in our case we choose to avoid the experimental complexity and instead deliver our Raman beams through two separate fibres.

When setting up the experiment we initially operate in Doppler free mode where both beams are delivered by the same fibre and copropagate. Whilst this mode is not sensitive to accelerations it greatly simplifies the initial alignment. The copropagating beams must only overlap with the atoms (by maximising Rabi frequency) and be parallel with vertical (through retroreflection from a horizontal mirror).

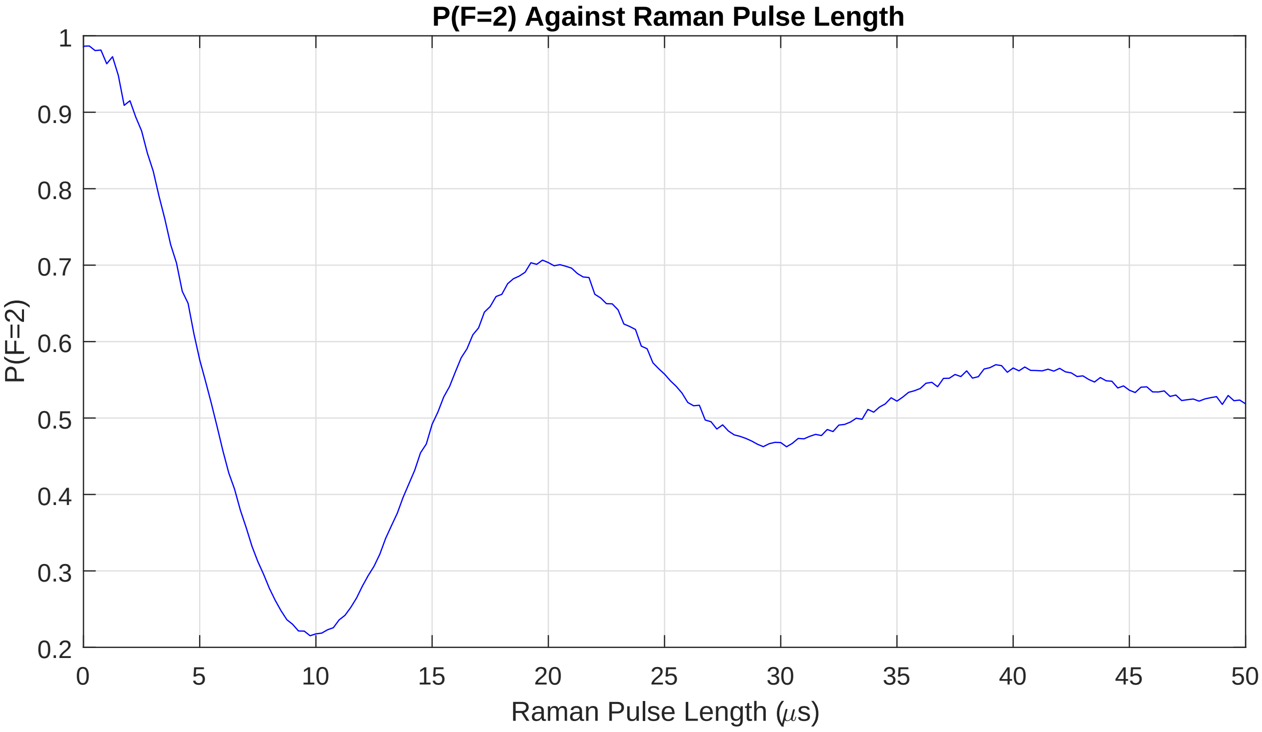

Figure 3.2: Doppler free Rabi flopping with a Rabi frequency of 20 kHz. The π-pulse efficiency is 78% providing further confirmation of successful optical pumping.

3.4 Doppler Sensitive Raman Pulses

To align the second Raman beam we adjust the delivery optics to couple the first beam into the second fibre. This through-coupling guarantees beam overlap, counter-propagation, atom overlap, and verticality (provided these conditions were met by the first beam). The fact that our Raman beams are 5.5 mm in diameter relaxes the constraints on beam overlap and atomic alignment whilst maintaining pulse efficiency. With the Raman beams aligned, we are able to proceed with the Doppler sensitive Raman transitions. The coherence time and transfer efficiencies are both lower for our Doppler sensitive beams, likely due to the velocity selection caused by finite cloud temperature; see section 3.6.

3.5 Atom Interferometry

We implement a Symmetric Ramsey-Bordé Atom interferometer of the type discussed in chapter 2.2 and observe interference fringes. By measuring the output of a large number of interferometers of increasing interrogation time T (spacing between pulses) we are able to generate a single plot that encompasses all of the key information about the interferometer. We operate the interferometer without chirping the Raman beams. For a high bandwidth system with short T-times the Doppler shift is insufficient to degrade fidelity. Figure 3.3A shows a scan of interrogation time T and exhibits both decreasing contrast at longer T-time and a shift in the mean value. Plot A shows the unprocessed data and the 1400 point moving average employed to remove the mean value drift. Plot B shows the data after subtraction of this moving average with a fit of functional form described in equation 3.1 Plot C shows the residuals of plot B. It is clear from these plots that for small T, sampling and periodicity mismatches cause oscillations in the moving average, effectively damping the scan for small values of T. More careful processing would vary the sampling length with T to remove this artefact. It is also clear that the amplitude decay rate has not been successfully matched. As we are primarily interested in the accumulation of phase, these errors are small and do not result in a dropped fringe up to $T > 3500$ μs; the fit in plot B is sufficient to determine $\mathbf{g} \cdot \mathbf{k_{eff}}$.

As figure 3.3B encompasses such a large number of oscillations, I have included reduced range sections to highlight the main features of the data. Figure 3.4 shows a scan of interrogation time T in the range 500μs to 1500μs. The fit tracks the periodicity of the oscillations exactly, but has some mismatch in amplitude. Figure 3.5 is still tracking the periodicity of the oscillations; however the contrast is reduced, the amplitude mismatch has grown, and the residuals are approaching the amplitude of the oscillations. These two plots illustrate that the fit successfully matches the period of the oscillations.

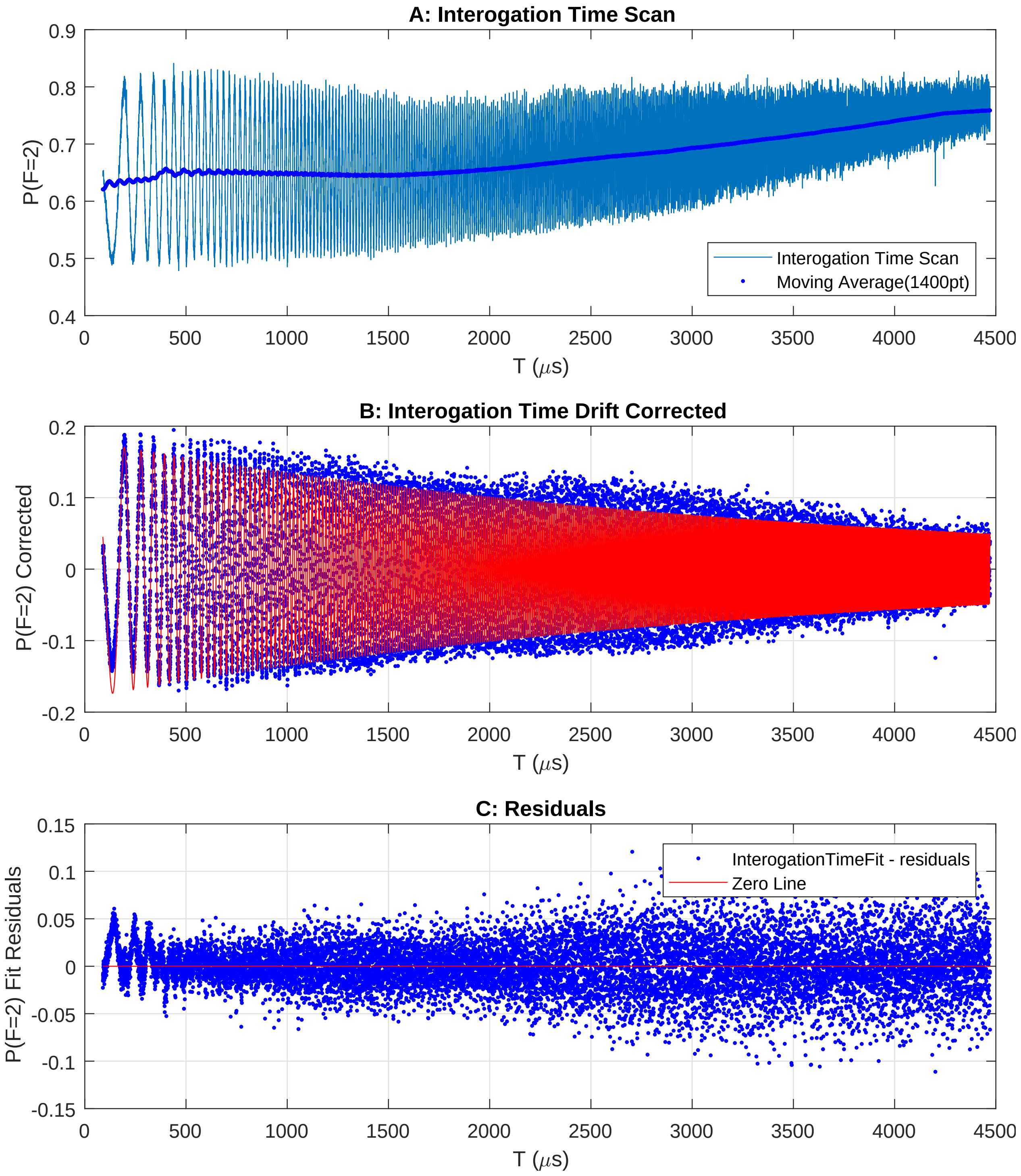

Figure 3.3: Plot A shows the raw results from an interrogation time scan and an overlaid 1400-point moving average used to remove the offset. This corrected data is shown in plot B along with the result of a fit of the form equation 3.1. Plot C shows the residuals of this fit. The following experimental parameters were used: $t_\pi = 8\ \mu s$, Raman carrier detuning of $\Delta = -37$ GHz (i.e. red) of the repump laser, with 180 mW in the down-going Raman beam and 250 mW in the up-going.

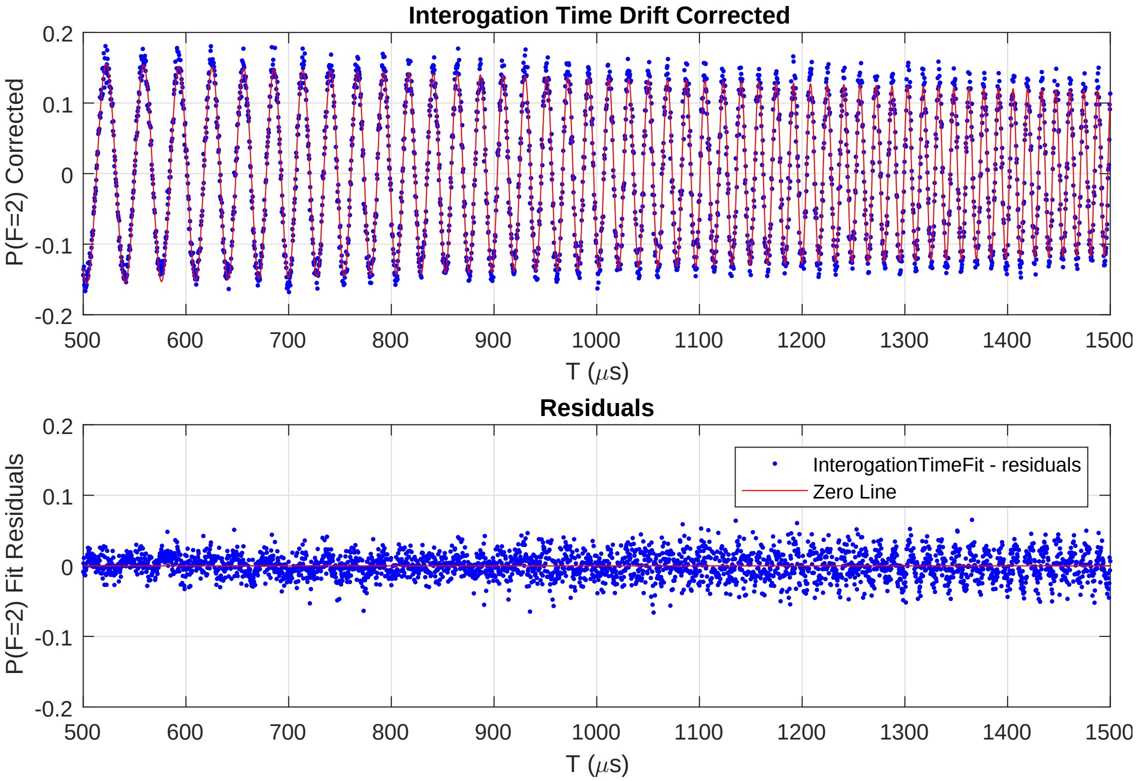

Figure 3.4: T-time (500 μs to 1500 μs) against drift corrected population with the fit and residuals shown.

The reduction in contrast at longer T-times is believed to be caused by phase noise introduced between the two fibres delivering the Raman beams to the experiment. Thermally and mechanically stressing these fibres causes phase fluctuations that completely obscure fringes at $T = 2$ ms. A fast optical phase lock after the fibres would reduce this phase noise and allow the experiment to operate at longer T-times, enhancing sensitivity.

The trial function used in figure 3.3B is: (all times are in microseconds)

$$f(x) = a_1 e^{-a_2 x} \sin\left[b_1\left(x^2 + t_\pi\left(1 + \frac{2}{\pi}\right)x\right) + b_2\right] \tag{3.1}$$

Coefficients and 95% confidence bounds are shown in table 3.1.

Coefficient	Value	95% Confidence interval		
a1	0.1808	0.1789	0.1826	
a2	2.899	2.843	2.955	$\times 10^{-4}$
b1	1.576668	1.576654	1.576682	$\times 10^{-4}$
b2	1.44	1.432	1.447	

Table 3.1: Fit coefficients for equation 3.1

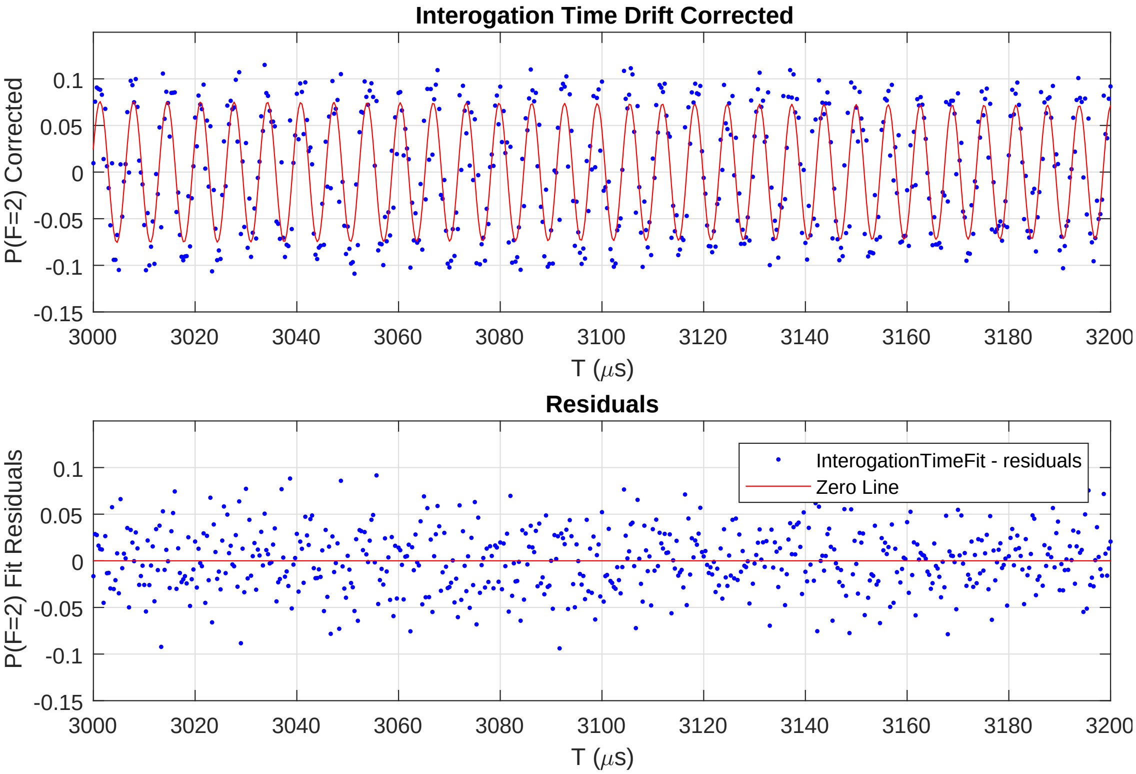

Figure 3.5: T-time (3000 μs to 3500 μs) against drift corrected population with the fit and residuals shown. Note the change in axis scales when compared to figure 3.4.

Comparing equation 2.39 and equation 3.1 reveals that b_1 can be used to calculate $g\cos(\theta)$. Making the appropriate substitutions gives:

$$g\cos(\theta) = 9.79039 \pm 4 \times 10^{-5} \text{ m s}^{-2} \tag{3.2}$$

The above bounds correspond to the 1-σ_g confidence interval and are based entirely on uncertainties in the fit. They should be taken as an indication of measurement precision rather than accuracy. We have not characterised the possible systematics here. The error in $g\cos\theta$ has been taken to match the 1-σ uncertainty in b1; the uncertainties in $\mathrm{k_{eff}}$ and T are significantly smaller than the reported uncertainty in $g\cos\theta$ so this is reasonable.

3.6 Temperature

The Doppler sensitive nature of the Raman pulses allows us to use them to measure the temperature of our atom source [77]. We follow the method of Wu [60]. Recall the interferometry sequence $\frac{\pi}{2} \rightarrow \pi \rightarrow \frac{\pi}{2}$

where the pulses are separated by the interrogation time T. We vary the second interrogation time period $T_2 \rightarrow T_2 + \delta T$ causing the interferometer to fail to close. We observe a Gaussian contrast envelope in δT:

$$\chi = \exp\left(-\frac{\delta T^2}{2/(k_{\text{eff}} v_{\text{rms}})^2}\right) \tag{3.3}$$

Where v_{rms} is the one-dimensional RMS velocity of the cloud in the direction of the Raman beams. The one dimensional temperature T_a is given by: [78]

$$T_a = \frac{m v_{\text{rms}}^2}{k_B} \tag{3.4}$$

Figure 3.6 shows such a δT scan showing sinusoidal oscillations in δT with the expected Gaussian envelope. Using equation 3.4 we find $T_a = 1.9\ \mu$K. This temperature was surprisingly low given the fact that sub-Doppler cooling had not been optimised. The cause of this anomaly was velocity selection from the long pulse time $t_\pi = 8\ \mu s$. The effective linewidth and resulting velocity class addressed by a Doppler sensitive Raman pulse is determined by the pulse duration. Equation 3.5 states this relationship, where $\sigma_{t\pi}$ is the $1/\sqrt{e}$ width of a Gaussian pulse [79]. In figure 3.6 $t_\pi = 8\ \mu$s corresponds to a Doppler width of $T_D \simeq 2\ \mu$K, consistent with both the measured temperature and the fact that velocity selection was responsible.

$$T_{\text{Doppler}} = \frac{m}{k_B (k_{\text{eff}} \sigma_{t_\pi})^2} \tag{3.5}$$

To address the full velocity distribution a shorter pulse was needed. Unfortunately the loss in contrast at long T-times with short pulse lengths prevents us from taking a single shot measurement. Instead we take a phase scan at several values of δT and measure the contrast of each scan. Plotting fringe visibility against δT allows us to measure the Gaussian envelope, at T-times too short to facilitate single shot measurement (100 μs in this case). Whilst long T times can result in lower measured temperatures, with hotter atoms leaving the interferometry region, this does not occur in this case. For the 5.4 ms total free-fall time used in figure 3.6, this effect becomes significant for temperatures above 1 mK (i.e. 100 times hotter).

Figure 3.7 was taken with $t_\pi = 2.0\ \mu$s and indicates a cloud temperature $T_a = 10.9\ \mu$K. This t_π results in velocity selection in clouds with temperatures above $\sim 30\ \mu$K so this measurement is limited by the true velocity profile of the cloud. Additional measurements taken at $t_\pi = 1.1\ \mu$s indicate an almost identical cloud temperature with velocity selection occurring at the $\sim 100\ \mu$K level, providing further confirmation that 10.9 μK is representative of our sample.

Optimisation of our polarisation gradient cooling should allow us to reach cloud temperatures of at least

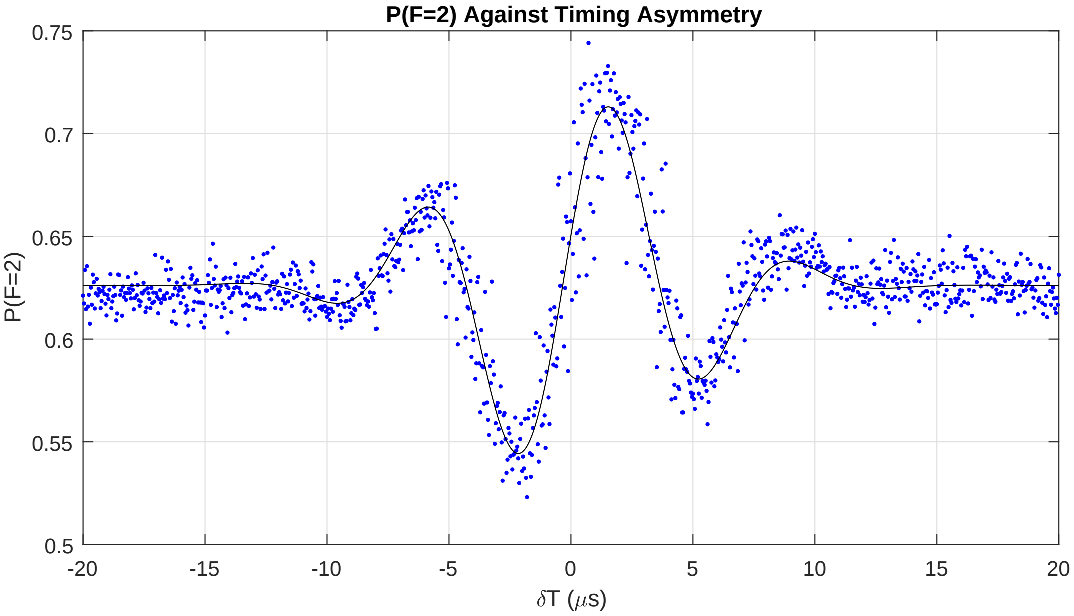

Figure 3.6: A scan of δT against population transfer efficiency. The fit indicates a cloud temperature of 1.9 μK. For this scan $T = 2.7$ ms. The same experimental parameters were used as in the interrogation time scan figure 3.3.

$T_a = 5.5$ μK [80] as demonstrated by McGuinness et al. in a similar experiment operating at high-bandwidth (over 100 Hz). Lower temperatures are routinely achieved but not at high bandwidth [81].

3.7 Large Power and Detuning

The high power of our Raman laser system should facilitate short pulses and large detunings, allowing LMT operation. For an interferometer running at short interrogation times, a short π-pulse allows us to address a far larger velocity class of atoms, with a corresponding increase in sensitivity. Large detunings reduce the probability of spontaneous emission during the interferometry pulse, increasing pulse fidelity. For large momentum transfer (LMT) interferometers this increase in fidelity is significant. Even a small loss in pulse fidelity rapidly degrades the contrast and sensitivity over the many pulses used for LMT. The potential enhancement offered by LMT motivates additional work to consider its use in this high bandwidth system [39, 82]. The system size and power consumption required to generate high power Raman beams may initially seem to prohibit their use in compact field deployable systems. In the following chapters we discuss optical cavity enhancement which provides a route to generating these high power Raman beams with compact, low power lasers.

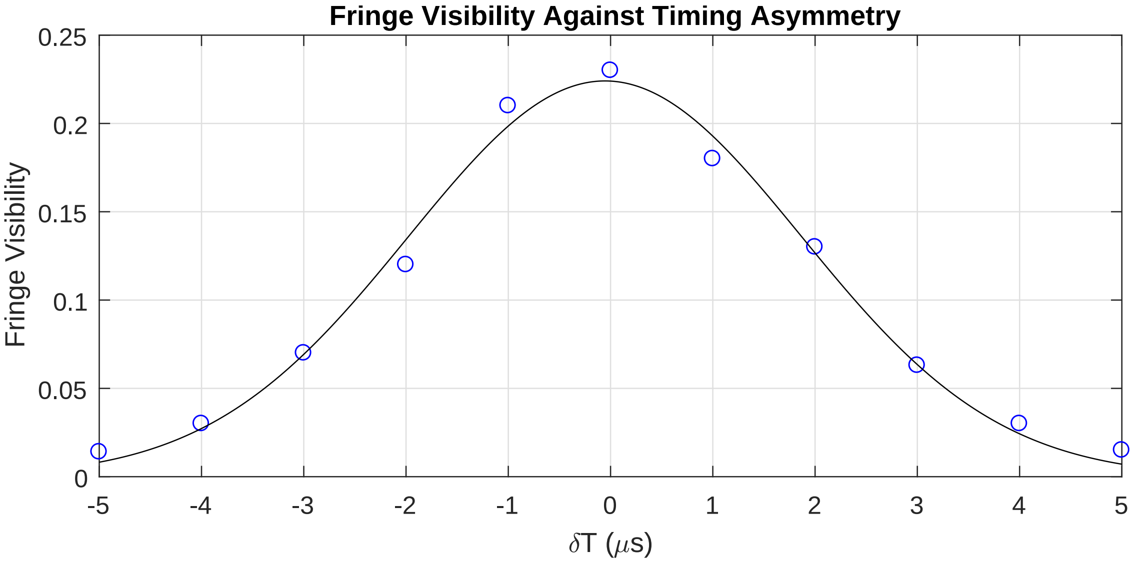

Figure 3.7: A scan of δT against fringe visibility. The Gaussian visibility envelope corresponds to a cloud temperature $T_a = 10.9\ \mu$K.

3.8 Conclusion

We have demonstrated a laboratory based, high bandwidth atom interferometer instrument and have performed an incipient gravity measurement with a fractional statistical uncertainty of $\sigma_g/g = 4.4 \times 10^{-6}$ where g is the acceleration due to gravity. This instrument will act as a platform for exploring the fundamental limitations of atom interferometer techniques. The dominant noise source is phase noise between the two Raman beams induced by vibration, stress, and thermal effects in their respective fibres. Significant improvements can follow from the addition of a phase lock on the Raman beam delivery. Finalisation of the proposed cooling and detection laser will further increase performance due to enhanced frequency stability and increased power. The construction of a powerful Raman laser allows an investigation into Raman pulse parameters with much larger single-photon Raman detuning and higher Rabi frequencies, both of which can enhance the atom-optical pulse efficiency. The improvements will enable large momentum transfer matter-wave beamsplitters that can increase sensitivity for a given T-time. This regime has not been explored at high bandwidth before.

CHAPTER 4

OPTICAL CAVITIES THEORY

A stable optical cavity is an arrangement of mirrors and other optical elements, arranged such that an optical field can circulate and is left unchanged in both phase and spatial mode by successive round trips. Where round trip losses are low, the lifetime in the cavity is long and photons complete many round trips before they are lost. Constructive interference between the input and circulating fields can result in a circulating intensity that greatly exceeds the input, resonant enhancement. Self consistency in phase is only achieved by narrow frequency bands, known as longitudinal modes, which satisfy the resonance condition of the cavity. A self consistent spatial mode is only possible for some combinations of cavity elements; these restrictions are known as geometric constraints. Cavity design is an exercise in exploiting these properties to achieve a desired optical field whilst satisfying these geometric and frequency constraints and minimising sensitivity to perturbations. Ray transfer matrix methods greatly simplify the optimisation process by allowing an optical cavity to be parameterised at a given reference plane by a single ABCD matrix [83].

In the following chapter we are going to analyse the properties of optical cavities and develop the tools we need to design optical cavities for atom interferometry. For further information the reader should refer to Lasers by Siegman which was the primary reference for this chapter [83].

4.1 Circulating Fields

The circulating field, $\mathbf{E}_{circ}$, within an optical cavity is the sum of the transmitted fraction of the field incident on the input mirror, with the field that has completed a round trip.

$$\mathbf{E}_{circ} = it_1\mathbf{E}_{inc} + g_{rt}(\omega)\mathbf{E}_{circ} \tag{4.1}$$

Where the amplitude transmission coefficient is t_1 and the round trip gain represented by $g_{rt}(\omega)$, includes all reflection and absorption losses, along with phases arising from wave propagation. The i in front of the transmission coefficient takes account of the π phase shift accumulated through transmission over reflection.

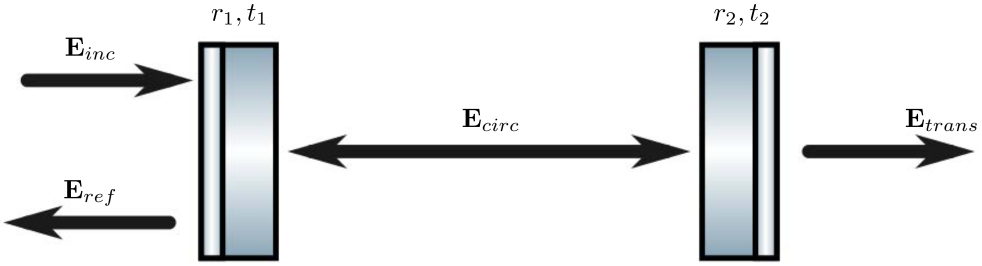

Figure 4.1: The electric fields and amplitude coefficients for a two mirror cavity. [84]

For a passive two mirror cavity with negligible internal loss, amplitude reflection coefficients r_1 and r_2, and round trip path length L_{RT} the gain is is given by equation 4.2.

$$g_{rt}(\omega) = r_1 r_2 \exp\left\{\frac{-i\omega L_{RT}}{c}\right\} \tag{4.2}$$

Where c is the speed of light and the radian frequency of the radiation is given by ω. Conservation of energy requires that for any mirror the reflection and transmission coefficients obey the following relation: $r_i^2 + t_i^2 = 1$. We can rearrange to see the intracavity field enhancement factor:

$$\frac{\mathbf{E}_{circ}}{\mathbf{E}_{inc}} = \frac{it_1}{1 - g_{rt}(\omega)} = \frac{it_1}{1 - r_1 r_2 \exp(-i\omega L_{RT}/c)} \tag{4.3}$$

4.1.1 Free Spectral Range

The denominator takes a minimum value when $\exp(-i\omega p/c) = 1$.

$$\frac{\omega L_{RT}}{c} = 2\pi n \tag{4.4}$$

These are the longitudinal modes of the cavity, and are the frequencies for which maximum resonant enhancement occurs. Away from these frequencies there is a rapid decay in the circulating field, so intracavity fields must operate close to these frequencies to benefit from resonant enhancement. These resonance peaks are separated by a frequency corresponding to an additional oscillation over the round trip path length. This frequency difference is known as the free spectral range:

$$\nu_{FSR} = \frac{c}{L_{RT}} \tag{4.5}$$

4.2 Power Enhancement

Circulating intensity is the figure of merit for cavity enhancement. Assuming we are on resonance ($\omega = \omega_0$) and then taking the modulus squared of equation 4.3 we find the circulating intensity.

$$\left.\frac{I_{circ}}{I_{inc}}\right|_{\omega=w_0} = \frac{(t_1)^2}{[1 - g_{rt}(\omega_0)]^2} = \frac{(t_1)^2}{[1 - r_1 r_2]^2} \tag{4.6}$$

Whilst the lower case r and t represent field amplitude coefficients, the upper case R and T represent the reflectance and transmittance for incident energy. Conservation of energy mandates that $R = r^2$, $T = t^2$, and $T + R = 1$.

4.2.1 Delta Notation:

Whilst the above treatment is sufficient for a two mirror cavity with no internal losses, we wish to describe more complex systems with lossy intracavity elements. We can describe these with delta-notation, where the approximate expression is valid for small round trip losses.

$$R_1 \equiv e^{-\delta_1} \simeq 1 - \delta_1 \tag{4.7}$$

In this notation we can consider all the contributions to round trip loss. Internal losses are grouped together under δ_0, and each mirror will have its own contribution δ_i with the input mirror given by δ_1. The approximate expression is valid for low loss cavities, when $\delta_i \ll 1$.

$$g_{rt} = r_1 r_2 e^{-\delta_0/2} = e^{-(\delta_1+\delta_2+\delta_0)/2} \simeq 1 - (\delta_1 + \delta_2 + \delta_0)/2 \tag{4.8}$$

For a low loss cavity on resonance we can rewrite equation 4.6 with delta notation:

$$\left.\frac{I_{circ}}{I_{inc}}\right|_{\omega=\omega_0} \simeq \frac{4\delta_1}{(\delta_0 + \delta_1 + \delta_2)^2} \tag{4.9}$$

If the input mirror transmission is equal to the round trip loss from the rest of the cavity $\delta_1 = \delta_2 + \delta_0$,

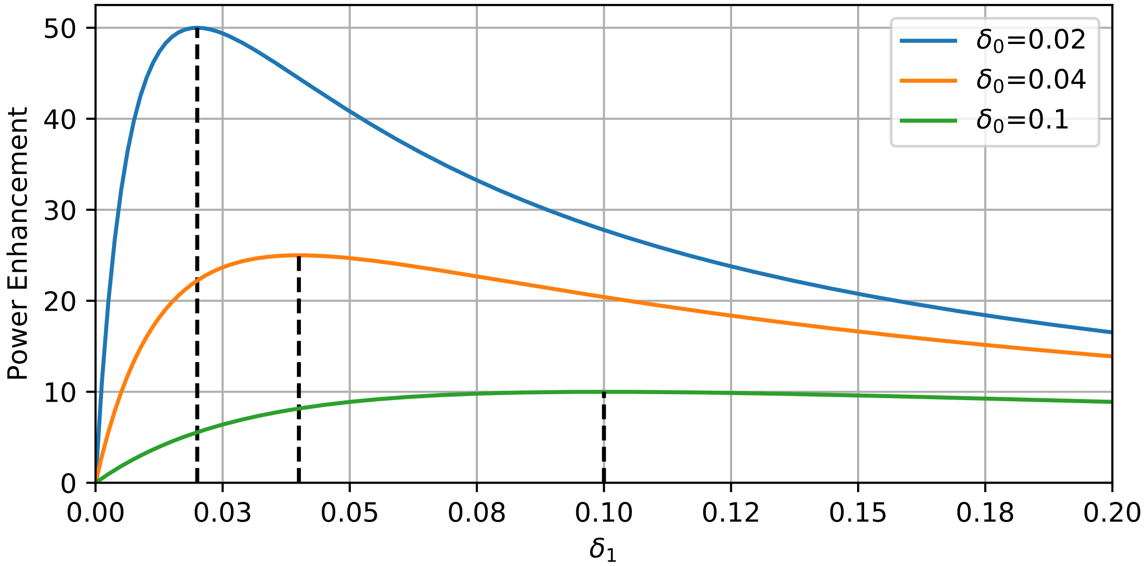

Figure 4.2: Power enhancement against δ_1 for different values of round trip loss δ_0. Impedance matching is indicated by the dashed lines. We have assumed $\delta_2 = 0$ which is valid for the cavities considered here where internal losses dominate.

then the cavity enhancement is $1/\delta_1$, and the system is impedance matched. Similar analysis of the reflected signal reveals that in the impedance matched case, the reflected signal vanishes. If the majority of the round trip loss is the input mirror i.e. $\delta_1 \gg \delta_2 + \delta_0$ then the enhancement tends to $4/\delta_1$, known as an over-coupled cavity. Reducing round trip losses increases the circulating intensity, and to maximise enhancement the only source of loss should be the incoupling mirror. Unfortunately, the cavities considered in the rest of this thesis $\delta_0 \simeq 10\%$ is much larger than the transmissions of commonly available mirrors, and we find that impedance matching gives us optimum power enhancement. We are able to simplify some expressions by combining all round trip losses, including the end mirrors, into a single term $\delta_c = \delta_0 + \delta_1 + \delta_2$

4.2.2 Finesse

Atom interferometry requires the frequency of the input laser to be chirped. As a result the off-resonant behaviour of the cavity must be considered, and for successful intracavity operation the linewidth of the cavity should be matched to the interferometer chirp. In chapter 5.1 we explore this limit in more detail and describe an alternative approach using a Pockels cell to maintain cavity resonance whist chirping the lasers for interferometry. The linewidth of the cavity resonance peaks ν_{FWHM} (full-width-at-half-maximum) is calculated from equation 4.6. The approximate expression is valid when the round trip loss is low, $g_{rt} \simeq 1$ or $\delta_c \ll 1$.

$$\Delta\nu_{FWHM} = \frac{2c}{\pi p}\sin^{-1}\left(\frac{1-e^{-\delta_c/2}}{2\sqrt{e^{-\delta_c/2}}}\right) \simeq \frac{c}{p}\left(\frac{1-g_{rt}}{\pi\sqrt{g_{rt}}}\right) \tag{4.10}$$

We define a new quantity called finesse, which is a measure of the resolving power of the cavity. Once again, the approximations holds if the round trip losses are small.

$$\mathcal{F} \equiv \frac{\pi\sqrt{g_{rt}}}{1-g_{rt}} \simeq \frac{\nu_{FSR}}{\nu_{FWHM}} \simeq \frac{2\pi}{\delta_c} \tag{4.11}$$

4.2.3 Cavity Lifetime

After the input beam is removed the circulating intensity persists, decaying exponentially over a number of round trips. From the definition of δ_c the circulating intensity decays as follows:

$$I_c(t) = I_0 e^{-\delta_c ct/L_{RT}} \tag{4.12}$$

The cavity lifetime (e^{-1}) is then given by equation 4.13 where we have substituted δ_c from equation 4.11 in its low loss limit.

$$\tau_c = \frac{\mathcal{F}L_{RT}}{2\pi c} \tag{4.13}$$

For the cavity described in chapter 6 with $L_{RT} = 1.4$ m and $\mathcal{F} = 35$, this lifetime is 26 ns, i.e. significantly shorter than typical μs pulse durations, so the effects of cavity lifetime are not significant. For long, high finesse cavities this lifetime can become comparable to or exceed the target pulse duration, resulting in severe pulse elongation, described by the cavity bandwidth limit [50]. In chapter 8 we describe a method to circumvent this limit enabling the operation of atom interferometers in long, high finesse cavities with lifetimes substantially longer than the pulse duration.

4.2.4 Compromise

For atom interferometry in a cavity we seek to maximise power enhancement whilst remaining resonant with the cavity for the duration of the laser chirp. In a conventional cavity this requires a broad linewidth. Examination of equations 4.9 and 4.11 reveals that these requirements are contradictory as power enhancement and linewidth are inversely proportional. The following expression is valid for a low loss impedance matched cavity on resonance:

$$\left.\frac{I_{circ}}{I_{inc}}\right|_{\omega=\omega_0} = \frac{\mathcal{F}}{\pi} \tag{4.14}$$

If we wish to increase the power enhancement we must reduce the linewidth of the cavity, which in turn limits the maximum chirp that can be achieved. Increasing the ν_{FWHM} at constant linewidth will also increase the power enhancement, but reduces the optical path length of the cavity. In practice the minimum path length of the cavity is constrained by the size of the system and fundamentally by the maximum free-fall distance the system can accommodate, so this is not a free parameter.

4.3 Gaussian Beams

In resonator systems, beams generally obey the paraxial approximation, that is they only make small angles to the optical axis. Under this approximation, and considering a single transverse field, Maxwell's equations reduce to the scalar paraxial wave equation. The simplest solution is given by a Gaussian beam [83].

$$E(x,y,z) = \frac{1}{q(z)} \exp\left\{-ik\frac{x^2+y^2}{2q(z)} - ikz\right\} \tag{4.15}$$

The fast oscillatory ikz dependence will be factored out and omitted going forward. The complex radius of curvature q encodes the evolution of a Gaussian beam during propagation.

$$\frac{1}{q} = \frac{1}{R(z)} - i\frac{\lambda}{\pi w(z)^2} \tag{4.16}$$

$R(z)$ is the real radius of curvature of the beam, and $w(z)$ is the radius at which the amplitude falls to $1/e$ (this is $1/e^2$ radius for intensity). Along the propagation direction q varies as $q(z) = q_0 + z - z_0$ where q_0 and z_0 are both defined in the same plane [85]. Once q has been determined, $R(z)$ and $w(z)$ can both be found by taking the real and complex parts of $1/q$.

$$w(z) = w_0\sqrt{1+\left(\frac{z}{z_R}\right)^2} \tag{4.17}$$

$$R(z) = z + \frac{z_R^2}{z} \tag{4.18}$$

Where z_R is the Rayleigh range and w_0 is the beam waist (radius at the focus). For simplicity we have assumed the beam waist is located at $z = 0$. One Rayleigh range away from the waist of a Gaussian beam the area of the beam doubles.

$$z_R = \frac{\pi w_0^2}{\lambda} \tag{4.19}$$

4.3.1 Gouy Phase

The Gouy phase shift is the additional shift acquired by a propagating beam compared to a plane wave over the same distance.

$$\psi_G(z) = -\arctan\left(\frac{z}{z_r}\right) \tag{4.20}$$

These phase shifts also arise in cavity modes, and the size of this shift is the key parameter in determining the spatial mode filtering performance. We will revisit this in section 4.5.1.

We have now established all the fundamentals we will need to analyse beam propagation in cavities. To proceed we need a better way of analysing the systems than repeated applications of the paraxial wave equation. For this we use ABCD matrices.

4.4 ABCD Matrices

ABCD matrices provide a method of transforming paraxial beams through a linear optical system. Each optical element is represented by an ABCD matrix and beam propagation through a multi-element system is accomplished with matrix multiplication. This is a powerful approach for computing the effect of multi-element optical systems. In equation 4.21 we present the general transformation for a paraxial beam at a distance x from the optical axis with propagation angle θ. We simplify these matrices, following the reduced slopes convention, by multiplying the angle θ by the refractive index in the media n [83].

$$\begin{pmatrix} x' \\ n'\theta' \end{pmatrix} = \begin{pmatrix} A & B \\ C & D \end{pmatrix} \begin{pmatrix} x \\ n\theta \end{pmatrix} \tag{4.21}$$

4.4.1 Specific Matrices

ABCD matrices for a thin-lens of focal length f, a curved mirror with radius of curvature R, free space propagation over a path length L refractive index n are given below.

$$M_{Lens} = \begin{pmatrix} 1 & 0 \\ -1/f & 1 \end{pmatrix} \tag{4.22}$$

$$M_{Mirror} = \begin{pmatrix} 1 & 0 \\ -2/R & 1 \end{pmatrix} \tag{4.23}$$

$$M_{FreeSpace} = \begin{pmatrix} 1 & L/n \\ 0 & 1 \end{pmatrix} \tag{4.24}$$

4.4.2 Cavity ABCD

ABCD matrices can also be be used to transform Gaussian beams in the following way:

$$q_2 = \frac{Aq_1 + B}{Cq_1 + D} \tag{4.25}$$

A complete optical system can then be described by a single ABCD matrix generated by multiplying together matrices for each of its elements. The output beam from such a system can be calculated with the ABCD transform. In the analysis of optical cavities we frequently encounter the half-trace of the matrix which we denote by m to simplify expressions in the following discussion.

$$m = \frac{A + D}{2} \tag{4.26}$$

We can apply ABCD matricies to optical cavities, representing each optical element by its ABCD matrix and using matrix multiplication can generate an ABCD matrix for the round trip. The ABCD matrix will change depending on the reference plane, i.e. the starting plane for the ABCD matrix propagation, but the half trace m is independent of this. The requirement for self consistency on a round trip leads to the following expression:

$$q_1 = \frac{Aq_1 + B}{Cq_1 + D} \tag{4.27}$$

We can solve for q and find:

$$\frac{1}{q_a}, \frac{1}{q_b} = \frac{D - A}{2B} \mp \frac{1}{B}\sqrt{\left(\frac{A + D}{2}\right)^2 - 1} \tag{4.28}$$

Comparison with equation 4.16 shows that one of these two solutions (which depends on the sign of B) represents a confined Gaussian beam with a positive real spot size w provided:

$$-1 \leq m \leq 1 \tag{4.29}$$

This solution can be shown to be stable against perturbations in the complex beam parameter q. Whether or not a particular arrangement of optical elements can support a stable mode can be determined by simply examining the half-trace of the matrix, m.

4.4.3 Cavity Properties from ABCD

Comparing equation 4.16 for the complex beam parameter of a Gaussian beam with the solutions of equation 4.28 we can find the radius of curvature in the plane at which the matrix is evaluated:

$$R = \frac{2B}{D - A} \tag{4.30}$$

Similarly the beam radius in this reference plane is given by the following:

$$w^2 = \frac{|B|\,\lambda}{\pi}\sqrt{\frac{1}{1 - m^2}} \tag{4.31}$$

Atom interferometry requires large beams, and the beam radius can be increased by either increasing the $|B|$ parameter, or by pushing $m \to \pm 1$. The B parameter varies with the reference plane at which it is evaluated, but it has dimensions of length, and for beams close to collimated is comparable to the physical length of the cavity. This clearly cannot be increased arbitrarily. Pushing $m \to \pm 1$ is also problematic, as $m = \pm 1$ represents the boundary of stability, and the sensitivity of the cavity to perturbations grows dramatically in this regime. The m parameter also plays a central roll in the mode filtering performance of the cavity as we shall see in the following sections. We shall revisit cavity modes in chapter 5.3.1, and show that an intracavity telescope offers an alternative route to achieving large modes in a compact geometrically stable cavity.

4.5 Higher Order Modes

An optical cavity only supports spatial modes with well defined wavefront profiles. More general solutions to the paraxial wave equation include higher order transverse modes, with more complex wavefronts. These can be decomposed with Hermite-Gaussian or Laguerre-Gaussian modes. Which decomposition is appropriate depends on the symmetry properties within the resonator. Such higher order modes have a larger diameter than the fundamental mode in the same cavity and have higher spatial frequencies in their transverse mode profiles.

Atom interferometers require flat optical phase fronts to deliver measurements with low uncertainty and high stability. In the best two-photon atom interferometers wavefront aberrations are the leading source of uncertainty [34]. By coupling into the fundamental mode of the cavity we are able to exploit the discrete mode profiles supported by the cavity to provide filtering of the spatial mode and achieve flat optical wavefronts.

We achieve our mode filtering in two ways: spatial mode matching of the input beam to the fundamental mode we wish to excite, and control of the cavity geometry to make higher order modes non-degenerate in frequency. The fundamental mode can be uniquely addressed in frequency and parasitic coupling to higher order modes is avoided. If the input beam is perfectly overlapped in position, angle and size with the fundamental mode then only the fundamental mode will be excited. This mode matching approach is fundamentally limited by the wavefront performance of the input optics. Higher performance is achieved by controlling the frequency spectrum of the higher order modes, to ensure the fundamental mode is non degenerate in frequency and can be uniquely addressed. This is achieved by manipulating the cavity's Gouy phase.

4.5.1 Gouy Phase in a Cavity

A cavity mode acquires Gouy phase on each round trip. The magnitude of this phase depends on the mode number in question and the geometry of the cavity. Higher order spatial modes acquire Gouy phase more quickly than the fundamental Gaussian mode and have different resonant frequencies. The magnitude of the Gouy phase acquired over a round trip is given by equation 4.32 for a higher order mode parameterised by indices p, q (e.g. $TEM_{p,q}$) in terms of the half-trace of the cavity m, and the sign of the B parameter [86].

$$\phi_{p,q} = \mathrm{sgn}(B)(p+q+1)\cos^{-1}(m) \tag{4.32}$$

A full statement resonance condition including the effect of Gouy phase is given in equation 4.33 [83] where L_{RT} is the round trip optical path length. The absolute frequency shift between this and the plane wave approximation we naively found in equation 4.4 is difficult to observe directly due to the complexity of measuring absolute frequencies in the optical domain. However, the presence and frequency spacing between higher order modes can be observed in the transmission signal of any cavity with imperfect mode matching.

$$\frac{\omega L_{RT}}{c} - \phi_{p,q} = 2\pi n \tag{4.33}$$

Higher order mode degeneracy will occur when $\phi_{p,q}$ is close to a multiple of π. The round trip Gouy phase can be controlled by changing the cavity geometry, with the critical metric being the half trace of the cavity m. Specific geometric changes used to control Gouy phase are described in chapter 5.4.1. Through careful tuning of the Gouy phase, the resonant frequencies of higher order modes can be shifted away from the fundamental mode frequency, providing spatial mode filtering. Whilst there are an infinite number of higher order modes, the increasing diameter of higher modes increases losses from finite apertures. As a result the behaviour can be effectively analysed by considering only the first few higher order modes.

4.6 Simulation

As we have seen cavity design requires the optimisation of a number of parameters. Stability m, mode radius w, and Gouy phase ϕ. In a multi-element resonator there are a large number of degrees of freedom specifically: spacing between the optics, and the focal lengths of optical elements, presenting us with a daunting parameter space. Fortunately we can be assisted with automation. I have written a python package that automates the matrix multiplication and analysis, allowing us to iterate over large numbers of cavities $\simeq 10^6$ varying multiple parameters. Physical insights, such as comparing Rayleigh ranges for different cavity sections can provide clues as to which parameters are more sensitive to variation. Physical constraints on the size of the cavity also reduce the area of the parameter space.

For the cavities in this thesis, we desire at least one section with a large near collimated spatial mode. We also require careful control of the Gouy phase to control higher order mode degeneracy and spatial filtering. We generate surface plots (beam radius and Gouy phase) with sensitive parameters on both axes. These allow us to quickly centre in on combinations resulting in stable modes, and then optimise these parameters for stability and higher order mode suppression. Details of the optimisation process are provided in the cavity design chapter 5. This software package is freely available and can be downloaded from the referenced link [87].

4.6.1 Limitations

The analysis presented in this chapter and the code both use the paraxial approximation and assume everything is perfectly aligned. This modelling was sufficient for the cavity constructed in chapter 6 and provides a good starting point for any cavity design, but may not provide the detail required for systems requiring higher performance. More sophisticated models should build on the approximations to include the effect of misalignment, including off axis beams and astigmatism. Misalignment can change stability properties of the cavity and shift the frequencies of higher order modes, lifting degeneracy between p and q values in the calculation of Gouy phase.

CHAPTER 5

CAVITY DESIGN

The ideal cavity for Raman atom interferometry has the following properties: large diameter collimated mode; power enhancement; non-degenerate higher order spatial modes; geometric stability and the ability to support two orthogonal polarisations and chirping laser frequencies; properties motivated in chapter 2. As we found in chapter 4 these requirements are contradictory, and impossible to achieve with conventional cavity geometries and optical techniques. Despite these challenges several approaches have been demonstrated each making different compromises between these parameters. Hamilton et al. [44] demonstrate cavity enhanced atom interferometry, generate power enhancement, avoid higher order mode degeneracy and maintain geometrical stability but sacrifice a large mode in the process whereas Riou et al. [49] present a cavity with a large mode but sacrifice higher order mode degeneracy and geometric stability. Neither of these cavities are able to support extended frequency chirps for the 2-photon Raman transitions (henceforth referred to as the Doppler limit), requiring either finesse and T-time limits or a horizontal geometry to avoid these being fatal. These compromises have prevented the benefits of cavity enhancement from being fully realised.

We will describe a novel design for a Doppler compensated, magnified cavity which avoids these compromises offering a large spatial mode, geometric stability, and tunable Gouy phase to lift higher order spatial mode degeneracy [2]. The cavity presented here is required to have a 0.4 m long large mode section to accommodate a vacuum chamber; it has a maximum height of around 1 m, and a target beam radius of $w = 2.5$ mm. We will describe the design process allowing similar cavities to be designed for the full spectrum of interferometry applications.

5.1 Doppler Shifts

Atoms in an atom interferometer aligned with gravity, experience Doppler shifted laser frequencies during free-fall, see figure 5.1. In rubidium-87, resonance with the atoms is maintained when the relative frequency of the Raman beams is chirped at $\alpha_{chirp} = 25.1\ \mathrm{MHz\,s^{-1}}$. This has the undesired effect of moving both laser frequencies away from cavity resonance, preventing beamsplitters entirely at long T times, see figure 5.2.

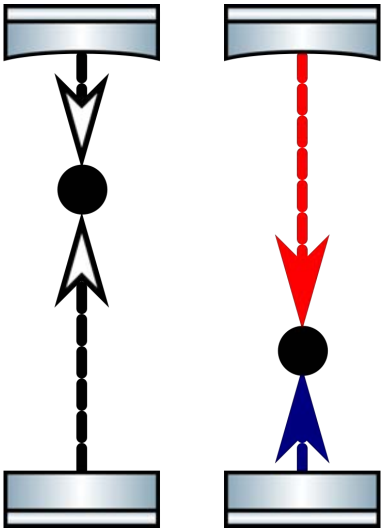

Figure 5.1: The lasers shift in frequency to compensate for the Doppler shift observed by the accelerating atoms. [84]

We arbitrarily define a maximum interrogation time T_{max}, to be that at which the Doppler shift has reduced the circulating intensity to half of its resonant value for the final beamsplitter pulse ($2T_{max}$ total free fall).

$$T_{max} = \frac{1}{2}\frac{\nu_{FSR}}{\alpha_{chirp}\mathcal{F}} = \frac{1}{2}\frac{c}{\alpha_{chirp}L_{RT}\mathcal{F}} \tag{5.1}$$

The free spectral range of the cavity is ν_{FSR}, α_{chirp} is the chirp rate, $\mathcal{F}$ is the finesse, and L_{RT} is the round trip optical path length of the cavity, twice its physical length for standing wave geometries. At T_{max} the Rabi frequency is reduced by a factor of two. Beamsplitter pulses at this Doppler shift must be twice as long as on resonance and the velocity class that can be addressed is also reduced by a factor of two. The sensitivity of circulating intensity to perturbations in laser frequency or cavity length are all dramatically increased as the laser moves off resonance. The first order insensitivity on resonance is replaced by the steep gradient of the Lorentzian Cavity transmission function [83].

For longer cavities the free spectral range decreases and the linewidth decreases proportionally. A cavity

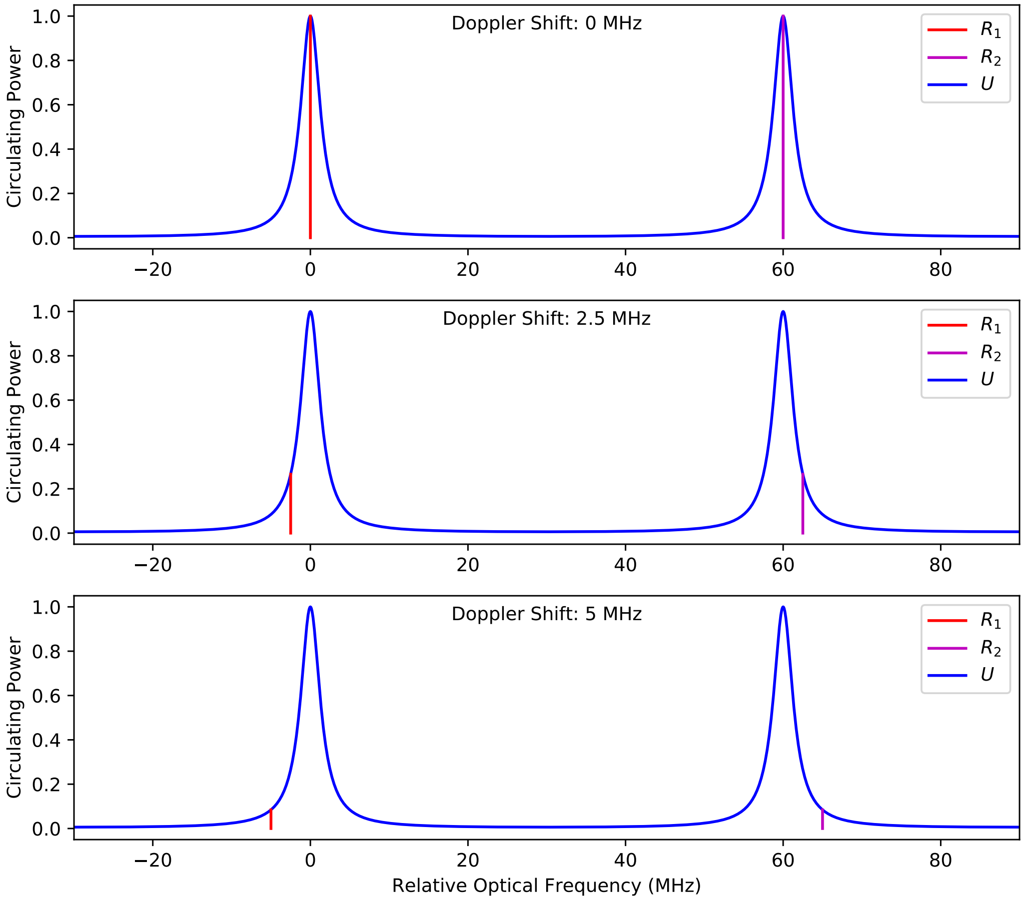

Figure 5.2: Uncompensated Doppler shift: Tracking the Doppler shift moves the lasers away from cavity resonance. This greatly reduces the resonant power enhancement and increases the sensitivity of the circulating power to perturbations in the cavity length. The cavity response is shown by U and the Raman lasers are indicated by R_1 and R_2. The cavity parameters for this synthetic data ($L_{RT} = 5$ m, $\mathcal{F} = 20$) were selected for clarity.

of round trip length 20 m which might fit round a large optical fountain has a free spectral range of only 15 MHz which even at the modest finesse of 100 gives 150 kHz line width. This cavity is limited to free-fall durations of 5.7 ms, defeating the point of building the large fountain in the first place. For higher finesse cavities, the linewidth decreases proportionally and the free-fall time over which resonance can be maintained is further reduced. These effects result in increased susceptibility to environmental noise and smaller atom numbers at the output of the interferometer. More severely, the sensitivity of an interferometer scales with the square of the interaction time, so Doppler limited performance severely restricts the achievable sensitivity. This is the central limit in existing cavity enhanced interferometers [47, 49–51].

5.2 Pockels Effect for Doppler Compensation

We solve the Doppler shift problem through the use of an an intracavity electro-optic crystal, a Pockels cell [88]. The Pockels cell induces a voltage controlled birefringence to the cavity increasing the optical path length in the slow axis with respect to the fast axis. This lifts the degeneracy between two orthogonally polarised cavity modes and shifts their resonant frequencies allowing them to be independently tuned, see figure 5.3. We use orthogonal linearly polarised Raman beams to implement our atomic beamsplitters with the polarisation axes aligned with the axes of our Pockels cell. This is consistent with the requirements of atom interferometry and compatible with the requirements of the Pockels cell. The size of the shift is linear in applied voltage and can be ramped smoothly up to the half-wave-voltage ($\sim$ kV) inducing a relative frequency shift in the resonance conditions of $\nu_{FSR}/2$ in a single pass travelling wave cavity and ν_{FSR} in a double pass standing-wave cavity as presented in this work.

The slew rate for Doppler compensation is given by equation 5.2. For metre scale cavities such as the system described in chapter 6 this is only 400 V/s which is readily achievable.

$$\frac{dV}{dt} = \frac{2}{N_{Passes}} \frac{\alpha_{chirp}}{\nu_{FSR}} V_{\lambda/2} \tag{5.2}$$

Pockels cells are bi-polar so sweeping the voltage from $-V_{\lambda/2} \rightarrow V_{\lambda/2}$ allows the relative frequency to be varied by ν_{FSR} in a travelling wave cavity and $2\nu_{\mathrm{FSR}}$ in a standing wave cavity. If longer sweeps are required, the resonance condition is maintained by reversing the polarity of the applied voltage between pulses and noting that the longitudinal modes now in use are separated by an additional free spectral range. In a travelling wave resonator a double length Pockels cell is required to achieve the same arbitrary relative shifts.

The Pockels cell also lifts the restriction on cavity lengths. In previous work the free spectral range ν_{FSR} had to be precisely tuned to ensure both Raman beams (separated by ν_{HFS}) resonate with the cavity simultaneously. This is satisfied when $\nu_{HFS} = N\nu_{FSR}$, such that the frequency splitting between Raman beams is an integer multiple of ν_{FSR}. By allowing the initial Pockels cell voltage to take a non-zero value, resonance can be achieved for both Raman beams without restricting ν_{FSR}. In a system where one of the Raman frequencies is generated by electro-optic modulation, having a non-integer ν_{FSR} separation carries the additional benefit of suppressing unwanted sidebands which would otherwise cause AC-stark shifts. In the integer multiple case these sidebands will always be co-resonant. The degree of suppression will vary as the Pockels cell is scanned for Doppler shifts and there will be times at which these sidebands co-resonate. This problem is further complicated by the resonant frequencies of higher order spatial modes. A full analysis

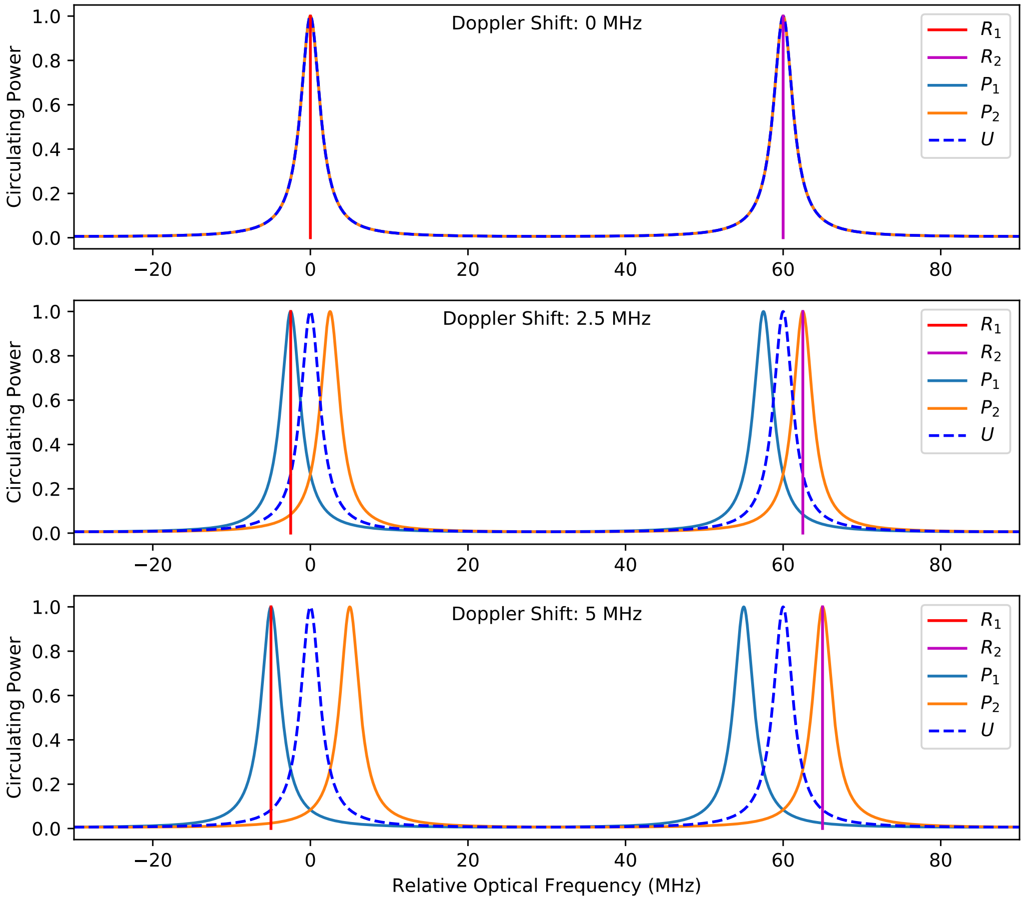

Figure 5.3: Compensated Doppler shift: Applying a voltage to the Pockels cell lifts the degeneracy between resonance peaks for the two polarisations. With the correct ramp rate, the shifting peaks track the frequency of the chirping laser beams and compensate for the Doppler shift. The cavity response for the two polarisations P_1 and P_2 track the chirping Raman lasers R_1 and R_2. The uncompensated cavity response is labelled U. The cavity parameters for this synthetic data ($L_{RT} = 5$ m, $\mathcal{F} = 20$) were selected for clarity.

of pulse timing, cavity ν_{FSR}, and Gouy phase will allow these co-resonances to be avoided. In chapter 7.6 we examine the use of Pockels cells in travelling wave cavities.

This technique compensates for Doppler shifts for arbitrarily large cavities of high finesse, removes restrictions on the possible cavity lengths, and dramatically reduces sensitivity to environmental and technical noise sources. For long, high finesse cavities with a lifetime comparable with the pulse duration, distortion of the temporal profile of the pulses becomes significant and further constraints apply [49, 50]. In chapter 8 we discuss a scheme to circumvent this limit.

5.3 Mode diameter

High fidelity beamsplitter pulses in atom interferometry require large laser beams compared to the millimetre scale atomic clouds. This maximises intensity homogeneity over the atomic ensemble, improves contrast, and minimises dephasing and losses due to finite temperature cloud expansion [89]. In an optical cavity this requires a large spatial mode diameter. As we saw in chapter 4.4.3 the $1/e^2$ radius, w, of the Gaussian eigenmode of a stable resonator is given by equation 5.3 in the reference plane at which the ABCD matrix is evaluated. The wavelength λ is 780 nm.

$$w^2 = \frac{|B|\,\lambda}{\pi}\sqrt{\frac{1}{1-m^2}} \tag{5.3}$$

The mode diameter can be increased in two ways, increasing $|B|$ or pushing $m \to \pm 1$ [83]. As $m \to \pm 1$ the cavity becomes degenerate to higher order modes, negating the mode cleaning advantage and approaching the edge of geometric stability. To increase the mode radius w of our 0.69 m long cavity from its confocal value[1] of 0.293 mm to the 2.52 mm achieved here would require $m \to 0.9985$. This would necessitate impractically large mirror curvatures approaching 2 km; for a 1 inch optic this corresponds to a deviation from planar of $< \lambda/18$. Control of the m parameter is therefore not a good technique for producing large modes.

The $|B|$ parameter has dimensions of length and in general varies with location within the cavity. However for cavities of interest with beams close to collimated, B is comparable to the physical length of the cavity. The length of the cavity cannot be practically increased in most systems, and the weak scaling on the length $w \propto \sqrt{|B|}$ makes this an ineffective approach for all but largest systems. Fortunately there is a more effective method to increase B.

5.3.1 Intracavity Telescope

An intracavity telescope focused close to infinity, magnifies the beam in one section of the cavity increasing $|B|$ in the large mode section [83, 90, 91]. Selection of the cavity end mirrors, focal lengths of the telescope elements and spacing between these elements are the outstanding challenge. A schematic for a magnified linear cavity is given by figure 5.4.

For the system presented here we choose planar mirrors at the ends of the cavity. The curvature of the cavity mode matches the curvature of the end mirrors, so planar mirrors are coincident with waists. For atom interferometry we require a large beam with minimal divergence so wish to operate close to a beam waist,

---

[1] The mode radius at the centre a confocal cavity of equal length. A confocal cavity has two identical curved mirrors with focal points coinciding at the centre of the cavity [83].

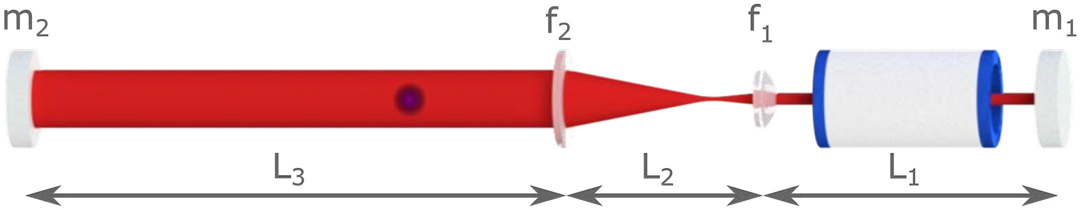

Figure 5.4: This is a general schematic for a standing wave magnified linear cavity. The small waist and in-coupling mode is on mirror m_1. The telescope is arranged with the shorter focal length lens f_1 and larger lens f_2 magnifying the mode and producing a large mode interaction region in length L_3. There is a focus between the telescope lenses. An intracavity Pockels cell is shown within L_1.

making a planar mirror at the large mode section (L_3) the appropriate choice. In the small mode section a planar mirror was selected due to the wide range of coatings available in stock planar mirrors. The coating of this mirror must be chosen to optimise cavity impedance matching and a planar mirror gave us the most choice. A curved mirror at the end of this section would reduce the length of L_1 but in this system, L_1 is already as short as it could be whilst still accommodating the Pockels cell.

With the mirrors chosen the next steps are the focal lengths of the telescope lenses. This is constrained by the available length for the cavity. In this system we had a total length of less than 1 m including beam delivery optics, so the cavity is practically limited to 0.7 m. Of this length the large mode collimated section must be longer than the vacuum system $L_3 > 0.39$ m. The remaining 0.3 m is divided between the compact mode section L_1 and the telescope L_2. Once dimensions for the Pockels cell were considered L_1 and L_2 end up needing to be similar splitting the remaining 0.3 m in two.

A telescope is characterised by its magnification. The precise relationship between the magnification and resulting mode size is complex, but the large mode diameter is of the same order as the telescope magnification multiplied by the confocal diameter (the diameter of a confocal cavity of the same length). For the 0.69 m cavity discussed here with a target mode diameter of a few millimetres, this suggests a magnification of around ×10. This estimate is used as a starting point for simulations to find the optimum magnification and resulting mode diameters.

Considering the target magnification, available space, and available lenses we select $f_2 = 150$ mm and $f_1 \simeq 12$ mm, producing a Keplerian telescope with a magnification of 12.5. Short focal length lenses have high curvature surfaces and are difficult to produce accurately, so where space permits avoiding short focal length lenses is advantageous.

With all of the optics selected, the final challenge is to select the exact optic spacings L_1, L_2, and L_3 to produce a stable cavity with a large mode. This is a three dimensional parameter space making optimisation difficult. Fortunately, we can fix L_3 to the value enclosing the minimum value vacuum system, and noting that due to the large mode and near collimation in this section, the cavity mode is insensitive to this spacing. With the search reduced to two dimensions, we use as a starting point $L_2 = f_1 + f_2$ corresponding to a telescope focused at infinity and set L_1 to occupy the remaining space, 0.1 m. Within the telescope we expect the beam to come to a tight focus so we expect cavity parameters to vary most strongly with L_2, weakly with L_1, and almost independently of L_3.

We use the simulation package presented in chapter 4.6 to calculate ABCD matricies for 10^6 cavities with varying L_1 and L_2. We use these matricies to calculate the large mode waist of the cavity which we represent with the surface plot shown in figure 5.5. Slices at constant L_1 are shown in the lower figure. Initial searches of the parameter space covered larger regions at lower resolution, to locate the region containing stable cavity modes. Once the region was located, higher resolution scans could be conducted. If the resulting modes are smaller than desired, the magnification of the telescope should be increased and then the process repeated.

Outside the surface, stable cavity modes do not exist. At the edges of the surface the radius diverges as the cavity reaches the limits of stability ($m \to \pm 1$), see section 5.4.1. As we predicted, the performance of the cavity is far more sensitive to L_2 than L_1, but not intractably so. Slices through the surface of constant L_1 illustrate that at the centre of the surface the beam waist is remarkably insensitive to perturbations in L_2. This should be contrasted with the asymptotic behaviour at the edges of the surface which is the same dependence encountered by two mirror cavities at the edge of stability. At the very centre of the surface, the design is first order insensitive to perturbations in L_2 but unfortunately this solution is degenerate to higher order modes. Surface plots provide a powerful and flexible way to visualise the parameter space for optical cavities.

5.4 Higher Order Modes

As we discussed in chapter 4.5.1 the ability of a cavity to suppress higher order modes is controlled by the round trip Gouy Phase, shown in equation 4.32. Where the round trip Gouy phase is an integer factor of π higher order mode degeneracy will occur. For the fundamental mode ($p, q = 0$) the Gouy phase takes the simplified expression:

$$\phi = \operatorname{sgn}(B) \cos^{-1}(m) \tag{5.4}$$

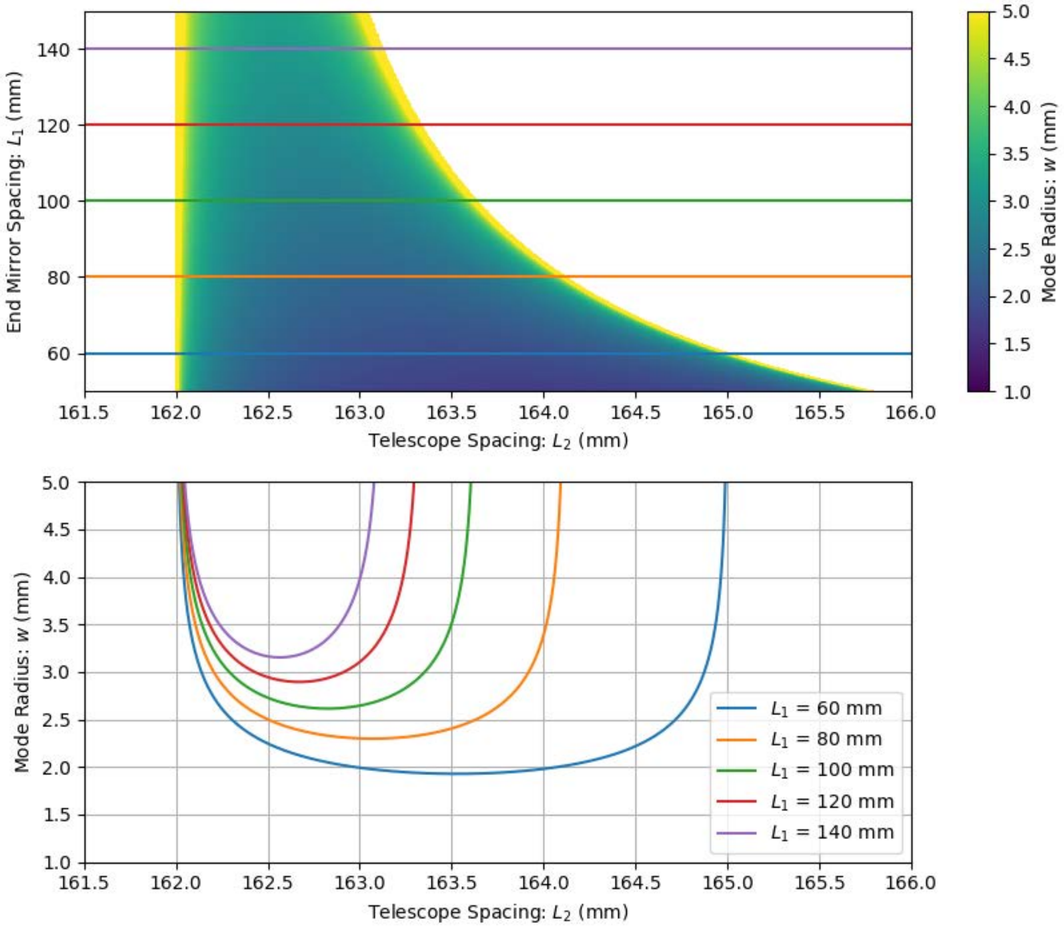

Figure 5.5: The beam radius at mirror-2 is shown as a surface against the length L_1 and the telescope spacing L_2 with a number of slices shown below. The large diameter of the section and correspondingly long Rayleigh range make the mode diameter insensitive to L_3. The slices illustrate that around a central set of values the large beam radius is insensitive to perturbations in length L_2.

5.4.1 Gouy Phase Control

The Gouy phase is controlled through the cavity half trace m which can be tuned by adjusting the length of the telescope L_2. To observe this behaviour we generate another surface plot of L_1 and L_2 with the surface representing the round trip Gouy phase, see figure 5.6.

Adjusting the lens spacing L_2 in the telescope varies the half trace m and as a result allows the Gouy phase to be tuned freely over its full range. The edges of the surface represent the edges of stability $m \to \pm 1$, and represent degenerate cavities with large modes and strong sensitivity to L_2 which should be avoided. Cavity parameters which result in degeneracy with the first five higher order modes are shown as contours in figure 5.6 (three contours and the two boundaries of the surface). The Gouy phase can be tuned to a

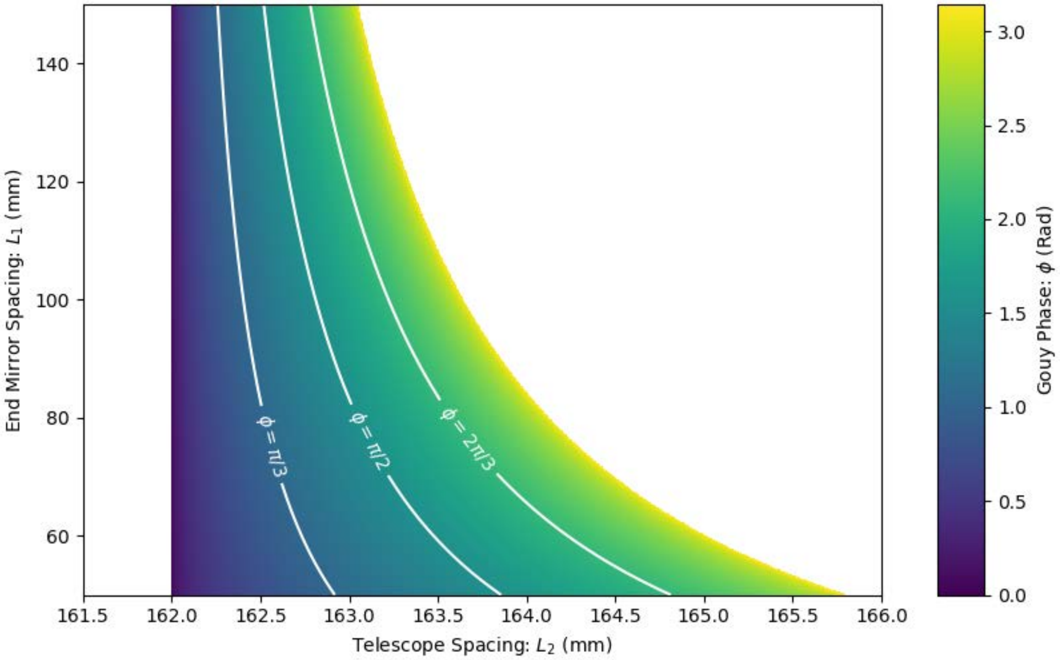

Figure 5.6: The round trip Gouy phase of the cavity is shown as a surface plot against length L_1 and the telescope spacing L_2. The edges of the surface correspond to the limits of stability $m = \pm 1$. Five contours corresponding to Gouy Phase values of $\phi = 0$, $\pi/3$, $\pi/2$, $2\pi/3$, π are shown. These solutions represent cavities degenerate to the first few higher order modes.

value reducing higher order mode degeneracy, whilst maintaining only moderate sensitivity to perturbations in length.

5.5 Parameter Selection

We combine the information on the previous surface plots on figure 5.7 by including the degenerate Gouy phase contours on the radius surface. We select cavity parameters which minimise sensitivity to perturbations in L_2 whilst avoiding degenerate values of Gouy phase and achieving the target mode diameter. These are $L_1 = 93$ mm, $L_2 = 162.6$ mm and the location of this cavity in the parameter space is indicated on the figure. This design produces a large diameter beam waist of $2w = 5.16$ mm. The telescope increases the effective length $|B|$, in the magnified section, from the physical round trip length of 1.38 m to 25.5 m making this large beam possible in such a compact geometry. With these parameters, beam radius fluctuations of 1% require the L_2 to change by more than 100 μm. This level of stability is readily achievable with standard optomechanics. The round trip Gouy phase for this design is $\phi = 1.25$ avoiding the degenerate values of $\pi/2$ and $\pi/3$ whilst minimising sensitivity to perturbations in the length of the telescope. A more detailed analysis of the relative contributions of higher order modes is required to fully optimise the choice of Gouy phase.

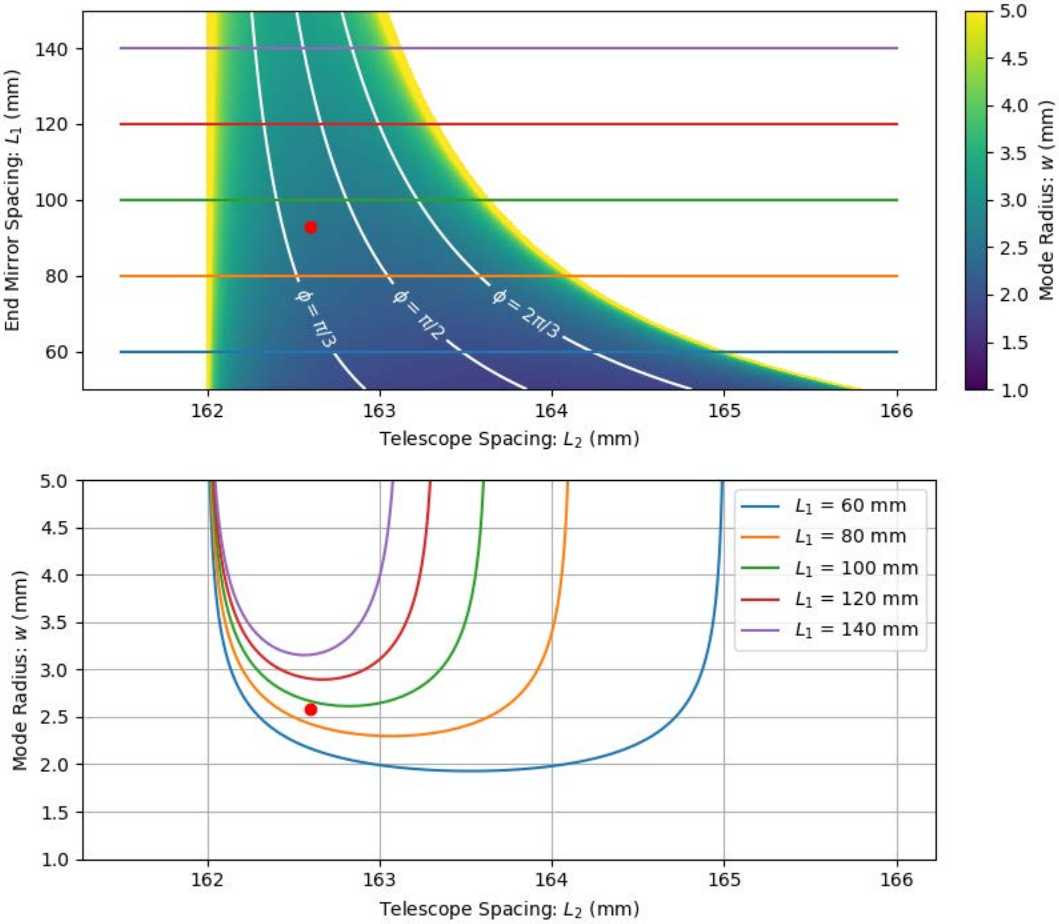

Figure 5.7: The mode radius on mirror-2 is shown for different values of L_1 and L_2, and slices for fixed values of L_1 are shown below. Contours representing degenerate values of Gouy Phase are shown in white, which should be avoided to allow higher order mode suppression. The cavity described in this work is indicated by a red spot on both plots. The plot was generated by calculating the ABCD matrices for 10^6 different cavities and was used to select optimal cavity parameters.

5.5.1 Adjustable Length

The cavity length and *FSR* can be coarsely adjusted without any significant impact on the stability properties by simply moving mirror m_2. The near collimated large mode section (L_3) has a correspondingly large Rayleigh range (26 m) allowing ∼ 10 cm changes without any significant effect. This is useful in schemes where the FSR must be precisely controlled to match atomic transitions, such as those used in [44] [49]. In our scheme, precise FSR control is not required, for reasons discussed in 5.2.

5.6 Conclusion

We present a novel optical cavity geometry for atom interferometry combining a large mode diameter with tunable Gouy phase, power enhancement, and Doppler compensation. An intracavity telescope allows a large beam diameter to be achieved in a physically short cavity, whilst avoiding the extreme dimensional tolerances encountered at the edges of geometric stability. Adjustments to the telescope spacing control the Gouy phase, suppressing higher order spatial modes, and improving wavefront flatness. An intracavity Pockels cell, introduces voltage controlled birefringence, allowing the resonant frequencies of the cavity's two orthogonal polarisation modes to be independently controlled. Aligning the Raman beams with the polarisation modes maintains cavity resonance even as the Raman frequencies are chirped. This overcomes the Doppler limit, the central limitation of current cavity systems, and allows a dramatic increase in cavity length and finesse. Maintaining precise cavity resonance also reduces our sensitivity to vibrations and laser frequency noise compared to existing work.

CHAPTER 6

CAVITY DEMONSTRATION

In the following chapter, we will examine the experimental apparatus used to construct the 1 m scale, large mode, Doppler compensated cavity described in chapter 5 [2]. We present characterisation data from the cavity including successful operation of the Pockels cell, finesse and power enhancement calculations and measurement of the intracavity beam diameter. The full alignment procedure is provided in appendix A.

6.1 Cavity Optomechanics

The cavity is 0.69 m long, and contains mirrors, lenses, a Pockels cell, and must be compatible with a vacuum system. The system must also provide beam delivery optics and photodiodes for monitoring the cavity. The entire system needs to be stable in a vertical configuration and will ideally remain aligned moving from a horizontal to vertical orientation. We used a 1 m long aluminium profile rail for this purpose[2]. It could be mounted horizontally or vertically, optics can be positioned along the length, and it is compatible with a range of translation stages for precise positioning of the critical optics. For an initial test, a laser beam was delivered parallel to the rail and the position was then measured with a CCD mounted to the rail on a sliding carriage. In the horizontal geometry the location deviated by $< 100\ \mu$m along its 1 m length, and changing the orientation from horizontal to vertical changed the position of the spot by $< 40\ \mu$m, again over the full length of the board. This includes any contribution from the CCD mount sagging under its own weight in this orientation.

The mirrors were mounted in kinematic mounts with two adjusters[3], the long focal length lens f_2 was mounted in a glue-in fixed mount[4] and the short focal length lens was mounted in fixed lens mount with a

---

[2] Owis: S 65-4-1000

[3] Thorlabs: Polaris-K1S4

[4] Thorlabs: POLARIS-L1G

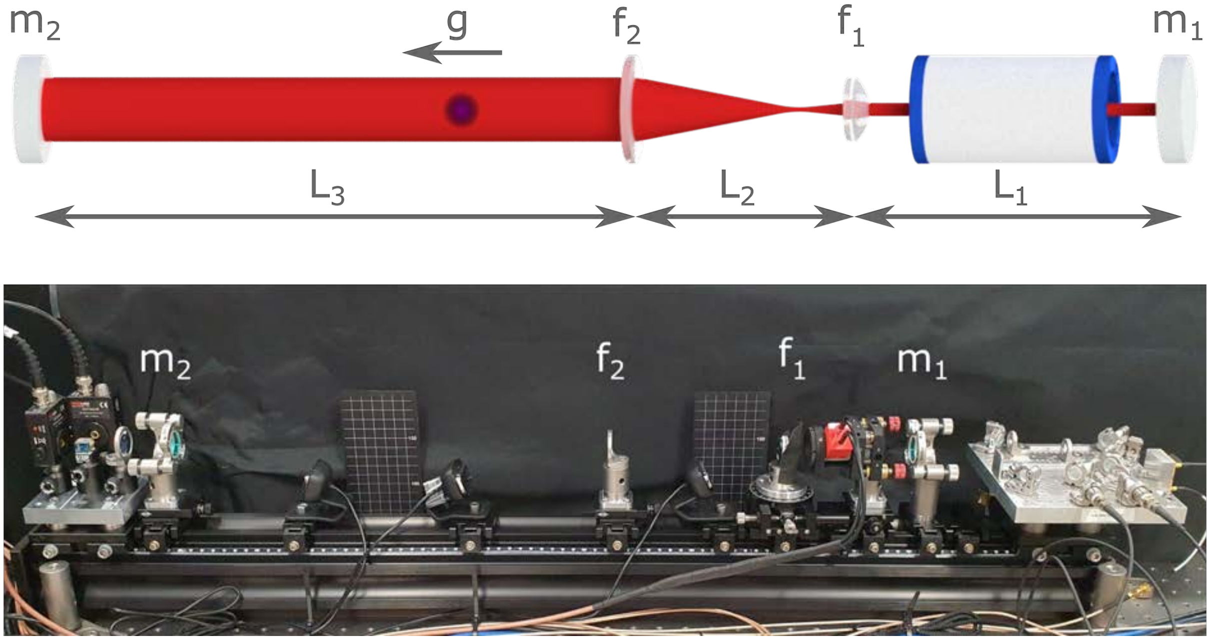

Figure 6.1: A schematic and photograph of the cavity in a horizontal orientation: Light is delivered to the cavity from a custom breadboard on the far right. This comes to a focus on the planar input mirror m_1. The Pockels cell is within L_1. The two cavity lenses have focal lengths $f_1 = 12$ mm and $f_2 = 150$ mm yielding 12.5× magnification. The large mode interaction region is produced in L_3. The atoms (purple) experience Doppler shifted laser frequencies when moving with respect to the cavity (when the cavity is in its vertical orientation).

retaining ring [1]. The Pockels cell was mounted in a 3 axis mount providing tip, tilt and rotation [2] although the tip and tilt axes are not centred on the middle of the crystal meaning that rotation, tip, and tilt were coupled. These mounts were all fixed on 1" posts to bring them up to the correct beam height. The 1" diameter increases stiffness and reduces the sag of the post when the system is mounted in its vertical orientation. These posts were mounted to rail carriages allowing them to be positioned at will. The axial locations of mirror-1 and lens-2, the transverse position of the Pockels cell and the rotation of lens-1 all required precise adjustment. This was achieved with compact translation stages also mounted on the rail, see figure 6.1.

Light is delivered to the cavity from a a custom beam delivery board, also mounted to the rail with 1" posts and a carriage. This board takes fibre inputs from the laser system, combines the two beams, and provides a telescope to match the cavity mode. It further includes beam samplers and a photodiode for cavity stabilisation. This was all achieved in a compact footprint of 140 mm × 140 mm; see figure 6.2. It

---

[1] Thorlabs: LMR15/M

[2] ESKMA optics: PM1

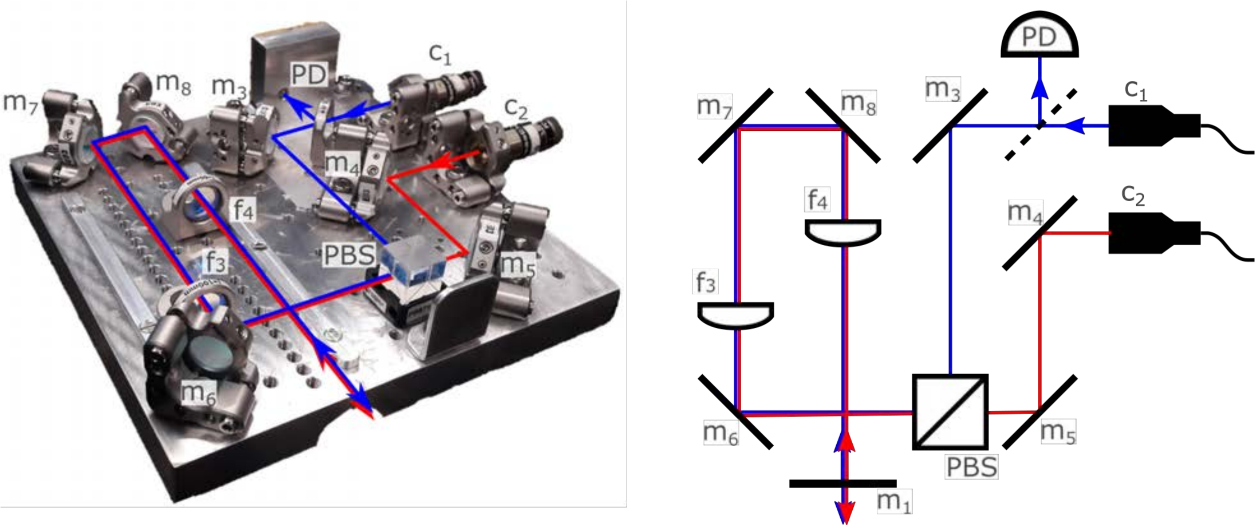

Figure 6.2: Light is delivered to the cavity from this custom beam delivery breadboard. It combines the two input polarisations on a PBS. Lenses f_3 and f_4 form a telescope to correct the beam size and bring them to a focus on cavity mirror m_1. Mirrors m_6 and m_8 are used to fine tune the spatial overlap with the cavity mode. The photodiode and beam sampler are used for laser frequency stabilisation.

has been designed to deliver the output beam to the centre of the rail and the entire board can be translated along the length.

Alignment of a multi-element cavity is challenging due to the large number of degrees of freedom. A full alignment procedure is provided in appendix A.

6.2 Cavity Performance

6.2.1 Frequency Response

We scanned the frequency of the input laser allowing measurement of the cavity transmission and reflection spectra; shown in figure 6.3. The peaks in transmission spectrum and dips in the reflection spectrum occur when the resonance condition is met. The depth of the dip in the reflection provides a measure of mode matching efficiency. In this case we observe a reflected signal $< 3\%$ but due to uncertainties in the background level claim 90% as a conservative estimate. This confirms that beam size and spatial overlap have been successfully optimised.

The spacing between the peaks also provides a coarse measurement of the free spectral range as 217 MHz, and we find the cavity finesse as a fit parameter $\mathcal{F} = 64$. For an improved measurement of the free spectral range, we used an electo-optic modulator to add further frequency components to the input laser. We tune this

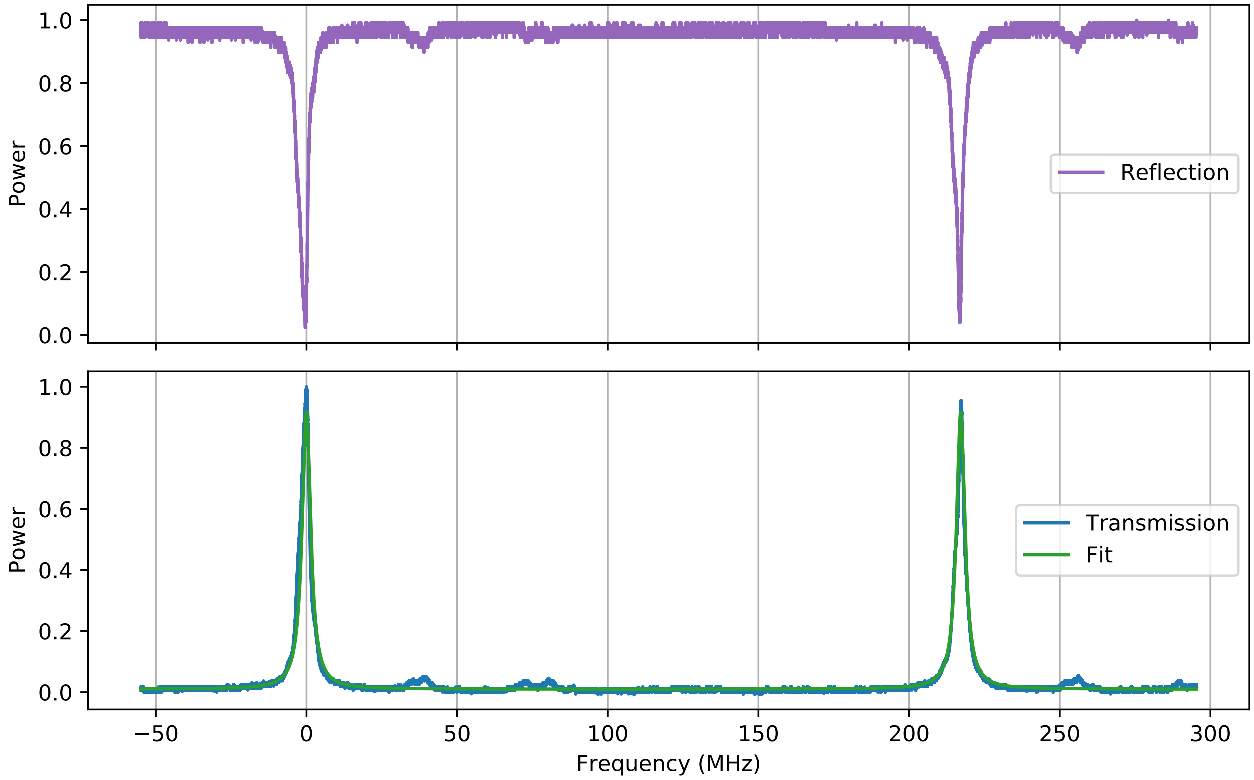

Figure 6.3: Cavity transmission and reflection spectra without the Pockels cell. The transmission spectrum is fitted and has a finesse of $\mathcal{F} = 64$. The features in the spectrum between 40 and 100 MHz are higher order modes. The $< 3\%$ reflection on resonance suggests excellent matching to the fundamental mode.

modulation frequency until multiple longitudinal modes are resonant simultaneously. This is only possible if the modulation frequency is an integer multiple of the free spectral range. We found $\nu_{fsr} = 217232.5 \pm 6.9$ kHz, corresponding to round trip optical path length of 1.380053 m $\pm$ 44μm. By employing a large modulation frequency (6.7 GHz) we were able to reduce measurement uncertainty by dividing uncertainties in the resonant frequencies by 31 free spectral ranges.

6.2.2 Intracavity Beam Diameter

We removed mirror-1 to profile the cavity input beam at a location coincident with this mirror. The target was to produce a beam waist of the theoretically determined size coincident with the location of this mirror; for details of the alignment procedure see appendix A. With this mirror removed we were able to profile the beam along the majority of the length of the cavity, see figure 6.4. The gaps in data occur where there were conflicts between the beam profiler and intracavity optics.

Whilst this beam profile is not a true profile of the cavity mode, due to the excellent mode matching

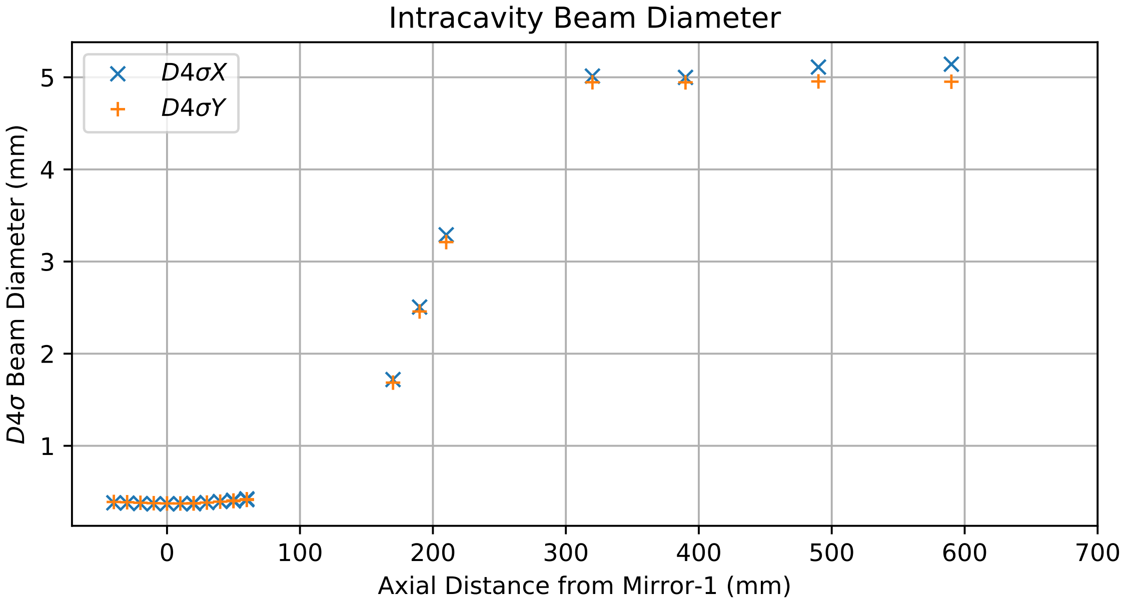

Figure 6.4: The $D4\sigma$ beam diameter as a function of axial position is measured with a CCD. The cavity input mirror was removed to enable this measurement.

observed with the mirror in place, and the fact the mirror is planar, the differences between this profile and the true cavity mode are expected to be small. The large mode beam diameter was measured to be 5.04 mm.

6.3 Pockels Cell

As we found in chapter 5.2, an intracavity Pockels cell allows for compensation of the Doppler effect. The Pockels cell induces a voltage controlled birefringence, and by applying a correctly tuned voltage ramp, the cavity modes can match the chirping frequency of the orthogonally polarised Raman beams. Figure 6.5 shows the effect of varying the Pockels cell voltage on the transmission function of the cavity, here illuminated with both polarisations.

In the first frame a voltage of −160 V was applied to compensate for residual birefringence in the crystal, and the resonant frequency for the two polarisations is degenerate. In the following frames the voltage is increased, lifting the initial degeneracy between the two polarisations causing their respective transmission peaks to separate. In the final frame the frequency difference between the two peaks is over 110 MHz, sufficient to compensate for 4.5 s of free-fall in rubidium-87, far exceeding the physical size of the cavity. Details for setting the ramp rate for a given cavity and atomic species can be found in chapter 5.2. The intracavity Pockels cell has behaved as predicted and enables Doppler compensation in cavity enhanced atom

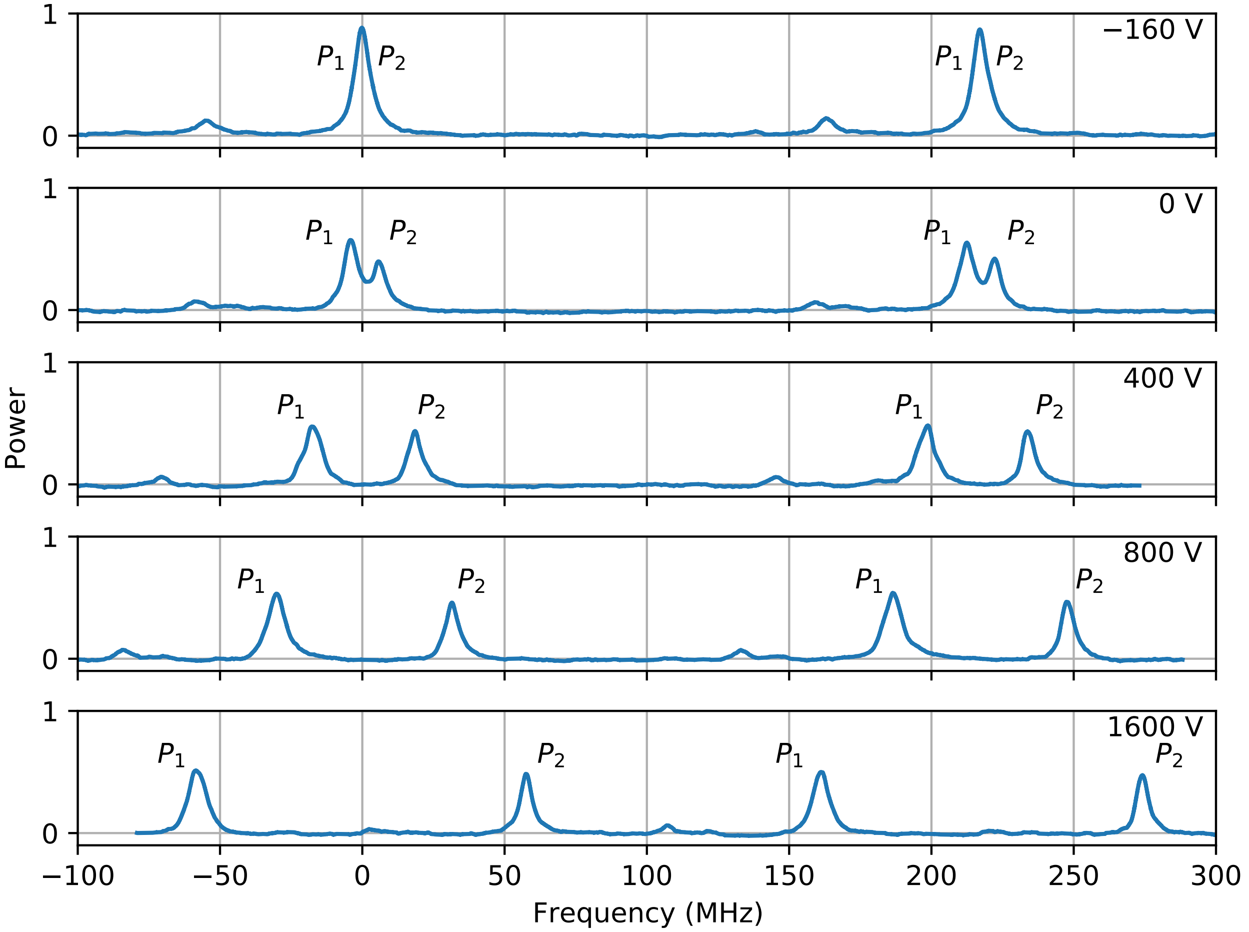

Figure 6.5: Increasing the voltage applied to the Pockels cell induces birefringence into the cavity. The orthogonally polarised cavity modes are separated in frequency, from the degenerate value at -160 V to 114 MHz at 1600 V applied. The initial offset compensates for residual birefringence in the crystal. Ramping the voltage at 390 $\mathrm{V\,s^{-1}}$ compensates for the 25.1 $\mathrm{MHz\,s^{-1}}$ Doppler shift in rubidium-87.

interferometry for the first time.

In the spectra provided in figure 6.5 the Pockels cell is well aligned with the cavity mode. This is shown by the lack of other transmission peaks at other frequencies and relatively constant amplitude between different voltages. In the BBO crystal[1] used in this system, the indices of refraction are $n_e = 1.55$ and $n_o = 1.66$ so a small misalignment produces significant path length differences, and coupling to higher order modes. Details of the alignment procedure are provided in appendix A.8.

---

[1] β-barium borate Pockels cell, Gooch and Housego, Light Gate 3, AR coated at 780nm

6.4 Power Enhancement

Resonant power enhancement is one of the key benefits achieved with this optical cavity. This proof of principle system demonstrated a power enhancement of over five times with a finesse of $\mathcal{F} = 35$, using standard components. Whilst modest for a cavity, this is a dramatic improvement in the context of atom interferometry.

Table 6.4 shows the specified loss of all the optics in the cavity and reaches a total round trip loss of 10.3%, including $\delta_1 = 4.3\%$ from the input mirror. This data comes from manufacturer specifications or tests and does not include any losses due to misalignment, or scatter from dust on the surface. It also neglects transmissive losses from absorption in the glass for most of the optics. As we found in chapter 4.2, we maximise the resonant power enhancement in this system by impedance matching; transmission through the input mirror is equal to round trip loss. This would suggest that a larger value for $\delta_1 \simeq 6\%$ would increase the enhancement. The input mirror had a target specification of $\delta_1 = 5\%$ which is close to impedance matching the specified round trip losses. However, test data from CVI demonstrated that the actual transmission of this mirror was lower than this.

Name:	Manufacturer	Part number	Loss per Pass (%)	Passes per RT	RT Loss
Mirror-1	CVI	PR1-800-95-1025	4.269%	1	4.27%
Pockels Cell	G+H	LightGate 3	< 1.5	2	3.00%
Lens-1 eyepiece	Thorlabs	AL1512-B	< 1	2	2.00%
Lens-2 objective	Thorlabs	LA1433-780	< 0.5	2	1.00%
Mirror-2	CVI	TLM1-800-0-1025	0.048	1	0.05%
				Total:	10.28%

The finesse calculated from a fit of figure 6.5 is $\mathcal{F} = 35$ which with the input mirror transmission $\delta_1 = 4.3\%$ suggest a round trip loss of $\delta_c = 18\%$ and gives a power enhancement of 5.3 times. This value is not strongly dependent on any the parameters and is a reasonable estimate of resonant enhancement. This increased total loss motivates the use of a more transmissive input mirror, but even with perfect impedance matching, the power enhancement only increases to 7.3 times.

With the Pockels cell removed from the cavity, a higher finesse of $\mathcal{F} = 64$ was measured, see figure 6.3. The same analysis indicates a round trip loss of $\delta_c = 10\%$ and power enhancement of 17.8 times. This implies a single pass loss through the Pockels cell of 4% which is significantly above the specified 1.5%. This naive comparison neglects misalignment effects through the Pockels cell; qualitative observations during alignment suggest that these are likely to be significant. The large number of transmissive components has limited the maximum attainable enhancement in this cavity, however the number of surfaces and the resulting loss can be dramatically reduced with design improvements; see chapter 7.1.

6.5 Laser System

The laser system delivers 400 mW of light at 780 nm in two frequency components separated by the hyperfine frequency $\nu_{HFS} = 6.8$ GHz, as required for Raman atom interferometry. This is achieved using a telecoms laser at 1560 nm, frequency doubled to 780 nm; a schematic of the system is shown in figure 6.6. We start with a fibre laser producing 40 mW at 1560 nm[1]. The output from the seed is split into two arms for the two Raman frequencies, both of which are phase modulated by fibre EOMs[2]. The first arm is weakly modulated at 20 MHz to generate sidebands for frequency stabilisation. The second arm is modulated, at a frequency of 6.35 GHz and a modulation depth of $\simeq 0.9$ radians. This generates the second frequency component for Raman transitions, at a modulation depth that maximises the amplitude of the first side band after frequency doubling. The output power in this second arm is distributed between upper and lower sidebands with a maximum of 34% at the target frequency. In both arms the modulated light is amplified by an EDFA[3] producing 1 W at 1560 nm. The high power beams are frequency doubled in a quasi-phase matched Lithium-Niobate waveguide[4]. This produces $\simeq$ 400 mW of 780nm in each arm. Both arms are switched by fibre coupled AOMs[5], before passing through a fibre coupled optical isolator[6]. The isolators are connected to 2 m patch cords[7] to deliver 200 mW of power from each arm to the collimators on the beam delivery board.

6.5.1 Control System

The system is controlled by an ARTIQ based control system running on Sinara Hardware. An externally clocked[8] FPGA[9] provides 1 ns accuracy timing signals to frequency synthesizers[10], TTL I/O cards[11], DAC cards[12], and A-to-D converters [13]

---

[1] NKT: Koheras BASIK E15

[2] Electro-Optic Modulator: MPZ-LN-10 from iXblue

[3] NKT: 1W EDFA (Erbium-doped fiber amplifier)

[4] NTT Electronics: WH-0780

[5] Gooch and Housego: T-M150-0.5C2W-3-F2P, 150 MHz, 50% efficiency

[6] Oz Optics: FOI-11-11-780-5/125-P-50-3A3A-1-1-35-HP1, 35dB isolation, PM

[7] Schäfter + Kirchhoff: PMC-780-5.1-NA012-3-APC-200-P

[8] Nexyn: NXPLOS-I-0700, Phase Locked DRO 7GHz with Internal OXCO

[9] Sinara: 1123 Processor, Kasli

[10] Sinara: Urukul, AD9910 DDS (Direct Digital Synthesizer), 4 Channel, 400MHz

[11] Sinara: 2128 SMA TTL (Transistor-Transitor Logic)

[12] Sinara: 5432 DAC(digital-to-analogue converter), Zotino

[13] Sinara: 5108 Sampler (analogue to digital converter)

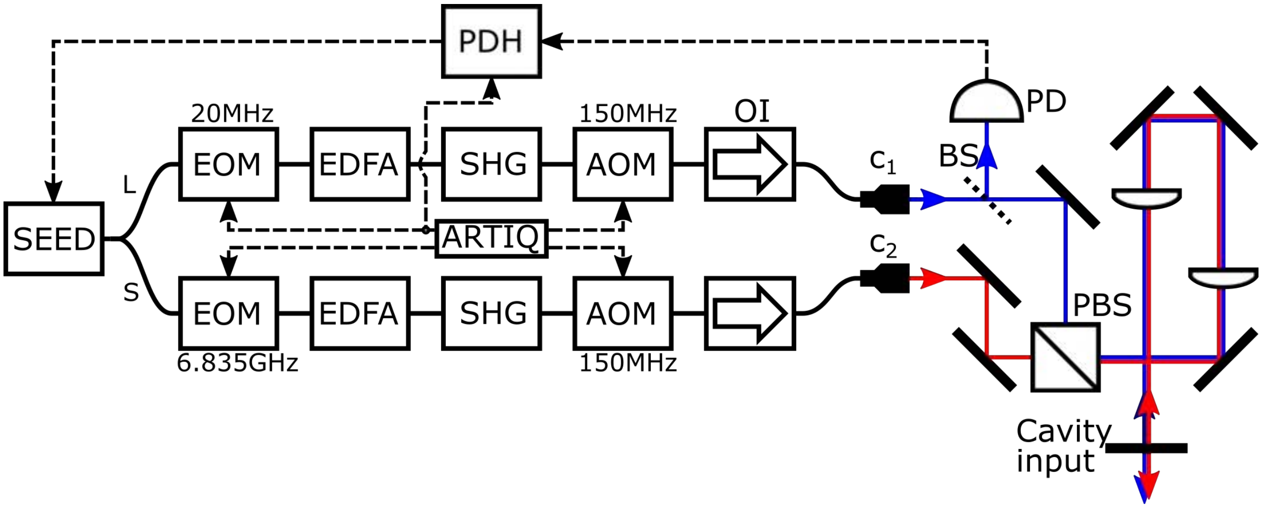

Figure 6.6: Light at 780 nm is produced by amplifying and frequency doubling a 1560 nm seed. Light reflected from the cavity in the polarisation shown in blue is reflected by a 5 % beam-sampler onto a bespoke photodiode for locking using the Pound-Drever-Hall technique.

These DDS cards generate the 150 MHz signals for the AOMs, the 20 MHz signal for the frequency stabilisation and local oscillator, and produce a signal at 164 MHz to generate the 6.835 GHz hyperfine frequency. This 164 MHz is mixed with a 7 GHz output from the clock, with a single-sideband mixer [1] achieving 32.7 dB carrier suppression, and further suppression of higher harmonics. These signals are amplified where necessary before delivery to their respective components. The DDS cards allow agile amplitude and phase control and share a common external frequency reference.

The DAC card was used to generate the voltage signals to control the Pockels cell. With an output range of only ±10 V a high voltage amplifier was required to step this up to the 3.5 kV half-wave voltage of the Pockels cell. The low slew rate required in this system, (Doppler compensation only requires 400 V/s), allowed the use of a relatively inexpensive amplifier[2] .

6.5.2 Frequency Stabilisation

We stabilised the laser to the cavity using a Pound-Drever-Hall lock [92]. In this scheme the laser is modulated on the input to the cavity. The reflected beam is picked off and measured on a photodiode. A mixer is used to compare the photodiode signal to the local oscillator at the modulation frequency. After low pass filtering, this error signal provides a measure of both the size and crucially direction of the deviation from resonance. We supply this error signal as the input to a PID loop and supply the output directly to the seed laser piezo

---

[1] Polyphase Microwave: SSB4080A

[2] Advanced Energy: Ultravolt 4HVA24-BP1-F-25PPM-BNC-10KV, Bipolar 4kV Voltage Amplifier

modulation.

As we inject light into both cavity polarisations, the standard technique to separate the input and reflected beams using a polarising beamsplitter and a $\lambda/4$ (quarter-wave plate) was not possible. Instead we insert a 5% beam-sampler into the modulated polarisation beam path, and stabilise the laser frequency on the sampled fraction of the light reflected from the cavity. The majority of the light passes through the pick-off and back into the fibre, making the additional optical isolation essential.

This loop is run continuously at low optical power and a large detuning to maintain laser lock during the sequence whilst minimising spontaneous emission. The laser is pulsed to full power for the Raman pulses. To minimise complexity in this system, the cavity has been left free running and the laser is stabilised to this drifting reference. This has the undesirable effect of tracking length changes in the cavity as shifts in the single photon detuning Δ, but due to the large detuning, these effects are expected to be small enough not to ruin this proof of principle experiment. For improved performance the cavity can be independently stabilised with a piezo through a more complex locking scheme such as that presented by Hamilton [44]. Adding a beam sampler and photodiode to the second polarisation would allow the Pockels cell voltage to be actively stabilised rather than the existing open-loop configuration.

6.6 Conclusion

We demonstrate a cavity for atom interferometer enhancement that for the first time combines a large mode diameter with the capability to provide Doppler compensation, reduction of wavefront aberration through spatial mode filtering and power enhancement. This overcomes the two key barriers preventing high performance use of cavity enhanced atom interferometry, while realising the two primary benefits. This is achieved while also being robust to changes in cavity length, and avoiding the extreme dimensional tolerances encountered at the edges of geometric stability. In chapter 7 we will propose some refinements to this cavity design to further improve performance.

CHAPTER 7

ADVANCED GEOMETRIES

The cavity design developed and implemented in chapters 5 & 6 solves the principle issues facing cavity enhanced atom interferometry delivering large modes, spatial mode filtering, and Doppler compensation simultaneously. Where the implementation fell short, however was with the high round trip loss, resulting in low finesse, relatively low power enhancement, and a reduction in achievable spatial mode filtering. Further to this, the standing wave geometry of this cavity makes it inappropriate for high bandwidth systems or those operating in microgravity. In this chapter I will propose a new cavity design to reduce losses, remove spectator beams, and lift the initial frequency degeneracy, whilst retaining the key properties already demonstrated. This magnified bow tie geometry is presented with a set of parameters for a table top implementation, along with the design process to enable the reader to design a cavity for their specific system.

7.1 Power Enhancement

The large number of transmissive optics limited the maximum attainable enhancement in the cavity described in chapter 6. On each round trip, the mode encounters 26 optical surfaces and 12 transmissions, increasing to 34 and 16 respectively with the addition of a vacuum chamber. This comprises two double passed lenses (eight surfaces and four transmissions); a double passed Pockels cell containing two crystals and two windows for hermetic shielding (16 surfaces and eight transmissions); and two mirrors. The vacuum chamber will add two double passed windows per round trip adding eight surfaces and four transmissions.

7.1.1 Windows

Moving the entire cavity into vacuum provides a dramatic reduction in round trip loss. The windows on the vacuum chamber and the windows providing hermetic shielding on the Pockels cell can all be removed from the cavity. This eliminates a total of 16 optical surfaces and eight transmissions per round trip.

7.1.2 Lenses and Mirrors

After the windows have been removed, the dominant transmissive optics are the two lenses, introducing four transmission and eight surfaces per round trip. The lenses used in chapter 6 had broad band AR coatings with reflectances of $< 0.5\%$ per surface. Custom AR coatings, should allow the loss per surface to be reduced to $< 0.1\%$ but transmissive losses cannot be totally eliminated.

For more dramatic improvements the lenses should be replaced with curved mirrors, see figure 7.1. The high reflectance mirror used in the previous chapter, had a reflectance of 99.952% resulting in 0.05% loss per reflection which is more than an order of magnitude improvement over the lenses. The contribution to round trip loss from even this relatively standard mirror is negligible compared to the remaining loss from the Pockels cell. By selecting mirrors with equal focal lengths to the lenses they replace ($R = 2f$), large mode diameters and tunable Gouy phase can still be achieved.

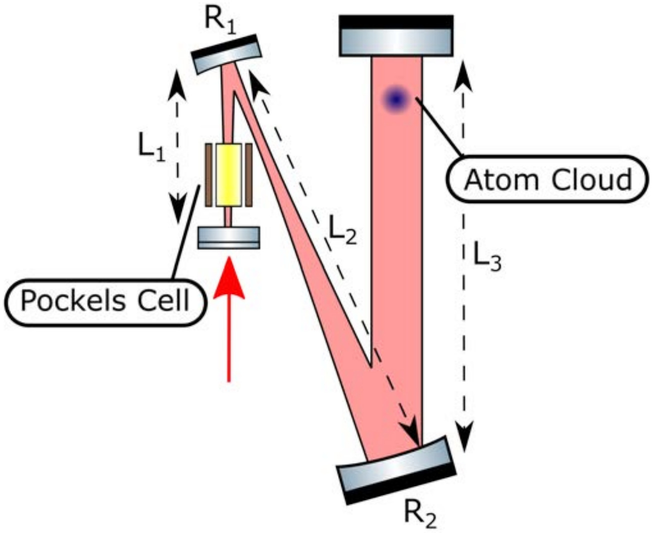

Figure 7.1: This cavity design replaces the lenses (f_1 and f_2) with curved mirrors(R_1 and R_2), achieving the same beam size, Doppler compensation, and Gouy phase tuning as in the linear geometry. This replacement allows a significant reduction in intracavity loss. [84]

7.2 Cavity Geometries

7.2.1 Standing Wave

The cavities discussed so far have all been standing wave geometries. In a standing wave cavity, the forward and reverse directions of propagation overlap and produce a standing wave within the cavity. Circulating light must necessarily pass through every optical element and the atoms within the interferometry twice per round trip. In one propagation direction, light should not contribute to the interferometer and efforts must be made to ensure it does not do so; this unwanted light is referred to as a spectator beam. Initial free-fall times of $\simeq 10$ ms are commonly used before the start of the interferometry sequence, to allow gravitational acceleration induced Doppler shifts to lift the frequency degeneracy between the downward and upward going beams. Even with these accommodations, spectator beams still produce phase shifts in an atom interferometer which must be characterised and compensated [47, 93].

For systems operating at high bandwidth, the sequences are too short for the Doppler shift to lift the degeneracy, so retroreflection cannot be used [80]. The same is true in microgravity where the relative acceleration between the atoms and the laser beams is negligible, and launching the atoms to induce a relative velocity will severely reduce the available interrogation time, in turn, reducing sensitivity.

7.2.2 Travelling Wave

A travelling wave (ring) cavity overcomes these limitations and will allow cavity enhancement of the widest possible range of systems. The cavity in figure 7.1 can be converted to a ring cavity with the same mode parameters by removing the planar end mirrors and unfolding the cavity; see figure 7.2. This design has the same beam diameter, and round trip Gouy phase. It removes the spectator retroreflected beams and their resulting light shifts, and further eliminates the degeneracy between the upward and downward going beams at short free fall times.

This in vacuum bow tie geometry eliminates the two planar mirrors and moves the Pockels cell into a single pass configuration, saving an additional six surfaces and two transmissions, leaving only 8 optical surfaces and 2 transmissions per round trip. Specifically four mirror reflections, and a double crystal Pockels cell contributing four end faces and two crystal transmissions per round trip. With high quality mirrors and AR-coatings on these surfaces, round trip losses in the $< 1\%$ range should be possible. This enables high finesse cavity atom interferometry and will dramatically extend the available power enhancement and degree of spatial mode filtering that can be achieved.

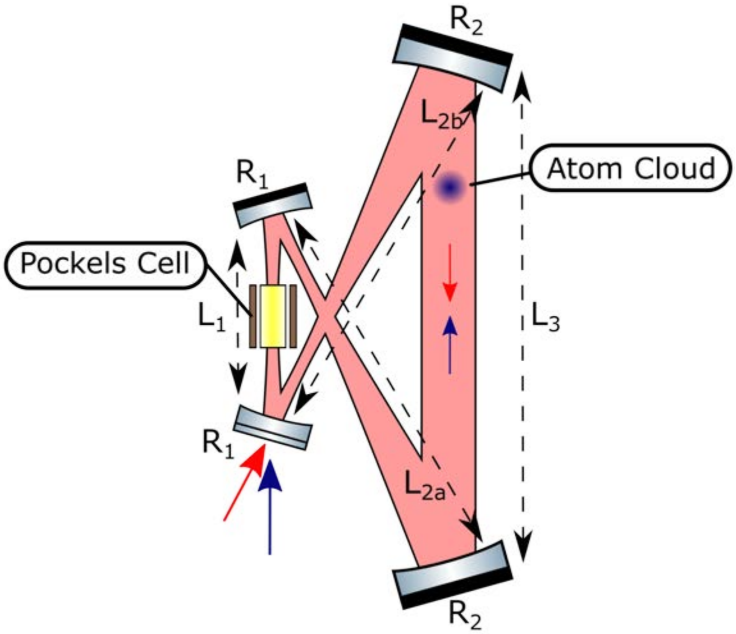

Figure 7.2: This magnified bow tie geometry unfolds the standing wave design in figure 7.1 converting the cavity into a travelling wave geometry. This prevents spectator beams from reflecting through the atom cloud preventing the associated light shifts and spontaneous emission. It further prevents the unnecessary double pass through the Pockels cell, reducing the number of optical surfaces per round trip.

Simply unfolding a magnified linear cavity fails to fully embrace the flexibility that the new geometry has provided. As the telescopes and the interaction region are no longer collinear, longer telescopes can be used without increasing the overall size of the cavity. This allows higher magnifications and larger mode diameters, or reduced mirror curvatures at fixed mode diameter. This is advantageous as mirrors with short radii of curvature are difficult to manufacture and have more stringent tolerances on alignment.

7.3 Magnified Bow Tie

The design procedure for a magnified bow tie cavity is similar to that described in chapter 5. The large mode diameter in section L_3 makes the cavity properties largely independent of this length. It is selected to accommodate the required interaction region which for the example we present here is chosen to be $L_3 = 0.9$ m.

The next feature to design is the telescope. Geometric considerations require the use of telescopes longer than half the length of the interaction arm, that is $L_2 > L_3/2$. The high telescope magnification required to generate a large diameter beam in L_3, implies that the length of the telescope is determined almost entirely by the focal length of the mirrors R_2. The focal length of mirrors R_1 should then be chosen to achieve the target magnification and large waist size. In this case we select $R_2 = 1$ m and then $R_1 = 24$ mm, producing a magnification of 41 times and a trial separation $L_2 = 512$ mm.

The optimum length of the telescope L_2 is determined graphically from figure 7.3 by ABCD analysis of the cavity round trip, using the sum of focal lengths as a starting point. We assume that the two telescopes will have equal lengths $L_{2a} = L_{2b} = L_2$ and examine the validity of that assumption in section 7.3.1.

The final parameter to determine is the small focal length section L_1. This is much less sensitive than the dependence on L_2 but more sensitive than L_3. Smaller values of L_1 reduce the mode diameter in the large mode section, but also reduce sensitivity to variations in L_2. Geometric constraints and the requirement to fit a Pockels cell within the L_1 section constrain the minimum practical length to 100 mm. We use this to constrain the parameter space over which we generate the surface plot.

Following the method in chapter 5, we generate a surface plot varying L_1 against L_2 with the surface representing the mode radius shown in figure 7.3. Gouy phase increases smoothly from the $\phi = 0$ on the $L_2 = 512$ mm asymptote of the contour up to $\phi = \pi$ on the other asymptote. We include contours representing the lowest five Gouy phase values degenerate to higher order modes, three shown in white and two represented by the asymptotes on the edges of the surface. Slices through the surface for different values of L_1 are also provided to indicate the relative sensitivity to perturbations in L_2.

As previously, we select cavity parameters avoiding higher order mode degeneracy, minimising sensitivity to perturbations in L_2 and achieving the target mode radius, indicating our selection with a red point on both plots. We choose $L_1 = 200$ mm providing sufficient space for the Pockels cell and allow small angles of incidence onto the mirrors, reducing astigmatism. We select $L_2 = 513$ mm achieving a large mode radius of 8.8 mm, avoiding degeneracy and minimising sensitivity to perturbations.

7.3.1 Telescope Mismatch

As in chapter 5, the Gouy phase can be tuned over its full range by varying the length of the intracavity telescope, but this is complicated in the bow tie geometry by the presence of two telescopes. In the previous section we assumed these were identical and used this assumption to select optimum parameters, but we must assess this assumption to see if it can be achieved experimentally.

If we allow the telescope lengths L_{2a} and L_{2b} to differ we find that there is a region occupying many mm^2 in which stable cavities exist, see figure 7.4. This is reassuring as mechanically setting the telescopes equal to the nearest millimetre in 0.5 m of path is readily achievable. By tuning the length of either telescope, or both

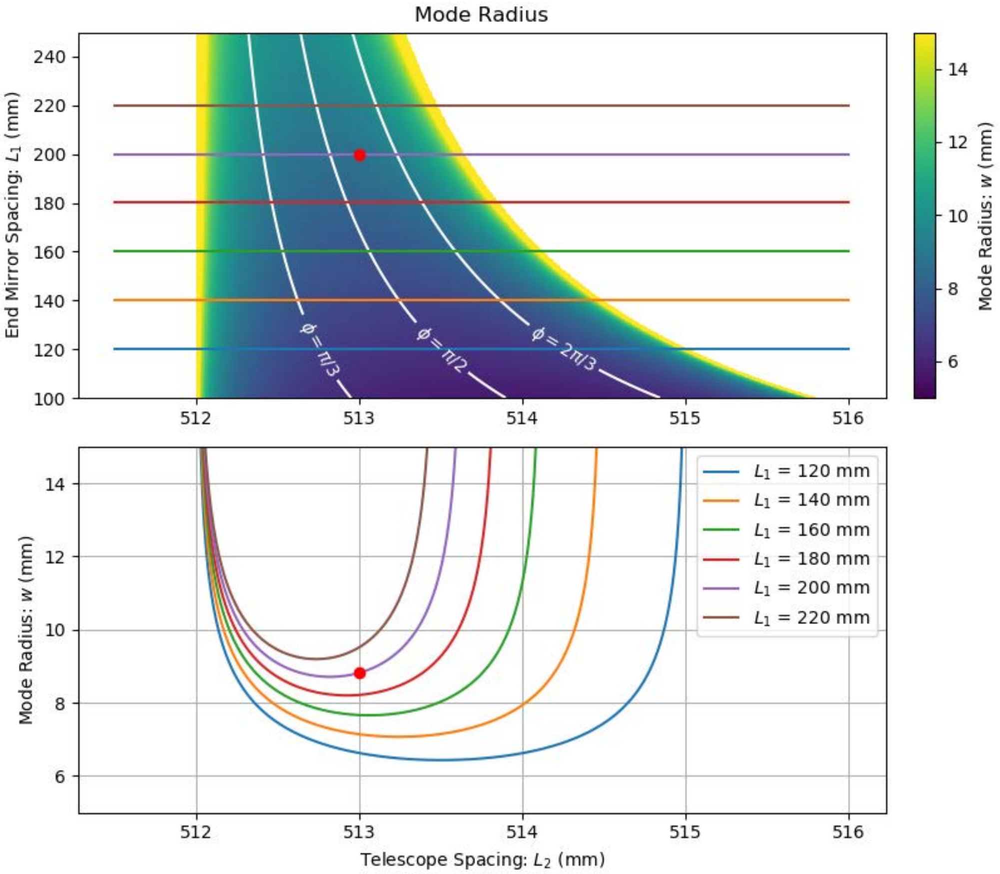

Figure 7.3: Beam radius against L_1 and L_2 surface assuming both telescopes have equal spacing. Gouy phase contours corresponding to higher order mode degeneracy are shown in white. Parameters for the example presented here are indicated by the red spot ($L_1 = 200$ mm, $L_2 = 513$ mm, and $L_3 = 900$ mm).

simultaneously, we are able to scan the Gouy phase over its full range, and explore a range of mode radii. Experimentally, once an initial cavity has been aligned, measurement of the mode diameter and analysis of the higher order mode spectrum will allow any remaining misalignment to be identified and appropriate adjustments made. The relative alignment on the two telescopes is no more tightly constrained than the alignment of any single telescope and is directly comparable to the linear cavity demonstrated in chapter 6.

It is important to note that the plot shown in figure 7.4 evaluates the mode radius in the centre of interferometry region L_3, and this does not necessarily coincide with the location of the beam waist. With mismatched telescopes the location of the waist will shift within and potentially beyond L_3 causing spot sizes on mirrors R_2 to differ. With a mismatch between L_{2a} and L_{2b} of 1 mm, mode radii on mirrors R_2 differ by < 10 μm. Whilst small, for interferometry applications the profile of the beam in L_3 is critical and this may impose a tighter tolerance on telescope mismatch.

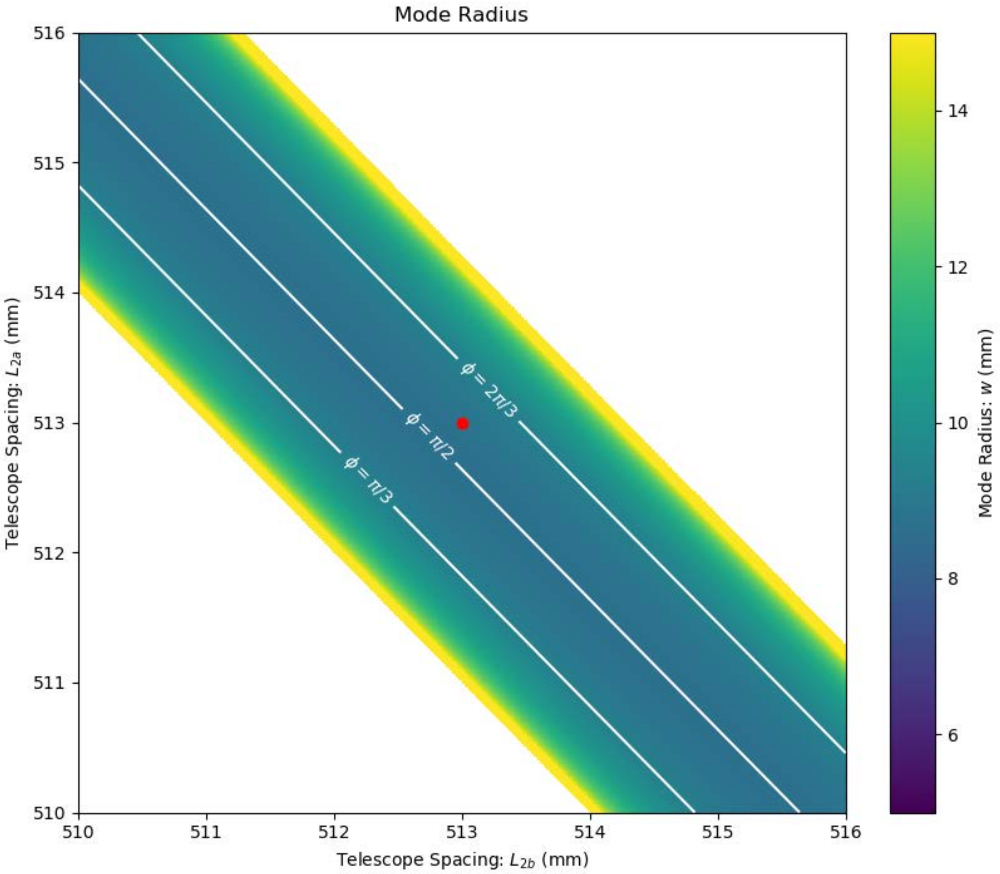

Figure 7.4: A surface plot of beam radius on one of mirrors R_2 against mismatched telescope lengths L_{2a} and L_{2b}. As expected this plot is symmetric about the line $L_{2a} = L_{2b}$. Contours indicating the first five degenerate values of Gouy phase are represented by the edges of the surface and the contours shown in white. The cavity parameters selected in this example are indicated by the red spot.

7.4 Aberrations in Bow Tie Cavities

The bow tie geometry requires non zero angles of incidence on the cavity mirrors. Off axis reflections from spherical mirrors result in spherical aberrations and astigmatism [51]. Whilst the spherical aberration is also present in the linear standing wave geometry with spherical lenses, astigmatism is the direct result of off axis reflections, and without consideration will degrade mode quality. Spherical aberrations are always present after reflection from a spherical surface, and with the short radii of curvature of the mirrors R_1 these aberrations are likely to be significant. We mitigated this in the linear cavity by using an aspheric lens for the short focal length element. Astigmatism increases with increasing incidence angle, so reducing this as far as possible will help to minimise the effects. Aspheric optics such as off axis parabolic mirrors can eliminate both astigmatism, and spherical aberration [94, 95].

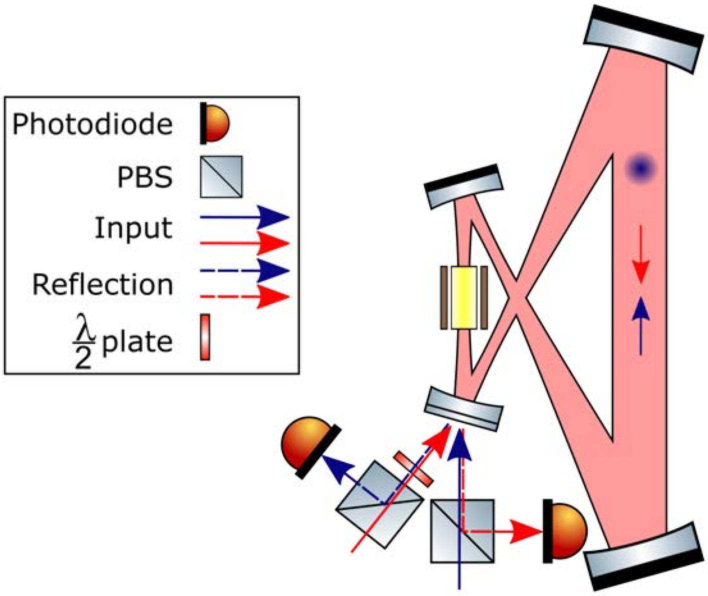

Figure 7.5: The two input beams, indicated red and blue, are in orthogonal polarisations so the reflected signal of one is separated from the input signal of the other using a PBS. Both reflected beams are directed to a photodiode so that an error signal can be generated for stabilisation of each polarisation independently.

7.5 Laser Stabilisation

Laser frequency stabilisation can be achieved with a Pound Drever Hall lock as discussed in chapter 6.5.2. As in standing wave geometries, we couple light into two orthogonal linear polarisations. The ring cavity geometry differs as we require one polarisation in each of the two rotational modes. As shown in figure 7.5, the input reflection overlaps with the input beam in the second polarisation. We separate these with a polarising beamsplitter (PBS) and $\lambda/2$-plate as shown.

The relative phase stability of the two laser polarisations is critical to interferometer performance. This motivates the use of either a phase lock between the input beams, or generating both beams from a common seed and then maintaining phase stable beam paths after they are separated. We propose the use of two feedback loops, one for each polarisation (rotational mode). One loop stabilises the first laser to the cavity (or vice versa), and the second is used to tune the intracavity Pockels cell to keep the second cavity mode on resonance with the second input laser. This allows both input lasers to remain resonant with the cavity and maintain phase stability. This operates even as the frequency difference between them is chirped to compensate for Doppler shifts.

7.6 Pockels Cells

In this bow tie geometry, the Pockels cell is now in a single pass configuration. This is expected to significantly reduce intracavity losses but also halves the available phase shift. To allow the resonant frequencies to be scanned over the full range, the Pockels cell needs to produce a shift of $\pm 2\pi$, which is equivalent to plus or minus the half-wave voltage in a double pass Pockels cell. To achieve this same shift in a single pass configuration an extended length Pockels cell may be needed.

Many Pockels cells are uniaxial birefringent crystals so light propagating at an angle to the symmetry axis experiences strong birefringence. In addition to requiring precise alignment, this also imposes a minimum beam size, where effects due to beam curvature over the length of the crystal do not reduce performance. This conflicts with the desire to minimise the beam diameter to reduce losses from the finite apertures at the ends of the cell. These constraints will need to be considered when selecting the mode size in the Pockels cell and the required clear aperture.

For most applications requiring a Pockels cells, the designer seeks to maximise the electro-optic coefficient, reducing the drive voltage, whilst avoiding residual birefringence in the absence of a field. A common Pockels cell meeting these requirements is a longitudinal[1] Pockels cell based on the r_{63} electro-optic coefficient in KDP [2] [96]. Another common crystal is BBO[3] implemented in a transverse configuration[4]. Both of these are uniaxial birefringent crystals, with the propagation direction aligned with the axis of symmetry. The application of an electric field introduces anisotropy between the principle axes causing birefringence; difference in optical path length for light propagating with each of the two polarisations. This manifests as an increase in refractive index for one principle axis and a reduction for the other. Equation 7.1 shows the refractive indices along the principle axes of a KDP crystal with an electric field E applied along the third principle axis of the crystal [97].

$$n_1(E) = n_o + n_o^3 r_{63} E/2 \tag{7.1}$$

$$n_2(E) = n_o - n_o^3 r_{63} E/2 \tag{7.2}$$

$$n_3 = n_e \tag{7.3}$$

For the Doppler compensation described in chapter 5.2, such symmetric birefringence is exactly what is

---

[1] The electric field is applied parallel to the propagation direction

[2] Potassium dideuterium phosphate

[3] β-Barium Borate

[4] The electric field is applied orthogonally to the propagation direction

required. An atom interferometer, with such a crystal is able to operate at a constant value of single photon detuning Δ, without having to modify the length of the cavity.

However if we wish to have independent control of the two polarisations then these standard crystal geometries are unsuitable. If we remove the requirement for no residual birefringence then this becomes possible. A transverse device based on the r_{63} coefficient in $\bar{4}2m$ class crystals (such as KDP) allows a phase shift to be introduced on one polarisation whilst leaving the other unchanged. From equation 7.2, we align one polarisation with n_2 allowing control, and the other with n_3 which is independent of applied field. For most applications, the strong residual birefringence, and the factor of two reduction in induced phase shift between the two polarisations makes this geometry unfavourable, but in some atom interferometry applications it provides some significant advantages. By arranging two of these crystals orthogonally we have the ability to control the optical path length for each polarisation independently, allowing agile arbitrary control of the resonant frequencies of the two polarisations. This arrangement also cancels out the residual birefringence. Independent control of orthogonal polarisations enables the bichromatic pulse scheme described in chapter 8.2.5. Other crystals can be used for independent polarisation control, selection of the most suitable will depend on technical considerations including optical damage thresholds, temperature dependence, and piezo electric effects [43, 68, 98].

7.7 Conclusion

We have presented a new geometry for cavity enhanced atom interferometry, the magnified bow tie. This geometry reduces the number of transmissive optics required allowing a significant reduction in round trip loss, allowing greater power enhancement and spatial mode filtering. This travelling wave geometry allows one interferometry beam to be injected into each rotational mode, removing the retroreflected spectator beams present in all standing wave cavities. This removes the associated light shifts and scatter and allows optical cavities to be used in high bandwidth system or those operating in microgravity where retroreflected spectator beams are intolerable. We have further presented the design procedure for these cavities applied to a table top example producing a 17.6 mm beam diameter in a cavity less than 1 m tall. Preliminary analysis of the alignment sensitivity for critical dimensions in the cavity suggest that the length constraints are readily achievable. Further analysis is needed to examine the angular tolerances required on the cavity optics. We finally examined the different types of Pockels cells and their effect of cavity enhanced atom interferometry, proposing a method for agile arbitrary orthogonal mode frequency control.

CHAPTER 8

CIRCULATING PULSE CAVITY ENHANCEMENT

8.1 Introduction

In the course of this work we have addressed the critical problems facing lab scale cavity enhanced atom interferometry, providing solutions to achieve large modes, spatial mode filtering, power enhancement and to overcome the Doppler shift limits. However, cavity enhancement is only effective if the pulse duration exceeds the cavity lifetime. As we found in chapter 4.2.3, for the systems constructed in the course of this thesis of 1 m scale with $\mathcal{F} < 100$, the cavity lifetime is orders of magnitude below the the pulse duration so the bandwidth limit is not a concern. But for pulses shorter than, or comparable to the cavity lifetime, the cavity fails to reach its maximum power enhancement. The intracavity field will persist long after the input light is removed resulting in significant pulse elongation. This bandwidth limit described by Alvarez et al. [50] restricts the maximum length-finesse product that can be achieved without significant pulse elongation. In a kilometre scale cavity, the bandwidth limit restricts the maximum finesse to $\mathcal{F} \leq 10$, significantly reducing the mode filtering and power enhancement benefits.

Whilst a kilometre scale system is two orders of magnitude larger than the largest system constructed thus far [99], recent proposals [27–29] using atom interferometry for mid-band gravitational wave [24–26, 100–102] and dark-matter [30, 103] detection require sensors with kilometre scale baselines and momentum separations of order $10^4\hbar k$.

The long base line in these systems causes significant propagation delays of beamsplitter pulses between atom clouds. This poses a significant challenge to standard, multi-photon, interferometry techniques where this propagation delay causes differential laser phase noise to dominate the overall noise budget. Differential single photon interferometry benefits from greatly reduced susceptibility to laser noise and is the most promising technique for future large-scale interferometers [62, 104]. Large momentum transfer (LMT) with sequential single-photon transitions has been demonstrated in ^{88}Sr [105–107], achieving interferometry with a momentum separation of $141\hbar k$ [71]. Extending the technique to $10^4\hbar k$ raises significant challenges. Spontaneous emission must be minimised during the interferometry sequence, motivating the use of transitions to long lived excited states such as those used in atomic clocks [108, 109]. The weak coupling to these long lived excited states requires high optical powers to match the Rabi frequencies that can be achieved on short lived states.

As we found in chapter 2.3, the 698 nm optical clock transition in ^{87}Sr is a suitable candidate for single photon interferometry. With an excited state lifetime of 150 s ($\Gamma = 2\pi \cdot 1$ mHz), spontaneous emission is a negligible source of decoherence [66,69]. With microsecond π-pulses and therefore MHz Rabi frequencies, the $10^4\hbar k$ pulse sequence is completed in a small fraction of the total interrogation time. Unfortunately microsecond pulses require prohibitively large intensities of several kW cm^{-2}. Delivering these pulses with uniform phase also demands flat optical wavefronts [34]. These constraints have prevented momentum separations of $10^4\hbar k$ from being achieved thus far.

Optical cavities offer a solution to both of these problems if the cavity bandwidth limit can be overcome. In this chapter we present a scheme based on circulating, spatially resolved pulses to overcome the bandwidth limit and satisfy the challenging pulse requirements for $10^4\hbar k$ LMT. A circulating pulse drives a π-pulse once per round trip, removing the need to couple a new pulse into the cavity for each beamsplitter. This avoids pulse elongation and overcomes the bandwidth limit, dramatically increasing the possible lengths and cavity finesses that can be exploited [3]. We present parameters suitable for the experimental realisation of $10^4\hbar k$ splitting in a 1 km interferometer using the 698 nm clock transition in ^{87}Sr, and propose a sub-scale demonstration to deliver performance enhancements in 10 m scale devices operating on the 689 nm intercombination line ($^1S_0 - ^3P_1$) in ^{87}Sr.

8.2 Circulating Pulse Interferometry

Consider a travelling wave cavity into which we periodically couple short, spatially-resolved pulses of light. The cavity has a 1 km baseline and a round trip path length of 6 km, see figure 8.1. We use a pulse duration $\tau = 6$ μs, which corresponds to a physical length of 1.8 km and satisfies the condition for spatially resolved pulses; see section 8.2.3. Successive pulses coupled into a single circulating mode are separated by the cavity round-trip time (20 μs) such that they constructively interfere; producing a high-intensity pulse circulating inside the cavity. This periodic train of pulses forms a comb in the frequency domain, but this is identical to free space LMT schemes using periodic short pulses. Light is coupled in away from atomic resonance, and shifted onto resonance using Serrodyne modulation in a Pockels cell once the stationary regime has been reached, see figure 8.2. The circulating pulse intensity is adjusted to drive a π-pulse on the atoms loaded in the cavity, delivering a momentum kick of $\hbar k$ on each round trip. To ensure successive momentum contributions add constructively, we alternate the pulse direction by populating both circulating modes of the cavity. After 100 ms, 5000 round trips have taken place and the target splitting of $10^4\hbar k$ is achieved.

In this beamsplitter sequence, momentum is only imparted to one arm of the interferometer (referred to as the *fast-arm*), leaving the other (*slow-arm*) unaffected. Lifting the initial degeneracy between arms requires careful treatment, outlined in section 8.2.5.

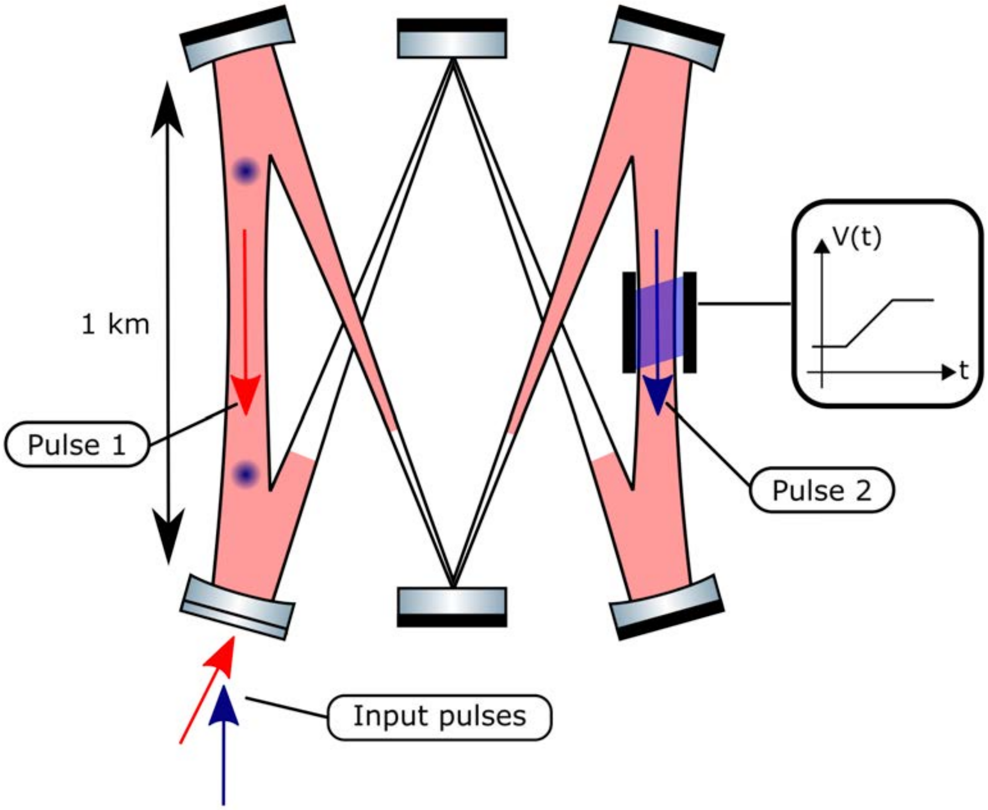

Figure 8.1: Circulating pulses in each of the two rotational modes in this 6 km round trip cavity. On each round trip, additional light is coupled into the cavity to compensate for losses. Serrodyne modulation, applied through a Pockels cell, shifts the frequency of each pulse on each pass to compensate for Doppler shifts. The pulse durations are maximised within the constraint that only one pulse may pass through the atoms (blue) or Pockels cell at a time. [84]

8.2.1 Cavity Build-up and Pulse Requirements

In the following analysis we consider only one of the two running wave modes of the cavity containing the circulating pulses, but note that the results apply equally to both. The response of the intracavity field to the train of input pulses is obtained by solving the propagation equation, see chapter 4 equation 4.1. We have selected parameters such that the cavity is impedance matched. The circulating pulse amplitude increases with each successive input pulse before reaching a stationary value where further pulses only compensate for round-trip losses; see figure 8.2. As we saw in equation 4.14, the stationary pulse intensity is cavity enhanced $I_{circ}(t) = (\mathcal{F}/\pi)I_{in}(t)$, allowing us to achieve $\pi-$pulses inside the cavity with reduced input laser power. A finesse of 4000 enables 6 μs $\pi-$pulses with an input intensity, at the centre of the beam, of only 4.4 $\mathrm{W\,cm^{-2}}$, compared to 5.6 $\mathrm{kW\,cm^{-2}}$ without cavity enhancement. This represents a 1000-fold reduction in required laser power, putting it within reach of existing laser technology; see section 8.2.7.

The total power required depends on the radius of the laser beams, with lower bounds of both atomic and optical origin. High-fidelity pulses can only be achieved if the intensity profile does not vary across the atomic cloud. With a beam to cloud diameter ratio of 20, residual intensity variations have a negligible contribution to fidelity loss. A typical cloud of radius of 200 μm would require a $1/e^2$ beam radius of 4 mm [110], and a total input power of 1.1 W [69, 71]. However, divergence of the Gaussian beam over the 1 km arm length is the more stringent constraint. The minimum beam radius at 500 m, $w = 1.5$ cm, is produced with a beam waist $w_0 = 1.05$ cm. This results in a minimum required input laser power of 16 W. Since the beam radius, and therefore intensity, varies with position along the optic axis, longer atomic freefall times may necessitate increased beam diameters to achieve required axial intensity homogeneity.

The required input optical power decreases linearly with finesse and quadratically with pulse duration. The need to avoid pulse overlap at the atoms constrains the maximum pulse duration; see section 8.2.3. Figure 8.3 shows the minimum optical input power required as a function of round-trip path length, for cavities with a baseline of 1 km and differing values of finesse. The clear reduction in input power motivates the use of large high-finesse cavities. The increase in the time taken to reach the stationary regime (linear in both length and finesse) is not a limiting factor in the proposed scheme.

8.2.2 Interferometric Sequence

Pulses of light are coupled into the cavity far-detuned from atomic resonance, avoiding unintentional interactions during the build-up phase. Once the target amplitude has been reached (white areas in Fig. 8.2), intracavity serrodyne modulation is used to shift the circulating pulse onto atomic resonance. Serrodyne

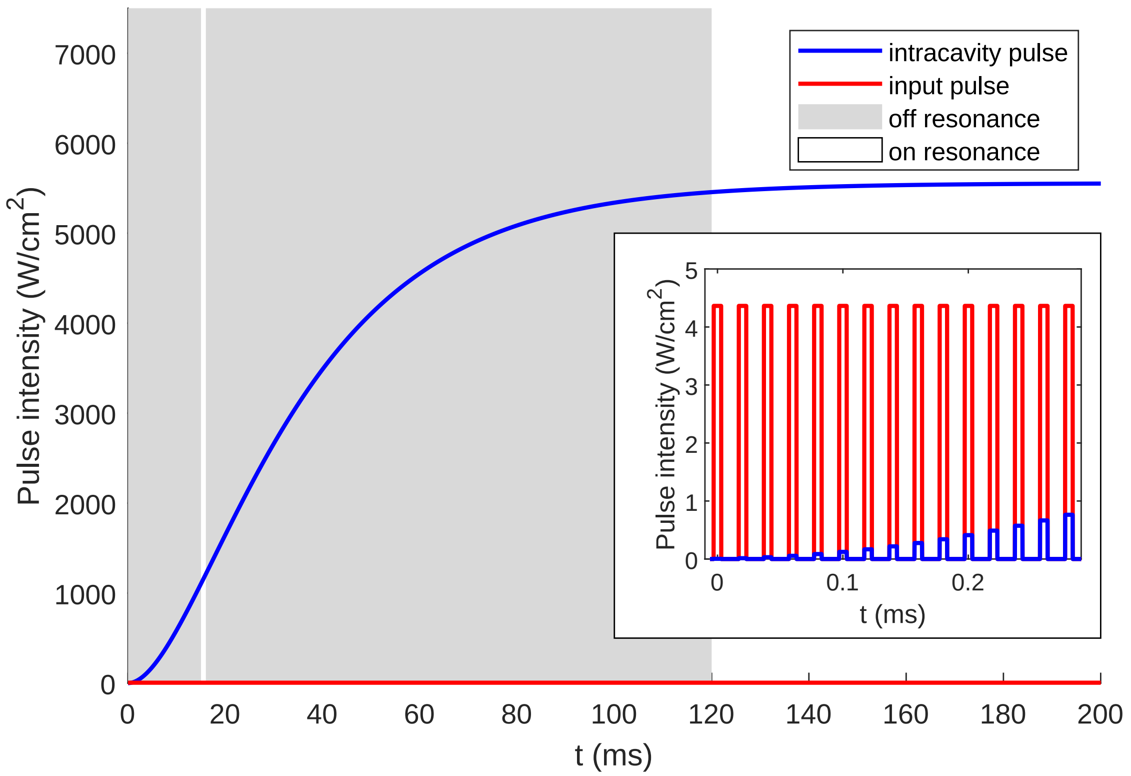

Figure 8.2: Cavity response to a periodic train of spatially-resolved coherent square pulses as a function of time. The input intensity I_{in} is plotted in red and the intracavity intensity I_{circ} in blue. The main plot shows only the intensity maxima, with the full time-dependence of the first input pulses shown in the inset. The system parameters are $L = 6$ km, $F = 4000$, $\tau = 6$ μs. The intracavity intensity increases as input pulses coherently add, before reaching its stationary cavity-enhanced value, which is exactly that of a π-pulse. Grey-shaded areas indicate when the light is off-resonant with the atomic transition. It is shifted on-resonance for one round trip at $t = 15$ ms to drive the initial $\pi/2$-pulse, and again after 120 ms to perform the LMT sequence; see figure 8.4.

modulation is generated by applying a linear ramp to an intracavity Pockels cell. High modulation efficiencies and low losses are essential to reaching the required pulse amplitude; some experimental steps towards realising this are discussed in section 8.2.4.

At $t = 15$ ms the circulating amplitude has reached that of a $\pi/2$-pulse and one of the pulses is shifted onto resonance for a single round trip, see white vertical line on Fig. 8.2. This delivers a $\pi/2$-pulse and is followed by a further serrodyne shift to move the pulse away from resonance whilst the amplitude is increased further.

The LMT sequence requires non-degenerate interferometer arms such that the fast-arm can be uniquely addressed in frequency. We propose two techniques to lift the degeneracy: imparting momentum to the

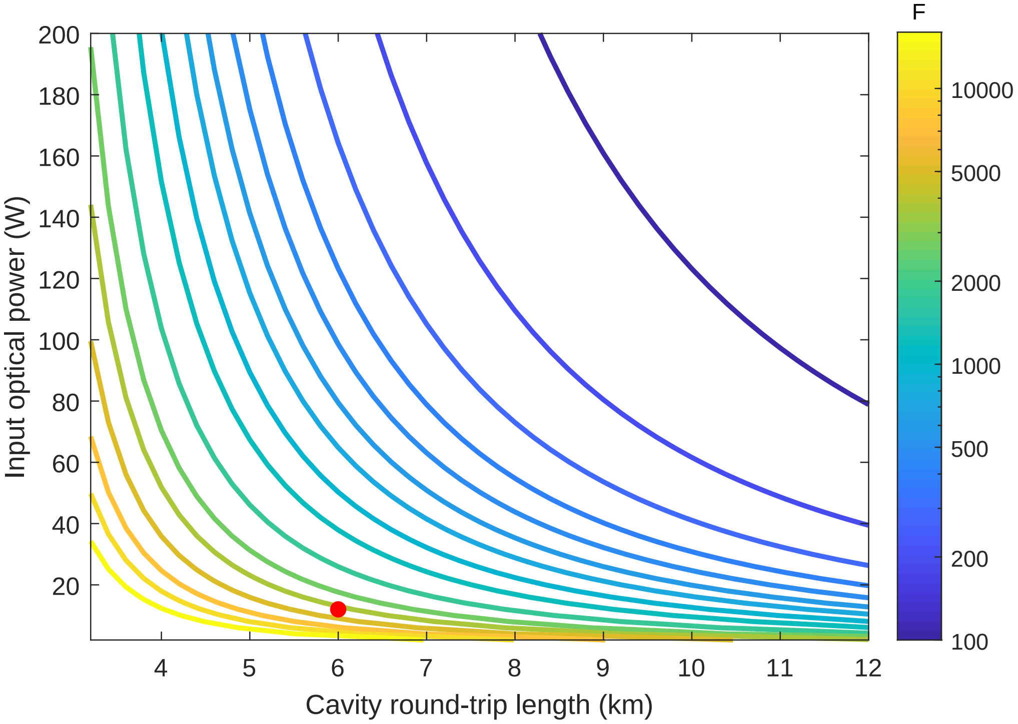

Figure 8.3: Required input optical power as a function of cavity round-trip length and finesse. The cavity baseline is fixed at 1 km, and the maximum pulse duration, minimising power requirements, is selected. This is the limiting value for the pulses to avoid spatial overlap at the atoms, see section 8.2.3. The parameters used throughout are indicated by the red dot.

slow-arm of the interferometer with the 689 nm transition; and bichromatic beamsplitter pulses to track the recoil of both arms; details of both schemes are provided in section 8.2.5.

At $t = 120$ ms, the circulating intensity has reached the value required for a π-pulse and the initial degeneracy has been lifted. Intracavity serrodyne modulation is used to shift both circulating pulses onto resonance with the fast-arm of the interferometer. On each round trip they deliver a pair of sequential counterpropagating π-pulses, imparting $2\hbar k$ of momentum. Recoil shifts and gravitationally induced Doppler shifts are compensated every round trip with further serrodyne modulation. After 5×10^3 round trips, a momentum separation of $10^4\hbar k$ between the interferometer arms has been achieved. The circulating pulses are either dumped from the cavity or serrodyne shifted back away from resonance in preparation for the next beamsplitter. The total sequence duration is less than 1 s, a duration over which spontaneous emission losses remain negligible. Similarly constructed beamsplitter sequences are used to close the interferometer.

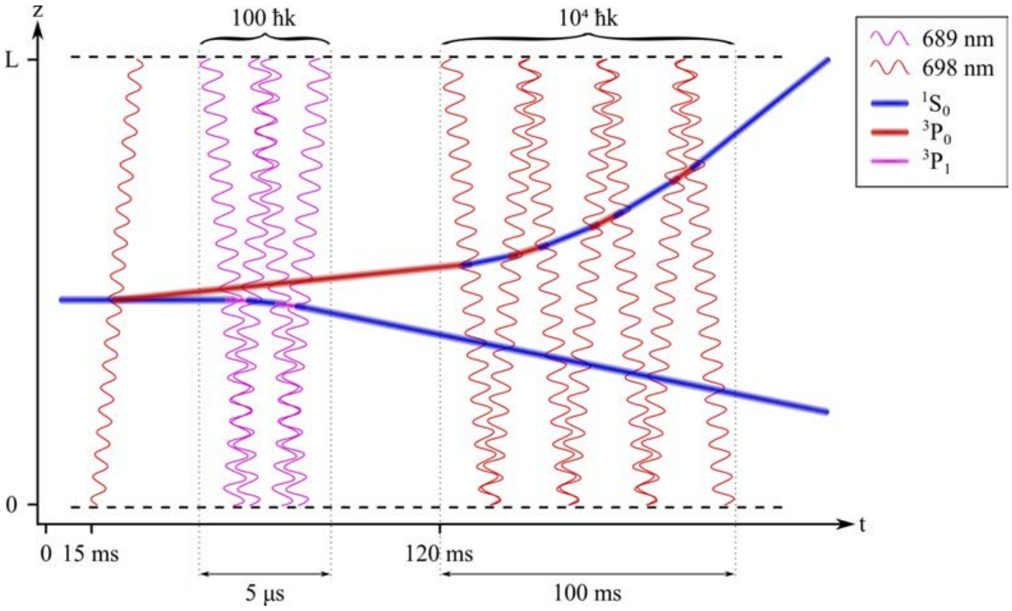

Figure 8.4: Space-time diagram for the large momentum transfer atom interferometry scheme. An initial 698 nm (red, wavy) $\pi/2$-pulse transfers the atoms into a superposition between the ground state, slow-arm (blue), and the excited state, fast-arm (red). Sequential counterpropagating π-pulses on the 689 nm transition (pink, wavy) deliver $100\hbar k$ of momentum to the slow-arm only. With the frequency degeneracy lifted, the main LMT sequence begins at 120 ms, delivering $10^4\hbar k$ of momentum to the fast-arm through counterpropagating π-pulses on the 698 nm transition.

8.2.3 Maximum Pulse Duration

The scaling of input power with pulse duration motivates the use of the longest pulses possible. However, the interferometry scheme described in this work requires successive pulses to alternate in direction and to be temporally distinct when they pass through the atoms and the Pockels cell. This constrains the maximum pulse duration.

We define an exclusive length L_{ex} as the region within the cavity where the pulses must not overlap. Two pulses, of equal limiting duration τ_{max}, propagating in opposite directions, will fully overlap when one pulse leaves the exclusive length and the other is about to enter. This condition is repeated on both sides of the exclusive length. Symmetry considerations show that there is an equal exclusive length on the opposite side of the cavity. Figure 8.5 illustrates the locations of the pulses and exclusive length in a generalised ring cavity. Summing the exclusive length and pulse length the condition becomes clear:

$$\tau_{max} = \frac{1}{2c}\left(L_{RT} - 2L_{ex}\right) \tag{8.1}$$

For pulses with $\tau \leq \tau_{max}$ and correct input timings, singular occupation of the exclusive lengths will be

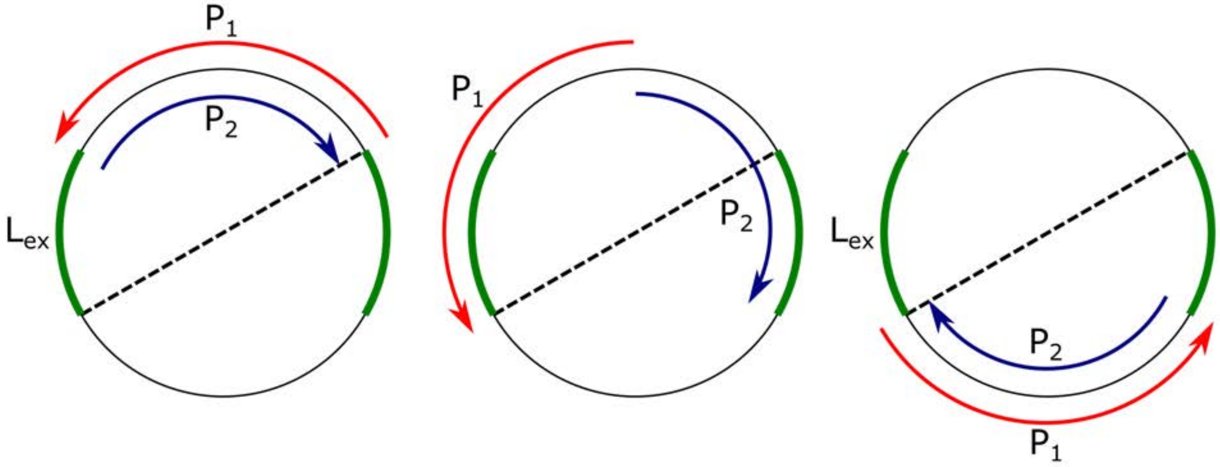

Figure 8.5: This figure shows counterpropagating pulses of duration τ_{max} circulating round the cavity represented by the circumference of the circle. In the first frame pulse-2 has just left the exclusive length and pulse-1 is about to enter it. The relationship between the pulse duration, exclusive length and round trip path length is clear from the first and third frames: $L_{RT}/2 = L_{ex} + c\tau_{max}$

achieved. Pulse durations approaching τ_{max} reduce performance requirements for the cavity and input lasers. The cavity presented in this paper has $L_{RT} = 6$ km and $L_{ex} = 1$ km yielding $\tau_{max} = 6.66$ μs, just exceeding the selected pulse duration of $\tau = 6$ μs.

8.2.4 Control of Frequency and Phase

Frequency and phase shifts arise during the sequence that require active control. There are two sources of frequency shift both caused by the Doppler effect: photon recoil and gravitational acceleration. Recoil shifts are caused by the absorption or emission of a photon, and affect the fast-arm of the interferometer during the main LMT sequence. Each recoil event causes a change in the velocity of the atoms, leading to a Doppler shift of $\hbar k^2/m = 2\pi \cdot 9.4$ kHz per recoil. Gravity accelerates both arms of the interferometer downwards and causes an additional Doppler shift of 14 MHz s^{-1}, or 281 Hz per round trip.

Figure 8.4 shows the fast-arm recoiling upwards on each successive beamsplitter pulse. The Doppler effect will cause the downward-going pulse to appear blueshifted, whilst the upward-going pulse appears redshifted. We track these shifts by applying serrodyne modulation to each of the two circulating pulses. When a pulse travels through the Pockels cell a serrodyne shift is applied. The magnitude and direction of the required shifts is different for the two circulating modes, so the shifts must be applied to the pulses separately. This requires the pulses to pass through the Pockels cell at different times. High efficiency modulation is achieved by applying a single, linear ramp for the duration of the pulse [111]. This is a $\chi^{(2)}$ effect, so the phase shift

ϕ, is proportional to applied voltage:

$$\phi = \pi \frac{V(t)}{V_\pi} = \pi \frac{V_0 + kt}{V_\pi} = \phi_0 + \frac{\pi kt}{V_\pi} \tag{8.2}$$

Frequency is defined as $d\phi/dt$ so a linear phase chirp produces a frequency shift. By adjusting the value of k the frequency can be shifted by up to $1/\tau$ Hz for a standard length Pockels cell, (ramping from $\phi = -\pi \rightarrow \pi$ over the pulse duration τ) and up to N/τ Hz for an extended length $N\pi$-Pockels cell. The performance of this scheme is limited by the modulation efficiency and any losses associated with the modulator itself. As both circulating modes use the same polarisation of light, reflection losses can be reduced by using a Pockels cell with Brewster's angle cut crystal facets [112].

The serrodyne shifts change the phase relationship between the circulating and input light. To ensure constructive interference continues, it is vital that the circulating and input pulses remain in phase. Phase compensation can be achieved in two ways. DC voltages can be applied to the intracavity Pockels cell to ensure that the phase on the input mirrors is constant for every pulse in both circulating modes. The voltages required will differ every round trip, and be different for each circulating mode. Longer Pockels cells will increase flexibility to introduce a phase shift whilst leaving enough headroom for modulation. A simpler approach experimentally is to adjust the phase of the input pulses on each round trip to match that of the circulating field. A Pockels cell or acousto-optic modulator on each of the input beams could achieve this in an agile and controllable way. Regardless of which phase compensation technique is adopted, the frequency of the input beams must also be tuned to track the circulating fields.

8.2.5 Initial Arm Degeneracy

Our scheme relies on velocity selective pulses such that only one arm of the interferometer is addressed, leaving the other unaffected. However, the large Rabi frequency ($\simeq$ 80 kHz) and small initial frequency separation from the first $\pi/2$-pulse (9.4 kHz) results in the two arms being initially degenerate. The two arms cannot be discriminated in frequency with high-fidelity until the frequency separation exceeds the pulse bandwidth. Since one recoil of $\hbar k$ produces a Doppler shift of $\hbar k^2/m = 2\pi \cdot 9.4$ kHz, $\simeq 10 - 100$ beamsplitters are required to lift this degeneracy.

One method to open the interferometer is to create the initial momentum separation with π-pulses on the ${}^1S_0 -{}^3 P_1$ 689 nm transition. The initial $\pi/2$-pulse on 698 nm splits the atoms into a superposition of the long lived excited state and the ground state, referred to as the fast and slow-arm respectively. We apply one hundred sequentially counterpropagating π-pulses on the 689 nm transition, imparting $100\hbar k$ of momentum to the slow-arm on the interferometer whilst leaving the fast-arm in the excited state unaffected. The resulting Doppler shift is $100\hbar k^2/m \simeq 2\pi \cdot 1$ MHz, greatly exceeding the Rabi frequency of the clock pulses, ensuring that the fast-arm of the interferometer can be uniquely addressed.

The 689 nm transition allows for much higher Rabi frequencies $\sim$ 100 MHz, enabling 10 ns π-pulses without cavity enhancement. The 100 pulse sequence is completed within 5 μs: 3.3 μs for the pulses to propagate 1 km between the clouds and $\simeq$ 2 μs for 100 pulses. The pulse bandwidth is large compared to the total Doppler shift so we achieve high-fidelity beamsplitters without Doppler compensation [71]. The $^3P_1$ state has a lifetime of 21.6 μs requiring a rapid pulse sequence ending in the ground state to minimise losses due to spontaneous emission. This beamsplitter sequence can be accommodated within the general scheme depicted on figure 8.2 and performed during the cavity build-up time, when the 698 nm pulses are far detuned from atomic resonance.

An alternative approach circumvents the issue of arm degeneracy, using only the 698 nm clock transition, by utilising two polarisation modes in each pulse. The two polarisation modes are independently serrodyne shifted to track the Doppler shifts experienced in both arms of the interferometer, redshifting one polarisation whilst blueshifting the other. As both interferometer arms recoil, the total number of beamsplitter pulses required to achieve a given momentum separation is halved.

The magnitude of the required shifts is slightly larger for the downward accelerated arm due to the gravitational contribution. The different magnitudes and directions of the required chirps necessitate independent modulation of the two polarisations. This requires two Pockels cells, each applying a phase shift to one polarisation whilst leaving the other unchanged, an arrangement described in chapter 7.6. Phase compensation can be achieved with the same methods discussed in the section 8.2.4, but must now be applied to both polarisations simultaneously. This dual polarisation, dual frequency scheme requires careful control of the light intensities on a pulse-by-pulse basis to ensure this bichromatic light field delivers high-fidelity π-pulses to both arms on each round trip. The details of the specific powers and frequencies required to achieve this are beyond the scope of this work.

8.2.6 High-Fidelity LMT

Reaching a momentum transfer of $10^4\hbar k$ requires 10^4 beamsplitter pulses, which must be of high-fidelity to maintain contrast through the interferometer. There are several factors limiting the fidelity of an atom-optic pulse: the thermal velocity spread of the cloud (which results in a dispersion in the Doppler shifts), the spatial variations of the beam intensity at the scale of the cloud, and the spontaneous emission losses. Although this discussion is not specific to our scheme, we demonstrate that we can maintain sequence fidelity at $10^4\hbar k$, and identify the limiting parameter. The fidelity improves with increased beam-to-cloud diameter ratio, with a strong dependence up to a ratio of 20. At this ratio the intensity is approximately constant at the scale of the cloud and further increasing the beam diameter results in only a minor improvement in fidelity. The fidelity also improves for reduced atom cloud temperature, and in our scheme temperature is the limiting parameter. This arises from the Doppler shift dispersion inside the cloud, and not from the spatial expansion of the cloud during its propagation, which remains negligible. For a cloud radius of 200 μm (beam-to-cloud ratio of 75), the sequence fidelity is plotted for various cloud temperatures, see Fig. 8.6. We observe that to achieve sufficient contrast at the output of the interferometer, a temperature of a few nanokelvin is required for $10^4\hbar k$ LMT [64].

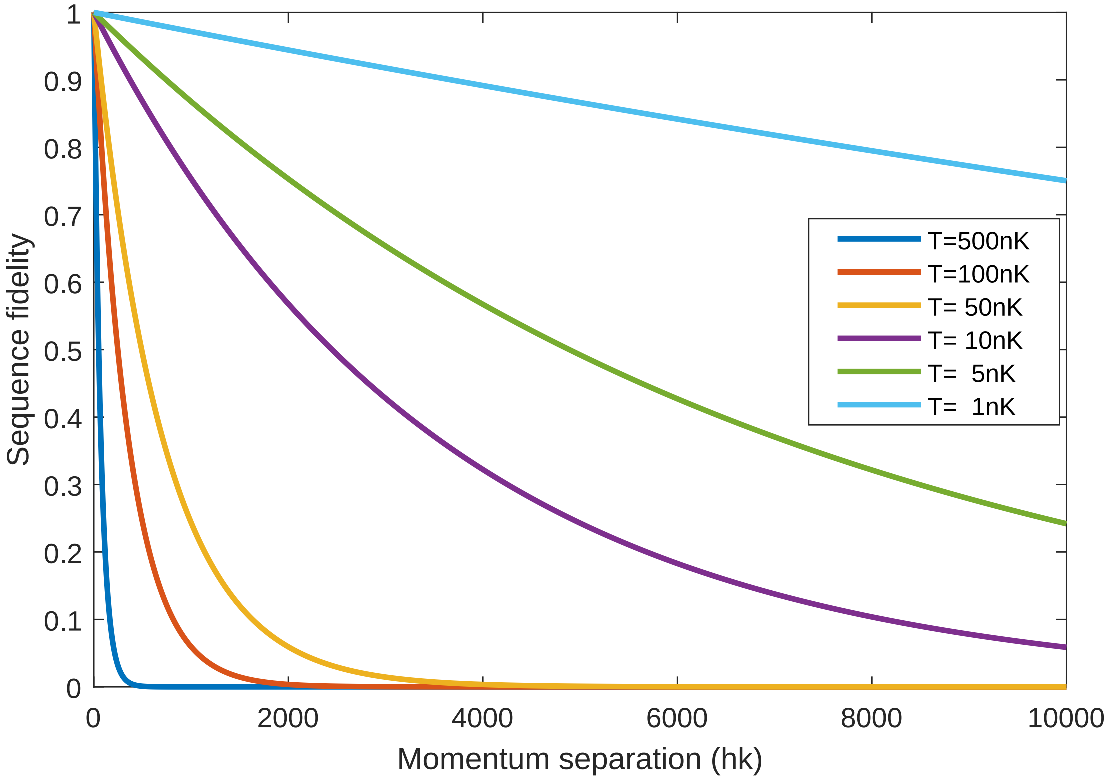

Figure 8.6: Fidelity of the whole LMT sequence as a function of momentum separation, for various atomic temperatures. The sequence fidelity is obtained as the cumulative product of individual pulse fidelities, which are obtained by averaging the transition probability over the cloud instantaneous spatial and velocity distributions. The initial cloud radius is 200 μm and the beam radius is 1.5 cm. To obtain a sufficient contrast at the end of the $10^4\hbar k$ LMT sequence, a cloud temperature less than 10 nK is required. Cloud expansion, Doppler shift compensation and spontaneous emission are included in the model. The pulse bandwidth is neglected, but any resulting errors can be compensated with frequency and intensity adjustments [113, 114].

8.2.7 Laser System

This scheme places demanding constraints on the input lasers, requiring narrow linewidth, rapid tunability, and high output power. It will require at least two separate lasers to inject light into both circulating modes of the cavity. The coherence length of the lasers must exceed the average distance travelled by a photon within the cavity. This ensures that successive input pulses continue to constructively interfere with the intracavity circulating pulse. With a cavity photon lifetime of $t_c = L\mathcal{F}/\pi c \simeq 30$ ms, a laser linewidth of ~ 1 Hz will ensure the limit is comfortably met. The optical paths on the input to the cavity must also be phase stable at ~ 1 Hz level. These performance levels are demanding, but regularly achieved in optical clock lasers operating on the 698 nm transition [115, 116].

Clock lasers do not typically produce the output powers required for this scheme, so we propose the use of a clock laser as the master to injection-lock a high power slave [117]. Commercially available high power Ti:sapphire lasers generate ≥ 5W, so the required output of 16 W would require the coherent combination of four of these. The pulsed nature of the output may allow the use of a single Q-switched slave laser, reducing the system complexity. Injection locking also simplifies frequency and phase compensation which may be accomplished by appropriate modulation of the master laser, prior to injection seeding. This retains the stability properties of the master laser and allows modulation to occur at low power levels.

8.2.8 Implementation in Smaller Systems

This scheme could be tested on a smaller system operating on the 689 nm $^1S_0 -^3 P_1$ transition in ^{87}Sr, where higher Rabi frequencies enable shorter pulses and correspondingly smaller cavities. A 40 m-round-trip cavity of finesse 1000, with 16 ns input pulses every 133 ns, will require only 1.2 W of laser power to implement π-pulses with a beam waist of $w_0 = 15$ mm. Generating controlled voltage ramps for serrodyne shifting for these nanosecond scale pulses is technically demanding, and it may take multiple round trips to accumulate a large enough shift to move the pulse onto atomic resonance. The atoms may need to be shelved into a dark state whilst this shifting takes place. Due to the large pulse bandwidth, no Doppler shift compensation is required as both arms are addressed with high-fidelity. Whilst spontaneous emission will limit the performance on this transition below the target of $10^4\hbar k$ momentum separation, it will still provide valuable enhancement to these lab-scale systems, and serve to validate the scheme.

8.3 Conclusion

We have presented a novel scheme for cavity enhanced atom interferometry to enable extremely large momentum transfer beamsplitters in large scale atom interferometers. Intracavity serrodyne modulation allows circulating, spatially resolved pulses to be recycled, overcoming cavity lifetime elongation and the pulse bandwidth limit. Serrodyne modulation is used to shift the pulse on and off resonance and compensate for photon recoils and gravitational Doppler shifts.

We analyse the case of a kilometre scale atom interferometer for gravitational wave detection, and find that a cavity with 6 km round trip path length and a finesse of $\mathcal{F} = 4000$ can generate a circulating pulse intensity of 5.6 $\mathrm{kW\,cm^{-2}}$ with only 4.4 $\mathrm{W\,cm^{-2}}$ at the input. When applied to the ^{87}Sr 698 nm clock transition this enables 6 μs π-pulses in a mode of 1.5 cm radius with an input laser power of only 16 W. The overall sequence fidelity is found to be limited by the temperature of the atomic cloud. A beamsplitter with $10^4\hbar k$ momentum separation between the arms and combined fidelity > 0.25 requires a vertical velocity spread of 1.2 $\mathrm{mm\,s^{-1}}$, corresponding to a temperature selectivity of 5 nK. Further reductions in cloud temperature increase fidelity and hence the maximum total momentum separation. This is the first practical, albeit challenging, approach to the generation of short, high-fidelity pulses on this transition.

Circulating pulse interferometry can also be applied to 10 m atom interferometers operating on the intercombination line in ^{87}Sr at 689 nm. Resonant power enhancement and spatial mode filtering will allow for an increase in fidelity and therefore the possible momentum separation in these systems, improving sensitivity. By overcoming the bandwidth limit we have enabled optical cavity enhancement of the largest proposed atom interferometers. Circulating pulse cavity enhanced atom interferometry offers a step change in large momentum transfer atom interferometry. With a thousand-fold increase in optical intensity, it enables large scale atom interferometers for gravitational wave detection and new tests of fundamental physics.

CHAPTER 9

CONCLUSIONS

We have laid the foundations for the widespread implementation of optical cavity enhancement in atom interferometry. These advancements have overcome the central issues facing cavity enhancement and enable performance improvements across the full spectrum of atom interferometers. We have further constructed an apparatus to investigate the use of high power beamsplitters on a high bandwidth atom interferometer, conducting an incipient gravity measurement.

We have demonstrated a scheme for cavity enhanced atom interferometry that for the first time combines a large mode diameter with the capability to provide Doppler compensation, reduction of wavefront aberration through spatial mode filtering, and power enhancement. This overcomes the two key barriers preventing high performance use of cavity enhanced atom interferometry, while realising the two primary benefits. This is achieved while also being robust to changes in cavity length, thus avoiding the extreme dimensional tolerances encountered at the edges of geometric stability. The techniques described enable large-mode, high-finesse cavity experiments capable of compensating for arbitrarily large Doppler shifts due to long free-fall times, as well as the parameters required for large momentum transfer orders. Furthermore, this scheme could be applied to state-of-the-art, long baseline atom interferometers, with 10 m baselines and 2 s free-fall times [118], while still remaining within the limits of cavity lifetime elongation [50]. As such, this scheme is highly applicable to the full range of atom interferometers. For fundamental physics, the scheme could be applied to increase optical intensities and reduce wave-front aberrations, increasing the space-time area through large momentum transfer without imposing limitations on free-fall time. For quantum technology sensors, the scheme could provide reductions in the required laser power, leading to cheaper sensors, or operation on power constrained platforms such as satellites, while also providing a route to increased sensitivity through robust cavity enhancement for large momentum transfer.

We have also presented a novel scheme for cavity enhanced atom interferometry that overcomes the cavity lifetime elongation and the pulse bandwidth limit: the one remaining restriction on cavity enhanced interferometry. Intracavity serrodyne modulation allows circulating, spatially resolved pulses to be recycled, and enables extremely large momentum transfer beamsplitters in large scale atom interferometers for the first time. We analysed the case of a kilometre scale atom interferometer for gravitational wave detection, and found that a cavity with 6 km round trip path length and a finesse of $\mathcal{F} = 4000$ can provide a thousand fold increase in circulating optical intensity. When applied to the ^{87}Sr 698 nm clock transition this enables 6 μs π-pulses in a mode of 1.5 cm radius with an input laser power of only 16 W. This is the first practical, albeit challenging, approach to the generation of short, high-fidelity pulses on this transition. With a sufficiently low atomic cloud temperature this scheme enables momentum separations between the arms of the interferometer of above $10^4\hbar k$. This represents a step change in large momentum transfer atom interferometry and enables large scale atom interferometers for gravitational wave detection and new tests of fundamental physics.

We have overcome the Doppler limit, the bandwidth limit, and enabled large modes and spatial filtering simultaneously. These improvements extend previous efforts in cavity enhanced atom interferometry into a new regime with a myriad of potential applications. Atom interferometers requiring the very best performance will benefit from the increased fidelity enabled by spatial mode filtering and resonant power enhancement. Ultra-portable quantum technology applications will use resonant power enhancement to reduce the size and power consumption of their lasers.

Integration of these cavity designs with atom interferometers is ongoing. Colleagues within the university of Birmingham are developing large momentum transfer capability within the AION consortium and cavity enhancement is a key part of the strategy. A high bandwidth system also under construction at Birmingham will employ cavity enhancement in this regime for the first time. Cavity enhancement will become a standard feature of atom interferometers going forward.

APPENDIX A

ALIGNMENT PROCEDURES

The cavity presented in chapter 6 has many optical elements and a correspondingly large number of degrees of freedom making the alignment challenging. In the following appendix we will discuss the procedure developed in the course of this work. The general strategy is to start with beams that are horizontal, and parallel to the rail. We then add optics such that they are well centred with the beam, and position them to achieve beam profiles consistent with the theoretical model. By ensuring that the beam is horizontal, parallel, and well centred on the optics, fine adjustments to lens positions or mirror tilts will not produce large coupled shifts in other dimensions. As we are adding components to match the beam, we must begin with the beam delivery board.

A.1 Beam Delivery Board Alignment

Coarse alignment of the delivery board is set by dowel pins in the optic mounts, and by starting with mirrors in a neutral position. The optics are added sequentially with a focus on maintaining horizontal beams, parallel to the board and passing centrally though the optics. Working through the beam path methodically from the collimator to the cavity will ensure the beam is well aligned. The beam delivery board with labelled optics is shown in figure A.1

A.2 Collimation and Parallelism

The Raman beams are delivered to the board through optical fibres, where they are collimated to a beam diameter of 830 μm. This is performed in advance of cavity alignment on a separate optical rail with beam diameters measured with a CCD. The target beam divergence was determined analytically in advance and

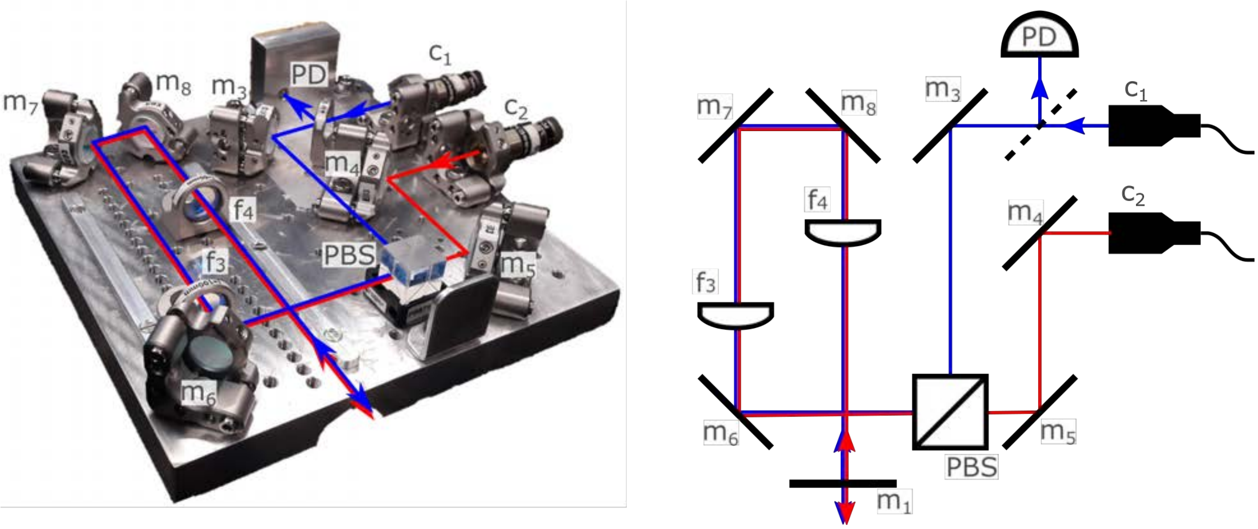

Figure A.1: Light is delivered to the cavity from this custom beam delivery breadboard. It combines the two input polarisations on a PBS. Lenses f_3 and f_4 form a telescope to correct the beam size and bring them to a focus on cavity mirror m_1. Mirrors m_6 and m_8 are used to fine tune the spatial overlap with the cavity mode. The photodiode and beam sampler are used for laser frequency stabilisation.

included compensation for the 40 mm optical path length from collimator-1.

The alignment procedure begins with collimator-1, once mirror-3 and the PBS (polarising beamsplitter) are in place on the delivery board. The collimator should be rotated on its axis to maximise reflection from the PBS and then locked into place; in practice this is done by minimising transmission which is more sensitive. Mirror-3, and the kinematic stage on collimator-1 are adjusted to set the beam horizontal and centre it on the PBS. Mirror-6 can now be added and the PBS rotated (coarsely) to centre the beam on it; mirror-6 is temporarily removed to check the parallelism of the beam over longer distances. Following this, it should be permanently replaced and adjusted to produce a horizontal beam parallel to the board and centred on mirror-7. Mirror-7 was also removed to check this alignment over longer distances. The beam delivery board was then mounted to the rail and parallelism was verified by adjusting the mirror until the beam position on the CCD was invariant under translation along the rail.

A.3 Lens Centration

The next task is to add the mode matching lenses to the beam delivery board. Lens-3 is added, with mirrors-3 and 6 adjusted to centre the beam on this lens. The lens slide should be mounted as this allows the lens to be added and removed repeatably. The coarse centration can be verified by examining back reflections from the lens. If these are close then we can proceed to fine centration adjustment with the beam profiler on the rail. The beam profiler should be placed close to the beam delivery board. When centration is achieved the spot location will not change when lens-3 is added or removed. If introducing the lens translates the beam up on the beam profiler then the beam is too low, and should be shifted up. If the lens translates the beam left, it is too far to the right and should be translated left. These adjustments should be made iteratively on mirror-3, as follows:

1. Measure position of the beam on the CCD. This is the reference position.
2. Add lens-3 and measure the new position on the CCD.
3. Remove the lens.
4. Adjust mirror-3 to shift the beam half way between the reference and translated positions. This is the new reference position.
5. Iterate until these two locations coincide.

Once this has been achieved satisfactorily, the lens should once again be removed and mirror-6 should be adjusted to ensure the beam is still parallel to the rail. Some iteration between mirrors 3 and 6 may be required to reach optimum alignment following which lens-3 should be removed once more.

Mirrors 7 and 8 can now be added in turn. They should start in a neutral position and be adjusted to produce beams which are parallel to board and rail. If the beam was centred through lens-3, then adjusting mirrors 7 and 8 to maintain the same beam location on the CCD should provide a very good starting point for lens-4. The alignment procedure is identical to that provided above. Mirror-7 should be adjusted to minimise deviations close to the board, before mirror-8 is used to ensure parallelism with the rail. Due to the short distance between mirrors 7 and 8 additional iterations will be required.

A.4 Beam Overlap

With the board fully aligned for collimator-1 and the lenses removed, we can align collimator-2. This should be rotated to maximise transmission through the PBS, and mirrors 4 and 5 walked until overlap with beam-1 has been achieved. This is verified with the CCD at several points along the rail. An iris can be added on the output of the beam delivery board to allow this alignment to be restored.

A.5 Cavity Optics

With a collimated beam aligned to the cavity rail, we are able to verify the mounting height of cavity optics. The lenses are both mounted on fixed height posts without lateral translation, at the height calculated to match the lens centre height from the beam delivery board. Each lens should be inserted into the beam, an initial visual check can confirm if the beam is passing through the centre of the lens. Adjustments to the height should be made with shims in the post. Any tilt control is set by examining the back reflection from the lens and adjusting the tilt to make the reflection overlap with the input beam as closely as possible.

The Pockels cell height is adjusted with shims such that the beam passes through the centre of the aperture. The horizontal position is also adjusted at this point with the translation stage. Roll should be set to coarsely align the Pockels cell with the polarisation axes of the input beams.

The transmission photodiodes should now be positioned. The height and positions of the diodes and their lenses should be adjusted to bring the light to focus on the surface of the diode. This is does not need to be particularly precise but it is much easier to set without the cavity mirrors in place. The mirrors should be set to match the cavity beam height; if corrections are required, shims can be used to achieve beam centre. The tilt of the mirrors should be set to maximise overlap of the reflected beam. In this system it was possible to observe light coupled back into the fibre as scatter through the fibre jacket when observed with a camera or IR viewer. This provided a precise indicator that the mirror had been set correctly.

A.6 Input Beam Size

Once this procedure is complete, the beam is well centred through the lenses on the beam delivery board, and all of the cavity optics are set up to operate with a beam at this height. The next task is to produce a focus of the correct size on the input cavity mirror. The mode matching lenses should be positioned at their calculated positions on the beam delivery board. A CCD placed at the location of the input mirror measures the focused spot size; see figure A.2. Lens-4 is translated to produce the target spot size on the CCD. The CCD should be translated along the rail to verify this measurement is at the focus. If not, lens-3 should be translated to compensate and the process iterated. Bolt slots in the lens mounts, combined with the alignment slide, allows manual sub-mm adjustment of the lens location and precise generation of the target spot size and location. We required a spot size of diameter 368 μm and produced 363 μm and 377 μm with the two beams.

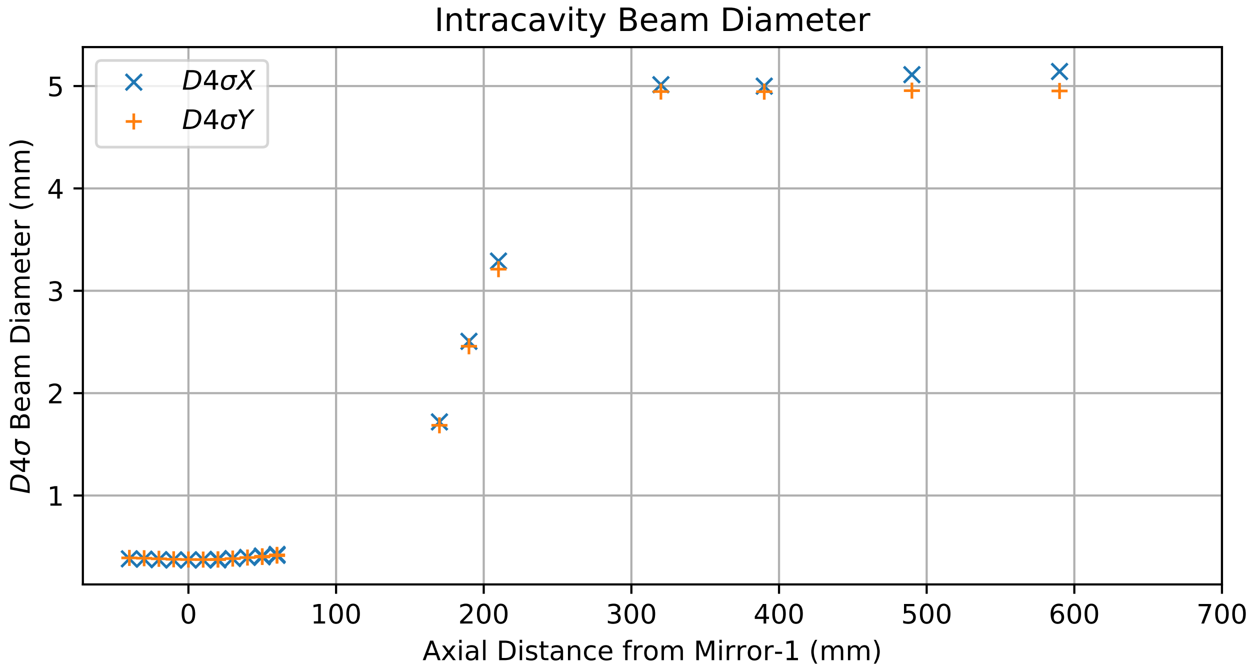

Figure A.2: The $D4\sigma$ beam diameter as a function of axial position is measured with a CCD. The cavity input mirror was removed to enable this measurement.

A.7 Cavity Optics Alignment

The cavity optics are ready to be placed. We begin with cavity lens-1. This should be placed at the calculated distance from the input mirror (in our case 9.3 cm) and then fixed down. This lens is on a fixed mount, and the telescope length is defined relative to this position. The CCD should be used to verify the beam is propagating parallel to the rail after passing through this lens. If deviations are observed, small adjustments can be made to mirrors 6 and 8 to compensate.

The CCD should be translated along the cavity to a distance L_2 from the first lens and translated until the beam diameter expected at lens-2 is observed. The position is marked, the CCD removed and lens-2 inserted. Mirrors-6 and 8 can be tweaked to keep the beam centred on this lens and the beam propagating through L_3 horizontal. The CCD should be moved to the location of M_2 the large mode mirror within the cavity, and lens-2 should be coarsely adjusted until the the onward beam is collimated. The lens-2 should be fixed down and fine adjustments made with the translation stage to produce the theoretical beam size on the CCD at M_2. The target is to achieve a large collimated mode in this section L_3 and this should be prioritised over the precise diameter of this mode.

At this point it is important to check that there is still a signal on the transmission photodiodes, and to adjust the transmission optics to maximise this. Once the mirrors are in place this signal will be strongly attenuated and difficult to align from scratch. Mirror-2 is placed at the target distance L_3, and as in the initial setup should be adjusted to reflect the input light back into the fibre. Due to the long path length between this mirror and the fibre, this adjustment is very sensitive. The input mirror is now placed, and adjusted to retro-reflect back into the fibre. Due to the shorter path length this is a far less sensitive adjustment, but this reverse coupling should done as efficiently as possible. If the input laser is now set to scan over a frequency range of approximately two free spectral ranges, a comb of low intensity narrow peaks should be observed in the cavity transmission spectrum. This indicates that we have formed a cavity but it is not yet correctly aligned. The input mirror tip-tilt should be adjusted to maximise the largest peak.

Optimisation of the spatial overlap between the input beam and the cavity mode is the final alignment step. We attempted to construct the cavity around the input beam but invariably there will be some mismatch between our input beam and the mode of the cavity we have now constructed. By adjusting mirrors 6 and 8 on the beam delivery board the relative size of the peaks in the comb can be adjusted. This process is similar to coupling into an optical fibre and will require a combination of tip, tilt, and walking the beam. One peak will emerge as being larger and more persistent that the rest and the goal is to maximise the height of this peak and minimise the height of the others. The reflected signal should also be examined at this point; once significant power has been coupled into the fundamental mode a dip appears in the reflected signal, as shown in figure A.3. This provides a measure of mode matching efficiency. In this case we observe a reflected signal $< 3\%$ but due to uncertainties in the background level claim 90% as a conservative estimate. This confirms that beam size and spatial overlap have been set correctly.

Additional cameras mounted to the rail to image scatter from the optics simplify alignment and reduce misery. They provide a simple indication of gross misalignment where the beam is no longer passing through the centre of an optic, or in some cases missing the optic entirely. In this system six webcams were used to monitor the beam delivery board, both cavity mirrors, both lenses, and the fibres. Despite operating the cavity at a wavelength of 780 nm, after removing the IR filters [119], these webcams provided a simple and low cost way of monitoring the coarse alignment of the system.

A.8 Pockels Cell Alignment

The Pockels cell should be placed into the aligned cavity, and the height adjusted so the beam passes through the clear aperture. The tip, tilt, and roll of the Pockels cell must be aligned with the optical axis of the cavity and the polarisation aligned with the input beams. When the cell is perfectly aligned, and illuminated

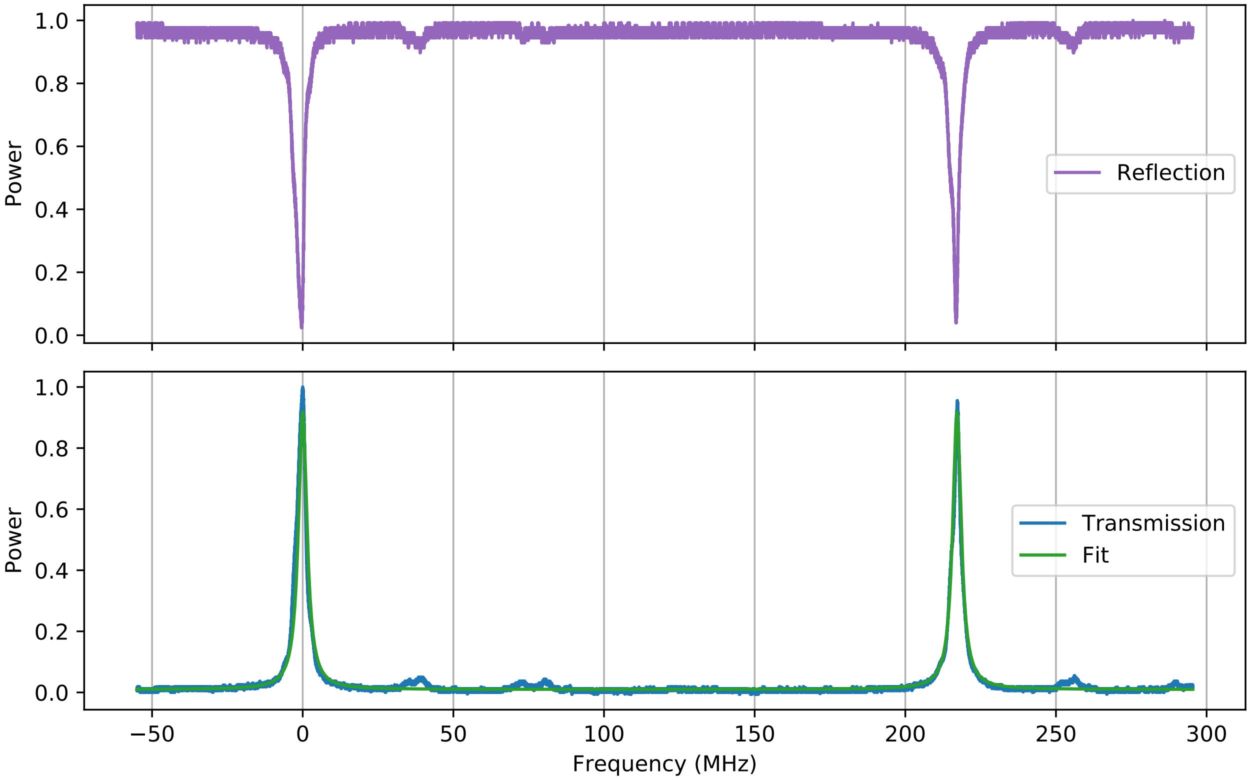

Figure A.3: Cavity transmission and reflection spectra without the Pockels cell. The transmission spectrum is fitted and has a finesse of $\mathcal{F} = 64$. The features in the spectrum between 40 and 100 MHz are higher order modes. The $< 3\%$ reflection on resonance suggest excellent matching to the fundamental mode.

with a single polarisation, the transmission spectrum will appear as it did without the cell. With both polarisations present the transmission signal may appear as two peaks separated in frequency due to residual birefringence of the crystal. An example spectrum is shown in figure A.4. When a low frequency triangle wave voltage is applied to an aligned Pockels cell, the separation between the peaks changes proportionally to the applied voltage, but the relative amplitudes remain unchanged. Any variation in the height of these peaks, or appearance of additional peaks are indicative of incorrect tip and tilt alignment.

The roll adjustment of the Pockels cell mount was strongly coupled to the tip and tilt, so we adjusted the polarisation of the cavity input light with a half-wave plate. Whilst this complicated the implementation of polarisation dependent transmission detection, it was justified by the alignment advantages it offered.

When the cell is initially placed into the cavity, and illuminated with a single polarisation, a large number of transmission peaks were observed. This is caused by the strong birefringence exhibited by a Pockels cell when the beam is misaligned from the crystal axis. In the BBO crystal[1] used in this system, the

---

[1] β-barium borate Pockels cell, Gooch and Housego, Light Gate 3, AR coated at 780nm

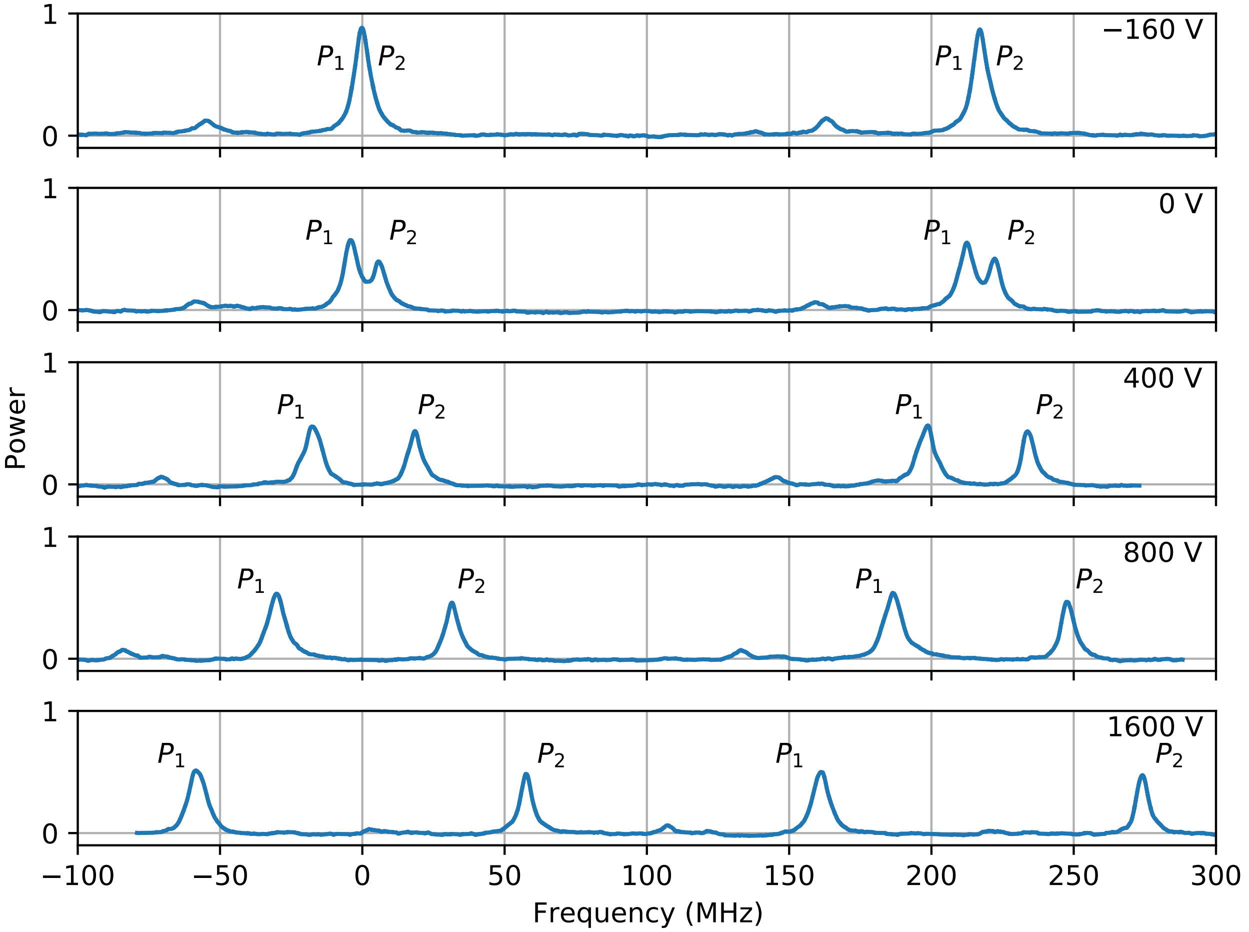

Figure A.4: Increasing the voltage applied to the Pockels cell induces birefringence into the cavity. The orthogonally polarised cavity modes are separated in frequency, from the degenerate value at -160 V to 114 MHz at 1600 V applied. The initial offset compensates for residual birefringence in the crystal. Ramping the voltage at 390 $\mathrm{V\,s^{-1}}$ compensates for the 25.1 $\mathrm{MHz\,s^{-1}}$ Doppler shift in rubidium-87.

indices of refraction are $n_e = 1.55$ and $n_o = 1.66$ so a small misalignment produces significant path length differences, and coupling to higher order modes. Adjusting the tip and tilt of the crystal allowed the number of transmission peaks to be reduced, leaving a smaller number of higher amplitude peaks. Off-axis birefringence makes it difficult to determine which peak represents the on-axis fundamental mode. Applying a slow voltage ramp to the crystal is helpful here and a triangle wave at 0.2 Hz from 0 to the half-wave voltage was used to aid coarse alignment. In higher finesse cavities slower ramps would be required. Steps should be taken to avoid the sustained application of high voltage beyond the minimum required for alignment as this can damage the crystal [120].

The voltage ramp will show the relative amplitude of the peaks changing with applied voltage. This is caused by incorrect input polarisation or incorrect tip-tilt. The Pockels cell acts as as a voltage controlled waveplate changing the polarisation of light not aligned with the principle axes and therefore varying the amplitude on any polarisation dependant detector. If both polarisations are monitored independently and simultaneously then the sum of the two intensities will be conserved but their relative amplitudes will vary. Incorrect tip-tilt causes the beam to experience the strong off axis birefringence which also varies with applied voltage. The angle of refraction when exiting the crystal will vary with the applied voltage when it is away from the normal, varying the round trip loss of a given cavity mode and causing the relative amplitudes of peaks to vary. Small adjustments should be made in tip and tilt until a single peak is sustained for the full range of voltages; this is fine tuned to maintain a constant amplitude. In practice, iteration between tip, tilt, and roll (input polarisation) is needed to optimise alignment.

Once the transmission spectra shows peaks of almost constant amplitude translating with voltage, and perhaps some small secondary peaks appearing at times, the cell is close to full alignment. Fine tuning requires adjustment of cavity mirror-1 which should be adjusted to maximise coupling efficiency, and also to reduce the appearance of other peaks. If the crystal or protective windows are wedged then transmission through the cell may induce a small tilt in the propagation direction; adjustment of the end mirror will compensate for this. Some iteration between this end mirror and the tip-tilt of the Pockels cell will yield best results. Final tweaks to the mode-matching mirrors (6 and 8) are required to maximise coupling to the fundamental and reduce coupling to higher order modes.

APPENDIX B

ATOMIC STRUCTURE OF RUBIDIUM

The following two figures show the relevant energy levels of rubidium 87 and the transitions addressed by each of the laser beams in the high bandwidth interferometer described in chapter 3. The polarisation state of the lasers is also shown.

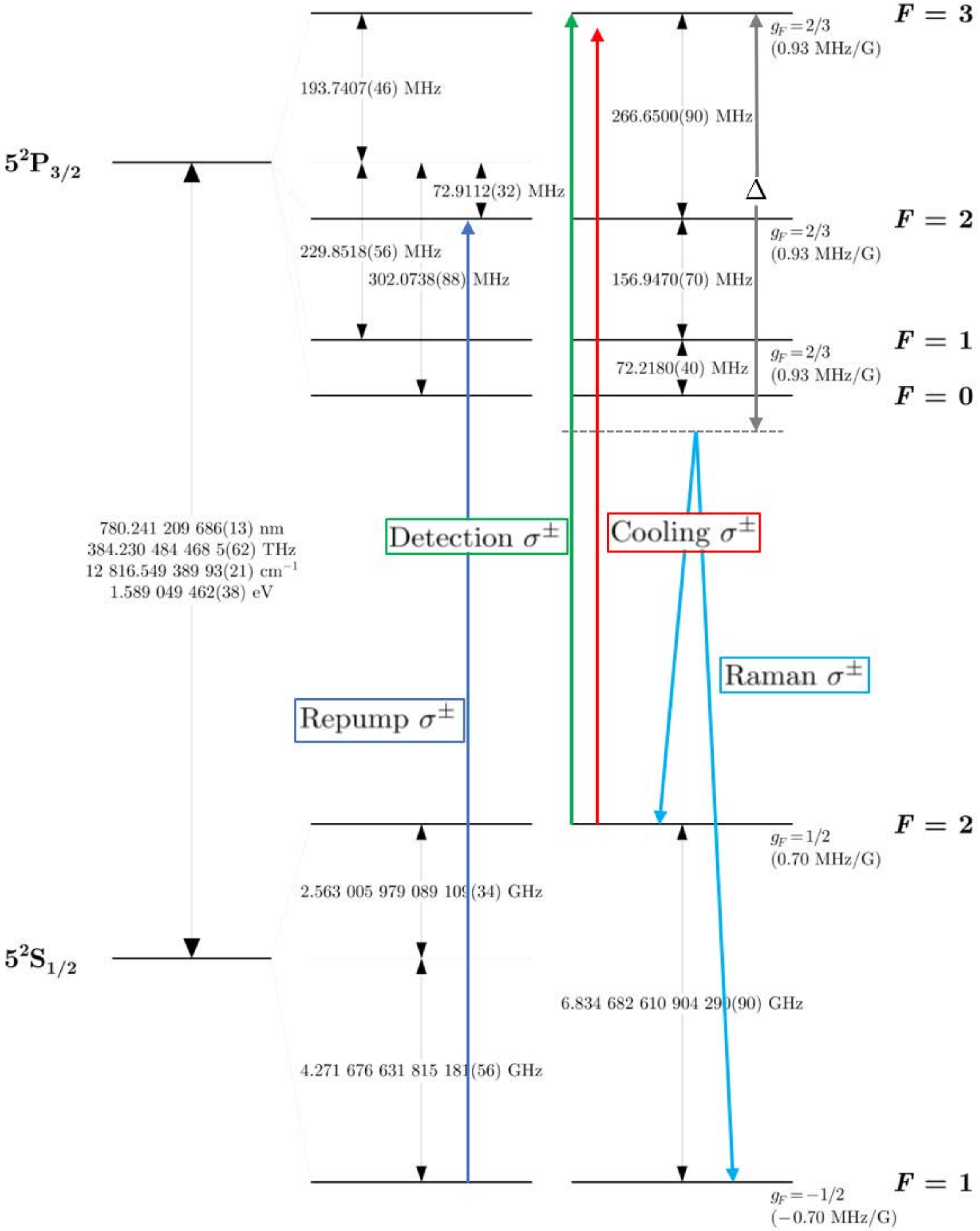

Figure B.1: Rubidium 87 D_2 transition hyperfine structure, with the transitions addressed by the lasers in the highbandwidth system indicated. The polarisations of the lasers are indicated in their labels. Where two polarisations are indicated e.g. $\sigma^{\pm}$, the atoms see light in both polarisations from different beams operating at the indicated frequency. Diagram adapted from Steck [121].

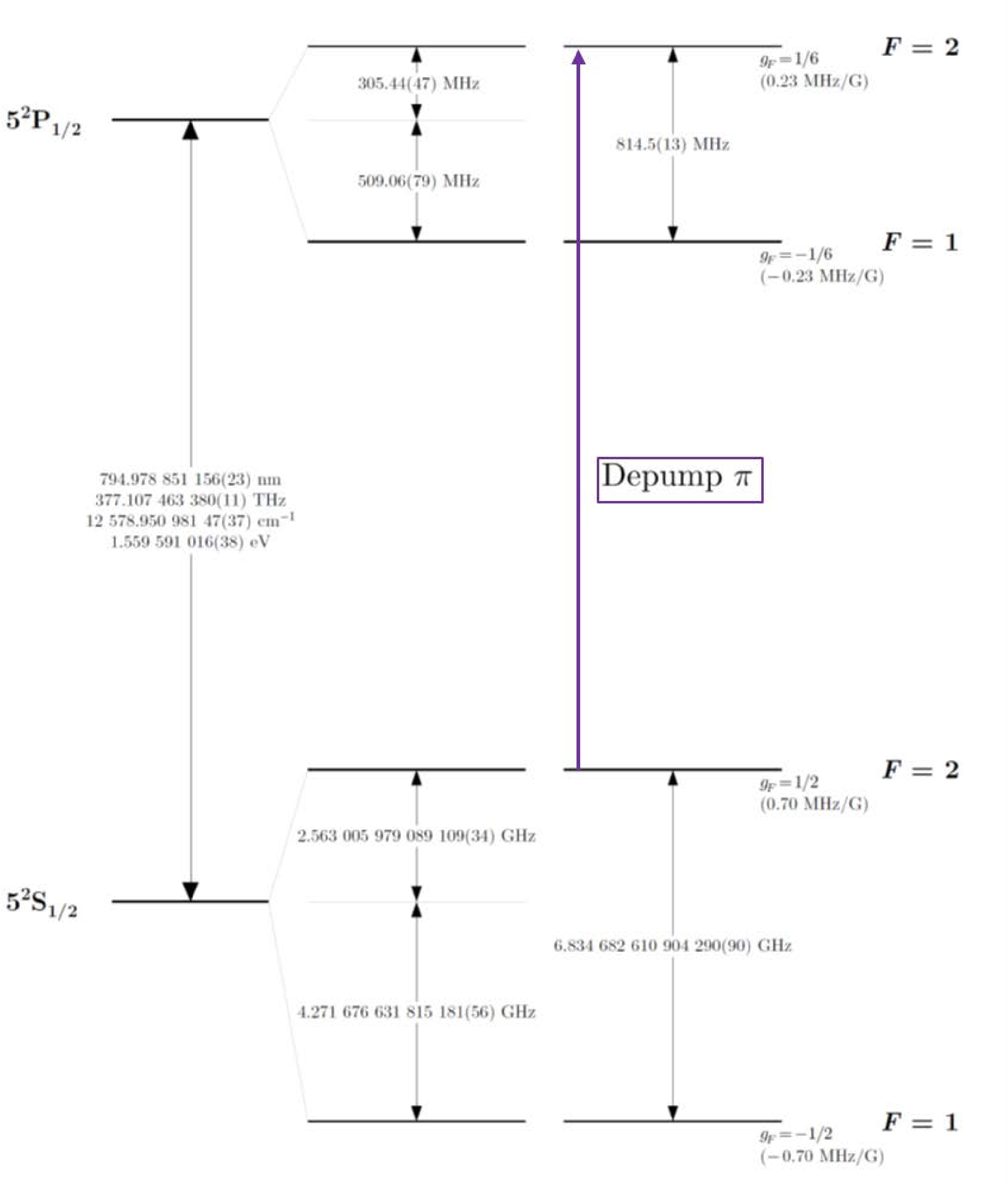

Figure B.2: Rubidium 87 D_1 transition hyperfine structure, with the depump laser indicated by the arrow. The depump laser is π-polarised. The $|F = 2, m_F = 0\rangle$ sublevel is dark to this laser. As a result atoms are shelved to this level during optical pumping. Diagram adapted from Steck [121].

APPENDIX C

SYSTEM DESIGN

The following section describes the key components in the high bandwidth sensor head from chapter 3. We focus on those features that enable high bandwidth operation.

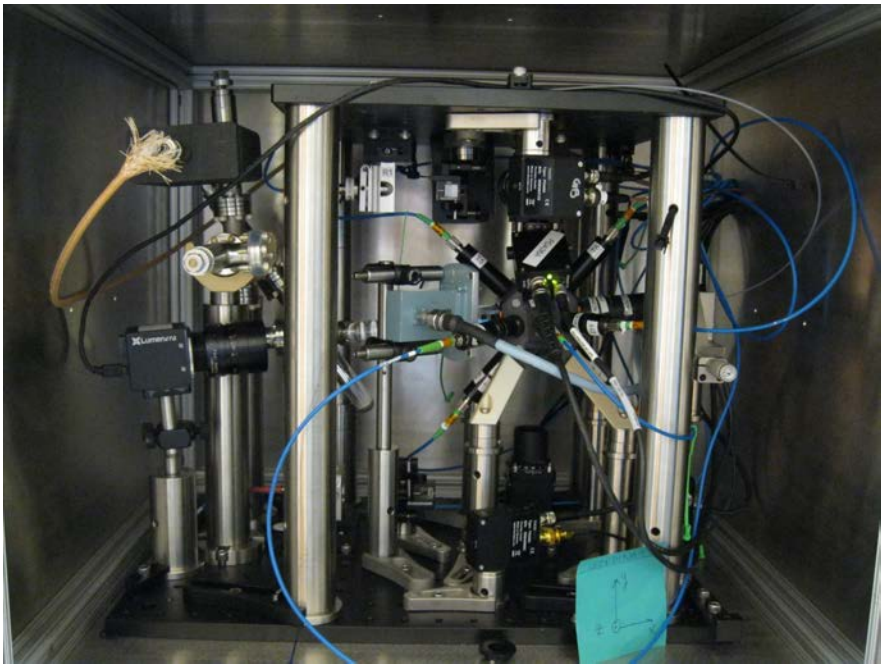

Figure C.1: This photo shows the entire sensor head inside its magnetic shield.

C.1 Vacuum

The experiment is conducted under vacuum in a quartz cell connected to standard CF16 vacuum components. The cell is AR coated at 780nm and is tilted by 5 degrees from horizontal to prevent the formation of fringes in the vertical Raman beams. These spatial fringes would vary the Rabi frequency across the atom cloud and cause a significant reduction in interferometer contrast.

The vacuum is maintained by an ion pump holding a base pressure of 10^{-8} mBar. Our high-bandwidth scheme allows us to tolerate much higher background pressures than a typical experiment running at T-times of 100 ms. We load directly from room temperature rubidium vapour removing the need for complex differential pumping stages or oven based dispensers. Rubidium was introduced to the experiment with an ampoule isolated from the main vacuum with a valve and heating tape was used to drive rubidium into the experiment cell. Whilst background Rb vapour allows efficient MOT loading, temperature control (implemented with a peltier cooler) allows the vapour pressure at the MOT to be precisely adjusted. Rakholia used this method to optimise the balance between recapture efficiency and loading rate; it is likely that we would also benefit [122].

C.2 Optomechanical and Magnetic Assembly

The optomechanical and magnetic assembly is a frame machined from G10 (a fibreglass epoxy) supporting almost all of the beam delivery optics and magnetic field coils. The Raman beams are carried to the sensor head from the laser breadboard through two separate fibres and are delivered to the atoms by optics mounted directly to plates above and below the vacuum cell. The frame itself is mounted directly over the quartz cell with approximately 2 mm clearance on each side. It is positioned on 3D printed legs of differing lengths in order to achieve the 5 degree tilt. These legs are bolted to standard 1" optics post, which are in turn mounted to the baseplate breadboard. The entire assembly is placed inside a mu-metal shield which helps to reduce the effect of stray fields on the interferometer.

C.3 Optical Delivery

Laser beams are delivered to the sensor through optical fibres. These beams must then be aligned, correctly polarised, and collimated before they can be used. We achieve all of these functions with this optomechanical frame. The frame features 16 optical ports 14 of which are tapped to allow 1/2" lens tubes to be screwed on directly (not all of these ports are currently in use). The position and orientation of these holes was designed such that the beams would overlap at the experiment centre, and were constructed precisely enough that no further alignment was required.

The six MOT beams are delivered to the experiment in fibre and pass through a 1/2" lens tube (2" in length) containing a $\lambda/4$ plate to produce the circular polarisation. The beams are not collimated and we rely on the natural divergence from the fibre to produce sufficiently large MOT beams [123]. The repump beam is collimated and circularly polarised using a lens in addition to a $\lambda/4$ plate. The D1 depump light is also collimated and has a linear polarisation set to match the magnetic quantisation axis. The detection beams are delivered to the experiment through two opposing 1/2" lens tubes in which they are collimated and circularly polarised. The stringent requirements of Raman beam alignment did not allow us to use this approach; instead Raman delivery was achieved with separate optomechanics described below.

C.3.1 Raman

The Raman delivery system was achieved using COTS[1] components. Fixed package fibre collimators[2] are mounted inside flexure mounts[3] on top of a 1D translation stage[4], providing 3 of the required 4 degrees of freedom. The beam passes through a Glan-Taylor polariser[5] to provide polarisation purity of at least 100000:1. A cube mounted gold-mirror[6] and $\lambda/4$ plate direct the light onto the atoms. The mirror-cube is mounted on an additional 1D translation stage, providing the final degree of freedom needed for arbitrary Raman beam steering.

C.3.2 Magnetic Fields

The G10 structure supports the coils used to produce the quadrupole and three bias fields needed to generate a MOT. The coils were made from bondable magnet wire[7], which was wound onto 3D printed forms and then cured at 200° for 30 minutes. The resulting rigid coils were then slid into the corresponding groves in the optomechanical frame, and adhered with a small amount of epoxy. Tight grove tolerances ensure the coils are centred with respect to the cooling beams. Placing the coils close to the vacuum chamber made it possible to generate the required fields and gradients with much smaller coils, drawing less power, offering lower inductance, and allowing much faster switching times than can be achieved with a standard design. The use of G10 and an all glass vacuum cell was mandated by the need to prevent the formation of eddy currents. Lenz's law states that these induced currents act to oppose the change in magnetic field, making it very difficult to switch the B field quickly. This is particularly important in our high bandwidth scheme

---

[1] Commercial Off the Shelf

[2] μLS: FC10-NIR1 $1/e^2$ diameter 5.5mm

[3] Siskiyou: IXF1.0a with IXF1.75mb

[4] Newport: DS40-X on B-2B

[5] Thorlabs: GT10-B

[6] CCM1-M01

[7] MWS, 25AWG, Heavy, Polyester Coated

as even a 1ms increase in switching time would reduce our bandwidth by 9%. The effect of stray magnetic fields on the interferometer was further reduced by placing the entire assembly within a mu-metal shield.

APPENDIX D

LASER SYSTEMS

D.1 Overview

The laser systems are the backbone of any light pulse atom interferometer. We use lasers to cool the atoms, generate a MOT, sub-Doppler cool, generate interferometry pulses, and detect the state of the atoms. The systems employed in the high bandwidth interferometer and their performance figures are discussed in the following appendix. Specific product references are for the purpose of clarification only and are not an endorsement by the author.

D.2 Second Harmonic Generation

The light for the Raman system is generated by frequency doubling the output of a fibre laser and amplifier at 1560nm. This offers a narrower line width than an equivalent ECDL (External Cavity Diode Laser) and has the potential for providing very large amounts of power. The fibre-laser seed is supplied by NP Photonics Rock module operating at 1560nm.[2] The Raman system uses an IPG Photonics fibre amplifier[3] generating 32W at 1560nm. Frequency doubling is achieved in a periodically poled lithium niobate crystal supplied by Covesion[4] temperature stabilised to $\pm 0.01^\circ$. A similar system was demonstrated by Sané et al [70]. The redesigned cooling system will use an 11W fibre amplifier[5] and SHG as cooling is less power intensive.

---

[2] NP Photonics: Rock Module, 50mW, linewidth < 3 kHz, Frequency range > 100 GHz, and modulation facility

[3] IPG Photonics: EAR-30k-C-LP-SF

[4] Covesion: PPLN MSHG1550-1.0-40 in a PV40 Oven with OC2 temperature controller

[5] IPG Photonics: EAR-10k-C-LP-SF

D.2.1 PPLN Mode Matching Theory

Maximising the efficiency of second harmonic generation requires optimised input beam parameters and careful alignment. In the following section we calculate these optimum parameters. Boyd and Kleinman [124] demonstrated that the maximum conversion efficiency is achieved when the ratio of crystal length to confocal parameter is 2.84. This fixes the relationship between the diameter of the incoming beam D, the focal length of the coupling lens f, and the length of the crystal l.

$$b = \frac{l}{2\mathcal{R}} = 2.84 \tag{D.1}$$

As we begin with a collimated beam, we select the appropriate lens to give us the required Rayleigh range $\mathcal{R}$.

The diameter of a beam at its focal point is: [125]

$$d_0 = \frac{4\lambda}{\pi}\left(\frac{f}{D}\right) \tag{D.2}$$

Where f is the focal length of the lens and D is the diameter of the collimated incoming beam. The Rayleigh range at the focus of a lens is:

$$\mathcal{R} = \frac{\pi d_0^2}{4\lambda} = \frac{4\lambda}{\pi}\left(\frac{f}{D}\right)^2 \tag{D.3}$$

Hence:

$$f = \sqrt{\frac{l\pi D^2}{22.72\lambda}} \tag{D.4}$$

For the Raman system $D = 1.1$ mm, $l = 40$ mm, and $\lambda = 1560$ nm; giving an optimum focal length of 65.4 mm. The closest available lens has a focal length of 60 mm yielding $l/2\mathcal{R} = 3.38$. The cooling system amplifier has a slightly larger beam diameter $D = 1.2$ mm; giving an optimum focal length of 71.5 mm. The closest available lens has a 75 mm focal length yielding $l/2\mathcal{R} = 2.58$.

D.2.2 Alignment

Aligning a free space frequency doubling system provided some unique challenges. SHG efficiency scales with input power squared making low power alignment impossible. The initial temperature was set based on the manufacturers data and coarse alignment was achieved by observing the crystal output beam profile on a silicon based CCD. Initially I optimised the input beam direction to generate a Gaussian output mode. The alignment was further optimised by maximising the conversion efficiency as measured on a silicon power meter. The crystal was then temperature tuned with optimisation requiring temperature adjustments at the 0.05 K level. Silicon detectors were used for measuring SHG output as they are completely blind to light at 1560 nm and cannot mistake pump light leaking thought the dichroic filter for SHG. GaAs based detectors (including most IR power meters) are particularly prone to this. These detectors are more sensitive to photons at 1560 nm than 780 nm so even a small amount of pump leakage can dominate an SHG signal.

Due to the significant pump powers involved, I monitored the transmission efficiency of the crystal with a wavelength insensitive thermal sensor as pump power was gradually increased. A reduction in transmission efficiency would have indicated a potentially catastrophic heating. Even at 95% transmission efficiency, the local crystal heating by the pump beam was significant. The crystal setpoint temperature was reduced from 81.2°C to 78.85°C to compensate for the local heating caused by the 32 W of pump power.

To reduce wavefront distortion, the SHG beam is collimated before passing through the filtering dichroic mirror[1]. The collimating lens, (coated for 780nm) produced a powerful back-reflection in 1560 nm which at full pump power was several watts. To prevent damage to the crystal-oven a beam block was constructed from anodised aluminium with a very narrow central aperture, allowing the crystal output to pass but absorbing most of the diverging back-reflected 1560nm.

D.2.3 Green Light

At pump powers above 15W green light became visible (see figure D.1). This light is generated through 4-wave mixing, a non-linear process coupling 3 photons at 1560 nm and producing one at 520 nm. The amounts of power are small, but as neither the eye protection nor the optics are coated for this wavelength these spots are visible and provided a useful check (through the use of back reflections) that the optics were aligned correctly.

D.2.4 Performance

The critical performance characteristics of a frequency doubling system are the maximum output power, and doubling efficiency. Measuring these quantities at such high beam powers is not entirely straightforward. The damage threshold of our power meter was ∼6 W in a 1mm beam and both the input and output beams exceed this. For the pump beam we overcame this by using the indicated output power given by the amplifier

---

[1] Thorlabs: DMSP1000, shortpass cut-off $\lambda = 1000$ nm

Figure D.1: The green spots are caused by 4-wave mixing within the PPLN doubling crystal, the are visible on the crystal output facet (top left) and on the beam block after a back reflection from the collimating lenses.

itself, this was not always reliable and exhibited hysteresis and clear misreads. These misreads are the source of the vertically stacked points in figure D.2. The output was measured with a thermal power meter[1] and these 'direct' measurements are plotted in figure D.2 in magenta. The highest output powers exceeded the detector damage threshold so 'corrected' data was taken in which a PBS $\lambda/2$ pair attenuated the power to 39.1% before measurement. This factor was reapplied to the values before plotting the 'corrected' data in blue.

The fit in figure D.2 only includes the corrected data series, the direct data is only shown to verify the correction. Equation D.5 gives the result of this fit, showing a conversion efficiency of 0.967% per Watt. It also calculates that 2.5% of the 1560nm, pump light reaches the sensor (consistent with the specifications of the dichroic mirror).

$$\mathrm{P}_{780} = 9.67 \times 10^{-3}(\mathrm{P}_{1560})^2 + 0.0254(\mathrm{P}_{1560})\,\mathrm{Watts} \tag{D.5}$$

The maximum output power was measured to be 12.0W. The 9.9W measurement was taken with the pump set to 89% system power despite indicating 32.5W output, suggesting that this was an overestimate

---

[1] Thorlabs: S310C

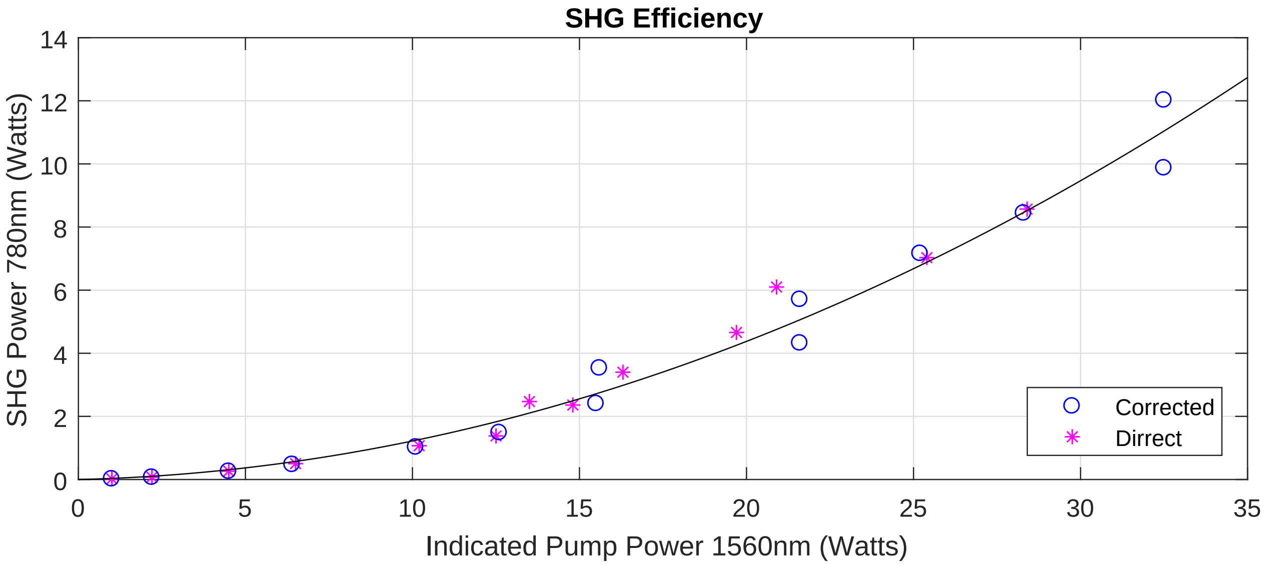

Figure D.2: The SHG output is plotted against indicated pump power. The fit only includes the corrected data.

of pump power at that time. This conversion efficiency is almost identical to the 36% claimed by Sané et al. and our higher output power is due to a slightly more powerful amplifier [70].

D.3 Raman System

The Raman system is required to produce two counterpropagating, orthogonally polarised beams, split by 6.8GHz, with common beam switching, and a fixed phase relationship at the atoms. Figure D.3 shows the beam path used to generate the Raman beams. We generate up to 12 W of 780 nm with SHG in a PPLN crystal. A beam sampler[1] diverts ∼1% of power to a fibre for frequency and sideband monitoring. The majority of the light passes through the common mode (COM) AOM which is used to switch both beams, controlling the pulse duration. The light is then split by a PBS (polarising beamsplitter) and $\lambda/2$ plate to allow precise the control of the power balancing. Both paths go through an additional PBS (polarising beamsplitter) and a half wave plate prior to fibre coupling. This allows the polarisation of the light to optimally matched to the PM fibre, minimising temperature and stress induced polarisation fluctuations, and subsequent power fluctuations on the atoms.

The 6.8GHz splitting is generated by modulating the 1560 nm pump light with a fibre-EOM at 6.8 GHz. Applying second harmonic generation (SHG) to a modulated source doubles the modulation depth but leaves the modulation frequency unchanged. Without further frequency manipulation, the combination of

---

[1] Newport: 10Q40NC.2

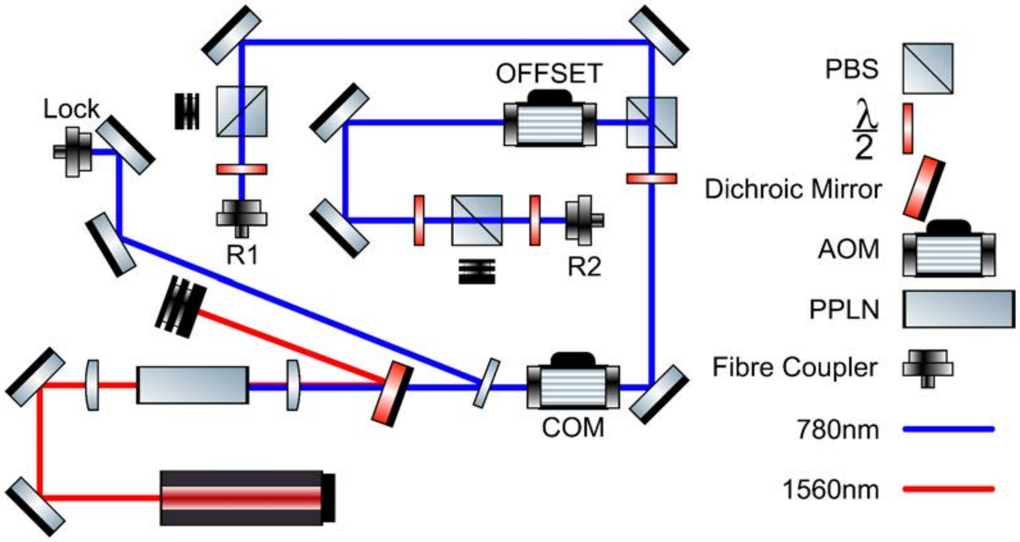

Figure D.3: The above beam path shows the set up used to generate and stabilise the Raman beams. Frequency doubling is followed by an AOM network and three fibre outputs. The Raman beams (R1 and R2) are delivered directly to the atoms. The Lock output is monitored on a wavemeter and Fabry-Pérot. [84]

R1 and R2 (the two Raman fibre outputs, see figure D.3) would provide multiple valid pairs of Raman beams imparting momentum in both directions leading to at least two simultaneous interferometers. To prevent this we drive the EOM 74 MHz blue of the 6.8 GHz hyperfine splitting, and compensate the additional frequency shift with an AOM (OFFSET) in the R2 beam path. This ensures that only pairs of counterpropagating beams with a single $\mathbf{k}_{eff}$ match the frequency condition, removing the simultaneous interferometry problem.

If Doppler free Raman beams are desired, we use a single fibre to deliver both beams (blocking the unwanted fibre input) and remove the additional 74 MHz EOM shift. The OFFSET AOM is not a problem in this case as it applies an equal frequency shift to both beams and simply increases the single-photon detuning Δ.

Due to very high AOM and fibre coupling efficiencies, this system can deliver up to 3.9 W output from each of the two Raman fibres. This power is divided equally between the carrier and two side-bands. Only two of the three lines from each fibre can participate in the interferometer, forming two valid pairs with single-photon detunings Δ differing by the 6.8 GHz hyperfine splitting.

D.4 Raman Beams Generated by Modulation

We generate the frequencies for our Raman beams with an EOM (electro-optic modulator) operating at 1560 nm, the output of which is amplified and frequency doubled. The EOM adds frequency sidebands to a carrier, the relative spacings and amplitudes of which are controlled by the frequency and amplitude of the RF input. These RF signals are controlled to <1 Hz in GHz signals with off-the-shelf components, meeting the system requirements without any custom RF circuit design.

In our system we drive the EOM with RF signals at the atomic Hyperfine splitting (after compensating for AC-stark shifts) and adjust the RF power to make the carrier and 1st sideband powers equal in amplitude as measured at 780 nm. Second harmonic generation (frequency doubling) doubles the modulation depth but leaves the modulation frequency unchanged. We have now generated three laser lines of equal power, separated by the hyperfine splitting ν_{HFS}. This is sufficient to drive Doppler free Raman transitions from a single interferometry beam; see section 3.3.

We deliver all three of these frequencies to the atoms through two fibres (section D). For a Doppler sensitive (gravity sensing) interferometer at high bandwidth this creates a problem. We cannot use the Doppler effect to break symmetry between the Raman beams propagating in opposite directions as its effect is effect is too small in 10 ms of freefall. For the interferometer to function successfully it is vital that each atom takes the same photon from each beam. If we wish our first pulse so cause the atom to recoil upwards, it must absorb an upward going photon and emit a downward going photon. Without breaking this symmetry we will scatter photons in both directions, resulting in at least two simultaneous Doppler sensitive and two Doppler insensitive interferometers. After three interferometry pulses the number of possible paths will obfuscate the output signal.

For our Doppler sensitive (gravity measuring) interferometer we break this symmetry by increasing the splitting between the sidebands by 74 MHz and then passing one of the two Raman beams through an AOM also operating at 74 MHz. This guarantees that only Raman transitions scattering in one direction satisfy the frequency condition, (the 150 MHz two photon detuning δ in the opposite direction make its transition probability negligible).

Even with the AOM, the presence of three frequencies in each beam results in two pairs of beams able to drive an interferometer in the desired direction (differing in Δ by the modulation frequency $\nu_{\mathrm{HFS}} + 74$ MHz).

D.4.1 Phase Lock

The OFFSET AOM can be used to phase lock the two Raman beams. By shifting the frequency of the AOM by δf for a small amount of time τ a phase shift $\delta f \tau$ can be added to that beam. The relative phase of the two beams could be monitored by combining a sample of the two Raman fibre outputs on a photodiode. The photodiode beat note (at ∼6.8 GHz) can be compared with a stable RF reference using an RF mixer or phase detector generating an output proportional to any phase error. An appropriate PID loop fed back to the the AOM's RF input would remove any phase noise occurring before the beams are sampled. As optical phase noise induced by vibrations in the fibres is likely to be a dominant noise source in the interferometer, it is almost certain that a phase lock will be required for optimum instrument performance.

D.5 Cooling and Detection

The cooling system is required to generate 6 beams with at least 3 mW of power, tunable from $\sim 10 \rightarrow 50$ MHz red of the $F = 2 \rightarrow F' = 3$ transition (^{87}Rb D2 line, see B.1). [121] To use the same laser system for detection this tuning range must be extended to include resonance.

The current laser system for cooling and detection is based on an ECDL Master, tapered amplifier, and a set of AOMs. This system was in place before I began working on the project and has operated well in the past [122]. Due to a number of limitations and problems (discussed in the next section) we decided to replace the system. My completed designs are included here along with some expected performance figures. These will be implemented in future refinements.

D.5.1 Existing System

The following laser system was the one used to carry out all of the measurements included in this report. The seed laser is an ECDL, which after passing though optical isolators is fibre coupled. This light is delivered to the board shown in figure D.4. This board splits the light with a PBS. An AOM shifts the frequency of the lock beam by 40 MHz before delivering it to the lock components where the frequency is stabilised through Modulation Transfer Spectroscopy. The other beam traverses a double pass AOM centred on 150 MHz and swept by ±10 MHz and is coupled into the output fibre. This allows us to scan the laser frequency by 300 ± 20 MHz with a parasitic factor of 2 variation in output power.

The output from figure D.4 is delivered to an injection-locked Slave laser and tampered amplifier (shown in figure D.5). The injection-lock is there to smooth out the power variations caused by the Sub-D AOM

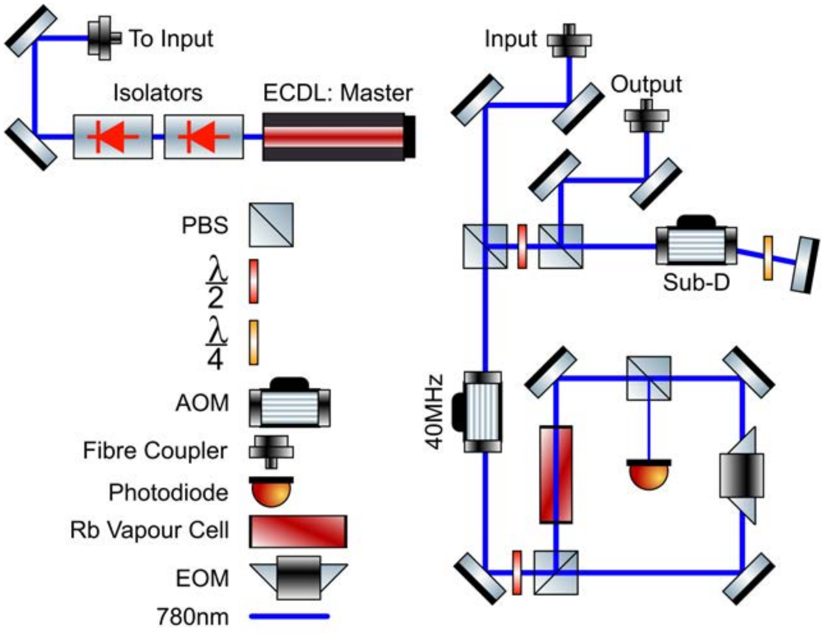

Figure D.4: This beam diagram shows the ECDL seed (top left) and the board used to lock the laser and sweep the frequency for sub-Doppler cooling (right). The output from this board is delivered to the optical amplifiers shown in figure D.5. [84]

and to amplify the power to the 30 mW needed to seed the tapered amplifier. The 500 mW TA output is fibre coupled and delivered to the AOM network described in section D.5.3.

Whilst this system had operated well in the past [122], the Master laser diode's performance has degraded resulting in a reduced mode-hop free region at the required frequency and a resulting reduction in long term lock stability. The injection-lock and TA seeding are both inconsistent resulting in drifts in output power requiring daily realignment. The system is exhibiting frequency noise from an unknown source at a level sufficient to degrade our measurement fidelity. The 500 mW TA output limits our cooling beam power to <5 mW per beam and we should achieve an increase in atom number with more cooling power. For these reasons it was decided that we would upgrade this system.

D.5.2 Upgraded System

The upgraded system (see figure D.6) is based on frequency doubling of 1560 nm analogously to the Raman. The fibre coupling efficiency from the TA was poor at only 30% resulting in less than 200 mW of power delivered to the AOM network. A fibre based amplifier allows much higher coupling efficiencies $\sim$70%, so a

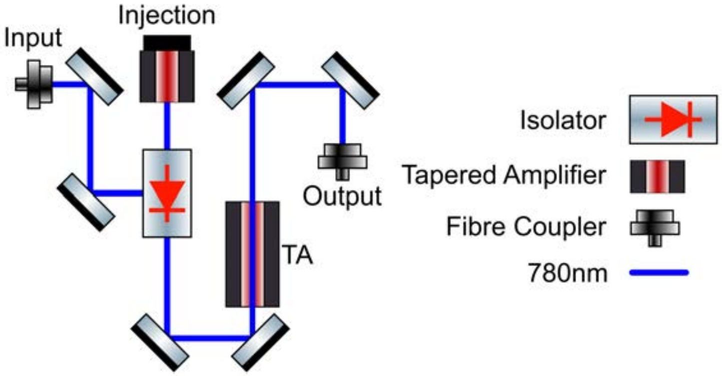

Figure D.5: This is the amplification board in the existing laser system. The 1.5 mW input seeds an injection-locked diode which in turn seeds the tapered amplifier generating 500 mW of output for the AOM network. [84]

large increase in usable power can be gained from only a modest increase in output. We chose an 11 W fibre amplifier (10 W specified) which we expect to generate 1.1 W of 780 nm and deliver 800 mW to the AOM network. This should allow us to deliver cooling beams in excess of 20 mW per beam without any further changes. The lock fibre will deliver ∼1 mW of power to the spectroscopy board described in section D.8.2.

D.5.3 AOM Network

The AOM network is common to both the existing and upgraded laser systems. It splits the input light into 4 output channels and allows them to be switched individually. The power in each channel can be varied by adjusting a series of $\lambda/2$ plates. The switching is achieved with a double passed 80 MHz AOM and the output fibre coupled. The RF used to drive these AOMs is switched with solid state switches triggered by a TTL input from the control system. The RF amplitude for C1 and C2 is adjusted with voltage control attenuators also driven by the control system. This allows precise control of both the timing and amplitude of these beams. This AOM network predates my involvement with the project and other than routine alignment is completely unchanged [122].

The outputs from this network are connected in the following way. C1 and C2 are both connected to in-fibre beamsplitters, producing 4 and 2 outputs respectively. These fibres are connected to the lens tubes attached directly to the optomechanical frame described in chapter C.3. The beams are allowed to freely expand, (passing through a $\lambda/4$ plate within the lens tube) and reaching a diameter of ∼10 mm at the MOT and delivering 3.5 mW per beam. C4 is connected to an in-fibre splitter producing 2 outputs used for detection. These fibres are also connected to lens tubes on the optomechanical frame, but these tubes contain

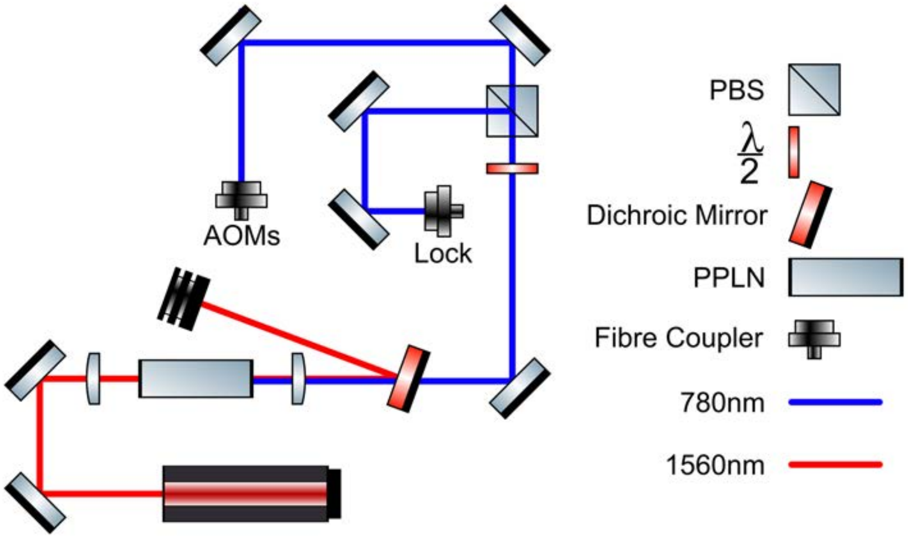

Figure D.6: The setup used to generate and fibre couple the light for cooling and detection in the upgraded system. After frequency doubling the light is split and coupled into two fibres, one for frequency stabilisation, and the other to deliver light to the AOM network. [84]

a lens to collimate the fibre output in addition to the $\lambda/4$ plate. For the detection beams, it is particularly important that both the power and beam diameter are well controlled. C3 is currently unused, but may in future be connected to a photodiode to allow us to monitor the system's output power and frequency. Combined with a MOT signal this would allow us to measure the MOT population on a shot by shot basis.

D.6 Depump Laser

The cooling and detection beams both address the $|F = 2\rangle \rightarrow |F' = 3\rangle$ transition on the D2 line of ^{87}Rb. In order to prepare the atoms into our desired $|F = 2, m_f = 0\rangle$ ground state sublevel we use a π-polarised laser resonant with the $|F = 2\rangle \rightarrow |F' = 2\rangle$ transition in the D1 manifold (see B.2). The $m_F = 0$ ground state is dark to this transition so applying it in parallel with our repump laser (section D.7) results in efficient optical pumping to this state. The efficiency of this optical pumping is analysed in section 3.2. The laser is a Vescent Photonics DBR (distributed Bragg Reflector) locked to the desired transition with a saturated spectroscopy module.[1] Ideally a single AOM would be used to switch the laser output, but the laser is locked to the desired output frequency so we require a second AOM with an equal and opposite frequency shift to

---

[1] Vescent Photonics: Spectroscopy Module

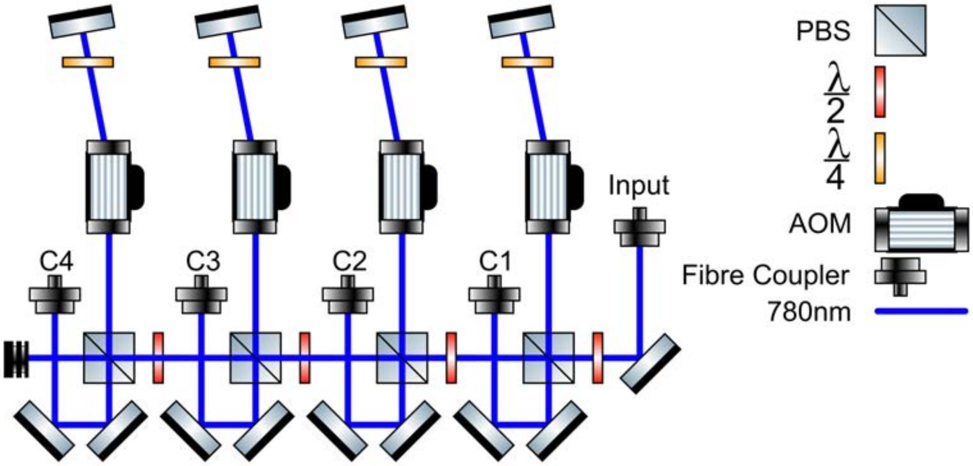

Figure D.7: A schematic of the AOM network described in section D.5.3. [84]

maintain the resonance condition; beam path shown in figure D.8. This system was designed and constructed by Adrian Orozco my fellow PhD student.

D.7 Repump Laser

The cooling transition in ^{87}Rb ($|F = 2\rangle \rightarrow |F' = 3\rangle$ in the D2 manifold) is almost a closed cycling transition, but there is a small probability that the electron falls to the $|F = 1\rangle$ ground state and goes dark. To prevent this we employ the Repump laser resonant with the $|F = 1\rangle \rightarrow |F' = 2\rangle$ transition in the D2 manifold. This repumps population from the dark state and allows both efficient cooling and total population detection to occur. This laser is based on another DFB diode locked through Modulation transfer spectroscopy to a Rb vapour cell. It is switched with a single AOM operating at the frequency required to achieve resonance. As with our other systems pulse duration is controlled through the use of solid state switches in the AOM RF lines, which are in turn driven by TTL channels from the control system.

D.8 Laser Frequency Control

D.8.1 Raman

For the Raman beams, common mode frequency noise will change the single-photon detuning (Δ) which will in turn change the Rabi frequency; see chapter 2. This causes fluctuations in the fidelity of the matter-wave optics, reducing fringe visibility; see figure 2.1. Whilst this can reduce contrast, for large detunings

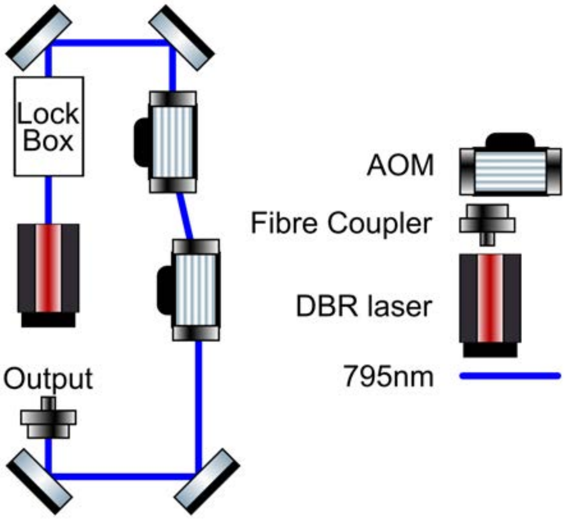

Figure D.8: This is the beam path used to generate, lock and switch the depump light. Designed and constructed by my fellow PhD student Adrian Orozco. [84]

$\Delta > 1$ GHz the passive stability of the seed laser is sufficient to prevent significant reductions. We monitor the frequency with a wavemeter offering ∼100 MHz accuracy which is sufficient for setting a detuning. We also monitor the relative sideband powers with a Fabry-Pérot. Sideband asymmetry is corrected by temperature tuning the PPLN crystal; they are found these to have passive long term stability once balanced. The most important specification in the Raman system is the frequency of the sidebands; fortunately this is controlled by commercial RF components electronics with ∼1 Hz level stability and is not a measurable source of noise in this system.

D.8.2 Cooling and Detection

For our detection system to perform at the atom shot noise limit it must have a frequency variation between the two detection pulses of less than ∼10 kHz. Frequency variation between these pulses will change the amplitude of the signal, giving us noise indistinguishable from phase noise in our interferometry fringes. It was exactly this problem that motivated the design of the upgraded system.

The existing Cooling and Detection laser described in section D.5.1 is locked to a rubidium vapour vapour cell using modulation transfer spectroscopy with feedback on the diode current (beam path shown in figure D.4). The new system will operate with a DFB fibre laser master exhibiting a narrower intrinsic linewidth and better passive stability reducing the demands on the lock servo. It eliminates all but one of the original AOMs removing several potential sources of frequency noise and severe sources of amplitude noise. One AOM per path is still required in the switching network. The removal of these AOMs also eliminates 360 MHz of required frequency shift and the ability to sweep the laser frequency (required for sub-Doppler cooling).

We use modulation transfer spectroscopy of rubidium vapour (see figure D.9) to lock the laser to the $|F = 3\rangle \rightarrow |F' = 4\rangle$ transition on the D2 line of ^{85}Rb with light delivered in fibre from figure D.6 (lock fibre) [121, 126] This lock point is 1.1GHz Blue detuned from the desired $|F = 2\rangle \rightarrow |F' = 3\rangle$ D2 line in ^{87}Rb and 50 MHz further still from the required final frequency for sub-Doppler cooling. To generate this frequency shift and retain the sweep functionality we modulate the incoming light with an fibre-EOM between 966.49 MHz and 1016.49 MHz. The RF for this is supplied by a DDS[1]. The light is spectrally filtered by a temperature stabilised Fabry-Pérot such that only the blue sideband is present in the spectroscopy cell. A polarising beamsplitter (PBS) and a half wave plate ($\lambda/2$) are use to divide the beam into a low power probe, travelling straight through the cell, and a high power pump beam. The pump is modulated by a free-space EOM before counterpropagating through the vapour cell in a path that overlaps with the probe. The probe beam is directed onto a photodiode, where an error signal can be generated with standard RF electronics. A PID controller takes the error signal and feeds back to the laser current closing the loop.

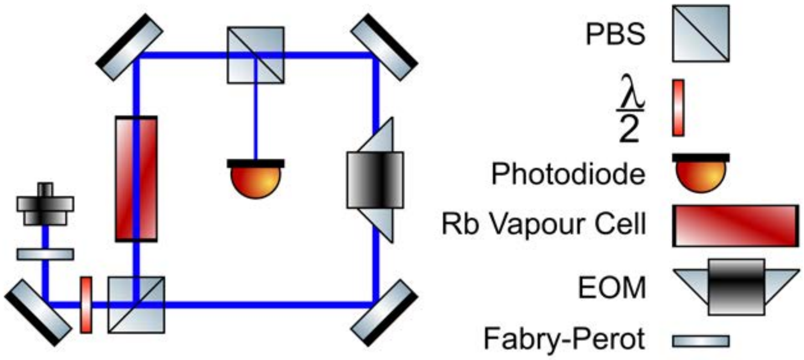

Figure D.9: This is the beam path used to implement Modulation Transfer Spectroscopy in the upgraded system. It is near identical to that used in the existing system with the notable addition of the Fabry-Pérot. [84]

---

[1] Analog Devices: AD9914

APPENDIX E

LASER COOLING AND THE MAGNETO-OPTICAL TRAP

The following section outlines the theory and practical details of the MOT, cooling procedure, and systems as they apply to the high bandwidth interferometer in chapter 3.

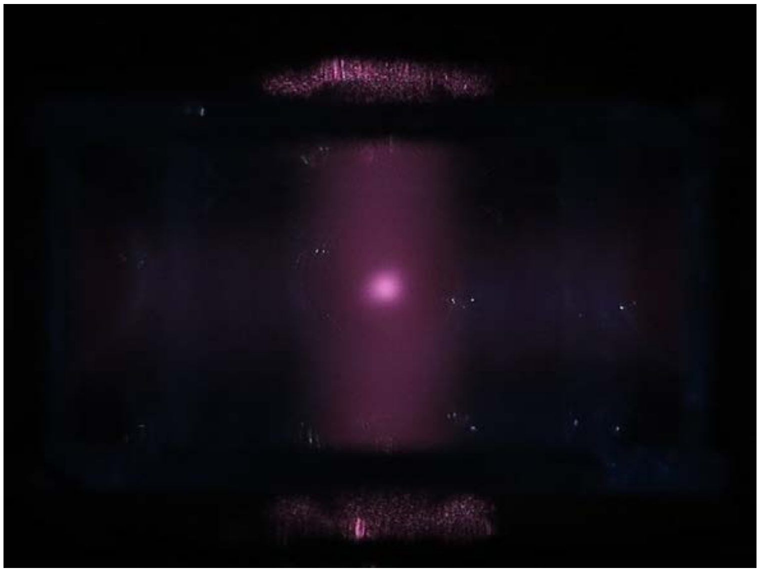

Figure E.1: This is a long exposure photograph of our magneto-optical Trap (MOT). The cooling beams can be seen in the figure as vertical and horizontal red stripes due to fluorescence of the background rubidium vapour.

E.1 Theory

Laser cooling and trapping relies on the ability to exert a controllable force on an atoms with laser light. A careful combination of laser beams and magnetic field gradients act together to cool and confine atoms into a low temperature cloud confined to ∼1 mm^3 . Laser cooling and trapping have been described in excruciating detail by numerous papers and every cold atom thesis since 1990; for additional information the following references provide canonical, early, or particularly instructive explanations [78, 127–131]. I will tackle the problem in two parts, first describing how the interaction between an atom and a laser beam can result in cooling. Secondly I will introduce a magnetic field gradient and explain why this can result in spatial confinement.

E.1.1 Laser Cooling

A photon carries momentum $\mathbf{p} = \hbar\mathbf{k}$. When an atom absorbs a photon, the atom recoils with equal momentum. The atom, now in an excited state will emit a photon in a random direction, causing an equal and opposite atomic recoil. The spontaneous emission occurs in a random direction, so over many scattering events the effect of the spontaneous photons on the atom's momentum average to zero. This approximation of a large number of scattering events is valid, with $\sim 10^3$ photons needed to cool an atom of ^{87}Rb from it's capture velocity of 4 ms^{-1} (corresponding to a temperature of $T = 0.2$ K) to base temperatures of ~ 100 μK. It is interesting to note that only the coldest atoms in the Maxwell-Boltzmann distribution are travelling slowly enough to be addressed by laser cooling.

To turn this momentum transfer into a cooling process it must be velocity dependant. We achieve this with the Doppler effect. By operating the laser at a frequency ~ 10 MHz below resonance (red detuned) we ensure that only atoms with a velocity component directed towards the laser beam are able to absorb photons and be cooled. When this velocity component vanishes no further recoil events can occur. As the initial velocity of the atoms is unknown we require cooling in both directions for all 3 spatial dimensions. We achieve this with 6 counter propagating beams, although systems can function with as few as four [132].

There are several limits that apply to the base temperatures achievable with these processes. The minimum temperature that can be conceived of with discrete $\hbar\mathbf{k}$ photon momentum kicks is the temperature at which an additional scattering event raises the temperature of the atom (known as the recoil limit). For ^{87}Rb this is 361.96 nK [121]. This is the lowest temperature theoretically achievable with laser cooling.

Unfortunately this temperature is not achievable with the cooling procedure described above. At sufficiently low temperatures the spontaneous emission, whilst still satisfying $\langle v \rangle = 0$, causes the atoms to undergo a random walk $\langle v^2 \rangle \neq 0$. This random walk has an associated kinetic energy, which with optimum trapping parameters corresponds a minimum temperature $T_D = \frac{\hbar\Gamma}{2k_B}$. This is known as the Doppler temperature and for ^{87}Rb is 145.57 μK [121].

We are able to beat this temperature with sub-Doppler cooling processes. Polarisation gradient cooling allows us to reach a temperature of 11 μK, with temperatures as low as 2.5 μK demonstrated elsewhere [81]. PG cooling is achieved by removing the quadrupole field whilst simultaneously red-detuning the cooling lasers and reducing the intensity. We sweep the frequency from 10 $\rightarrow$ 50 MHz red of the cooling transition whilst reducing the intensity to 0 over 1 ms. A detailed description of polarisation gradient cooling can be found in *Laser Cooling and Trapping* by Metcalf and Straten [78].

E.1.2 Magneto-Optical Trapping

The processes described above cools atoms within the region of space in which the beams overlap, but does not provide any trapping. Laser cooling on it's own is a viscous damping process with a non-zero $\langle v^2 \rangle$ (this is commonly known as optical molasses after the damping effect experienced by an object moving through treacle). This does provide an increase in density proportional to the cube of the velocity reduction ratio.

We desire much higher atom numbers and more importantly densities for our interferometer. We achieve this by applying a magnetic field gradient across the beam overlap region. This gradient Zeeman shifts the magnetically sensitive $m = \pm 1$ sub-levels by an amount proportional to the distance to the magnetic field null. The correct choice of cooling beam polarisations ensures that a cold atom moving away from the field null is brought onto resonance of the red-detuned beam with $\mathbf{k}$ directed back towards trap centre. Adding this spatially varying confinement force on top of the viscous damping generated by the molasses results in a dense cold cloud of atoms at the magnetic null. This is a magneto-optical trap (MOT). Figure E.2 illustrates the spatial dependence on transition frequency for an atom moving within a MOT.

E.2 Experimental Realisation

We generate our MOT and implement sub-Doppler cooling with the apparatus described in appendix C.3, but in summary it consists of 6 counterpropagating beams within a quadrupole field. The beams freely expand from fibres through $\lambda/4$ plates to generate the correct polarisations [133]. Each beam carries 3.5 mW of power and at the trap centre is 10 mm in diameter. The quadrupole coils are set up in the anti-Helmholtz configuration with 50 turns per coil, each turn being a square 24 mm × 24 mm. At 2 A operating current they generate a field gradient of 9 Gauss/cm at the trap centre. The original quadrupole coils were larger and had fewer turns, but due to a dimensional asymmetry produced a highly asymmetric MOT, shown on the left of figure E.3. Whilst this 'cigar' shaped MOT (aspect ratio ~5:1) may prove to be a very efficient way to load an atom guide, for our present experiment it is inconvenient [134–138]. The new square coils

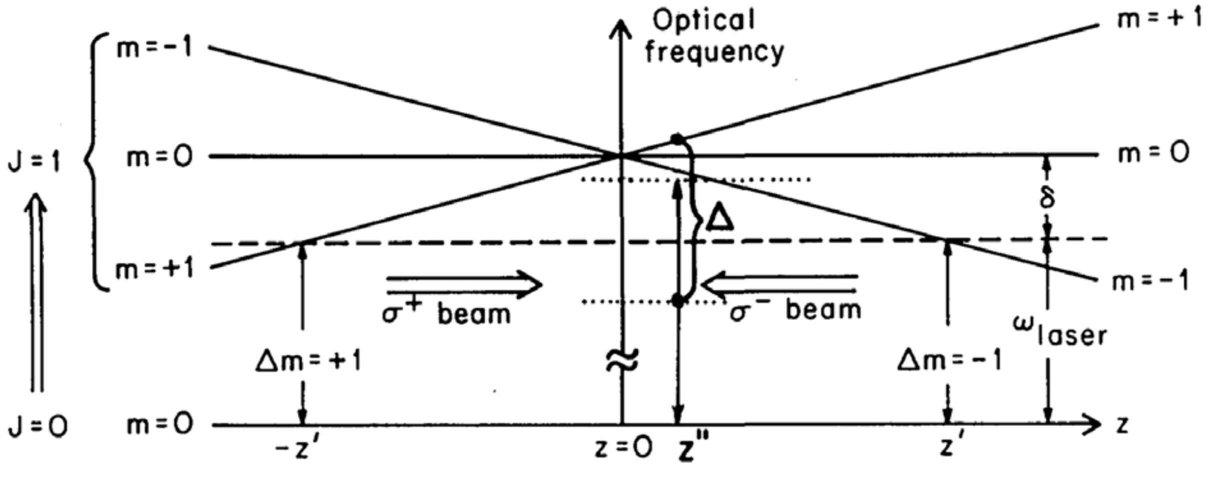

Figure E.2: Arrangement for a MOT. The horizontal dashed line represents the laser frequency seen by an atom at rest, and the two shorter dotted lines represent the frequencies of the opposing laser beams seen by a moving atom. At $z = z''$ an atom moving to the right sees the σ^+ beam detuned by Δ, but the σ^- beam is almost resonant with the transition to $m = -1$. This diagram was taken from reference [131].

generated the much rounder MOT shown on the right of figure E.3. The axial profiles of both MOTs were near identical with an end on view of the new MOT shown in figure E.4. The critical properties of any cold atom source are its atom number and temperature. These are discussed in the following section.

E.3 Performance

E.3.1 Atom Number

We measure the atom number by observing the fluorescence of an illuminated atomic cloud on a photodiode[1]. The relevant atom number for interferometry is that observed during an interferometry cycle, is generally lower than the steady state value because the MOT loading time restricted. The scattering rate per atom is given by:

$$R_{sc} = \left(\frac{\Gamma}{2}\right) \frac{(I/I_{sat})}{1 + (I/I_{sat}) + (2\Delta/\Gamma)^2} \tag{E.1}$$

Where Γ is the excited state lifetime, I is the intensity of the incident Radiation, I_{sat} is the saturation intensity, and Δ is the detuning measured in radians. The saturation intensity is a property of the atomic transition and is in general dependant on the polarisation of the light. The derivation of this formula and a

---

[1] Thorlabs PDA36A with gain at 70dB

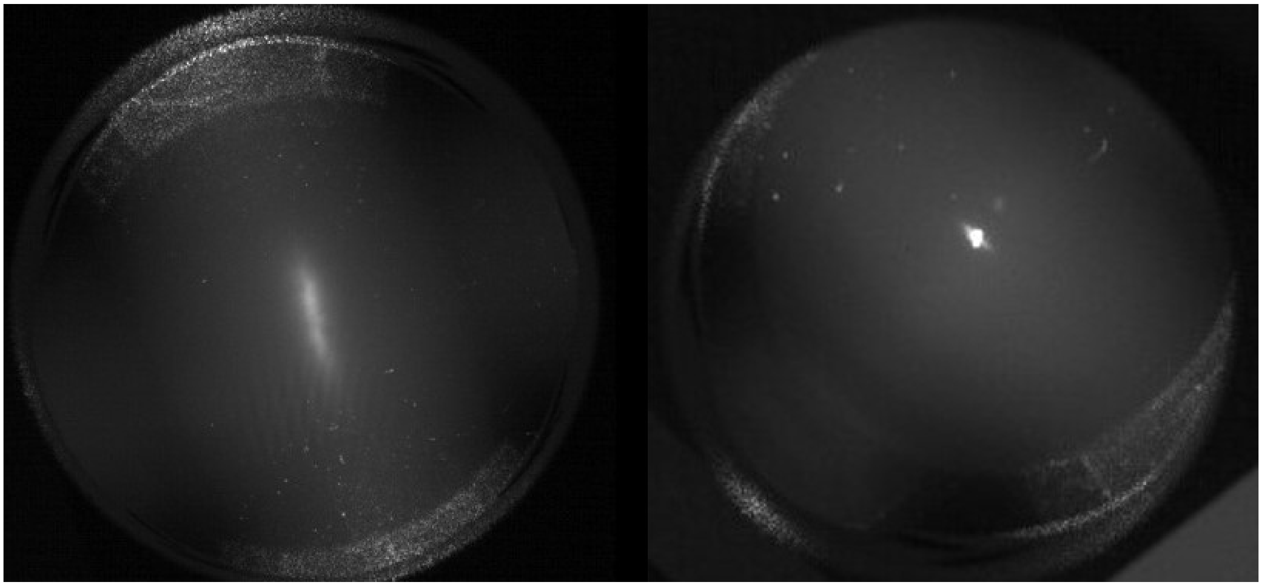

Figure E.3: The left photo is a plan view of the original MOT, the asymmetric ∼5:1 shape is caused by a 2:1 aspect ratio in the quadrupole coils. The new MOT is shown on the right. Utilising square quadrupole coils we were able to generate a far more rotationally symmetric MOT.

discussion of the approximations involved can be found in Steck ^{87}Rb Line Data [121].

The detection beams are collimated, σ-polarised, counter propagating beams and as such their scattering rate can be simply calculated allowing an accurate determination of atom number. The beam diameter is 4.5 mm, with 500 μW per beam.

For a 25 ms cycle and a 2 ms freefall (i.e MOT loading for 21 ms per cycle) we observe a steady state atom number of 1.2×10^7. For a 25 ms cycle and a 7.5 ms freefall (i.e MOT loading for 15.5 ms per cycle) we observe a steady state population of 5.1×10^6. The difference is due to a reduced loading time per cycle. With optimisation of the MOT parameters the recapture efficiency should be increased resulting in a higher steady state atom population. Rakholia et al. demonstrate 86% recapture efficiencies in an interferometer operating with a 20 ms cycle time [76].

Our observed atom number of 1.2×10^7 appears to be low for 10 mm cooling beams with an expectation of 10^8 atoms [139]. This may have a number of causes. The measurement underestimates the population that would result from continuous cooling. It was taken after both sub-Doppler cooling and optical pumping had occurred, which could result in some loss. Our experiment would benefit from increased optical power in the cooling beams, $I/I_{sat} = 15$ compared to 108 in a similar experiment by McGuinness [80]. These errors can be addressed and should result in a larger atom numbers, and a more reliable system.

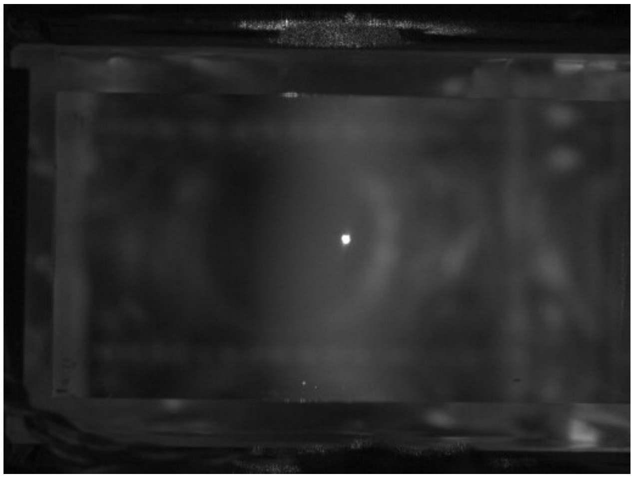

Figure E.4: This is an end on view of the new MOT. This is very similar to the end on view of the original MOT. During regular operation the detection optics are mounted in the location of this camera.

E.3.2 Temperature

In chapter 3.6 we exploit the Doppler sensitive nature of our Raman beams to measure the temperature of our sub-Doppler cooled atom source. We observe a temperature of $T_a = 10.9\ \mu$K. This is above reported temperatures for similar high-bandwidth experiments ($T_a = 5.5\ \mu$K) [80], and well above the 2.5 μK achieved in low-bandwidth experiments [81]. Optimisation of the intensity and frequency ramps during sub-Doppler cooling can improve this temperature. In any case, our short T time makes us far more tolerant of high cloud temperatures than typical $T = 100$ ms experiments.

APPENDIX F

EXPERIMENTAL SEQUENCE

F.1 Timing

The following section considers a single experimental cycle of the high bandwidth interferometer from chapter 3 with emphasis on the relative timings and durations of each event. Figure F.1 is a summary of the entire sequence.

F.1.1 Cooling

The sequence begins with a MOT already loaded into the trap. The MOT coils, cooling, and repump beams remain on unless an experiment is in progress. 70 μs into the sequence polarisation gradient cooling begins. The quadrupole (MOT) coils are switched off reaching zero quadrupole field in $\sim$100 μs. In parallel with this, the cooling beams are swept in frequency from 10 $\rightarrow$ 50 MHz red-detuned and the intensity is attenuated to zero over 1.5 ms. The removal of quadrupole field ends the spatial confinement of the trap and the atomic cloud begins to sag against the remaining cooling light.

F.1.2 Optical Pumping

1.57 ms into the experiment we introduce a bias field to define a quantisation axis for optical pumping. We wait 10 μs for it to switch on and then start the depump beam. After 200 μs optical pumping is complete and we switch off the depump beam, followed 10 μs later by the repump beam (this delay ensures that all the atoms are initialised into $F = 2$). The bias field is rotated to match the quantisation direction of the Raman beams in preparation for interferometry (vertical rather than the 5° tilt required for the optical pumping).

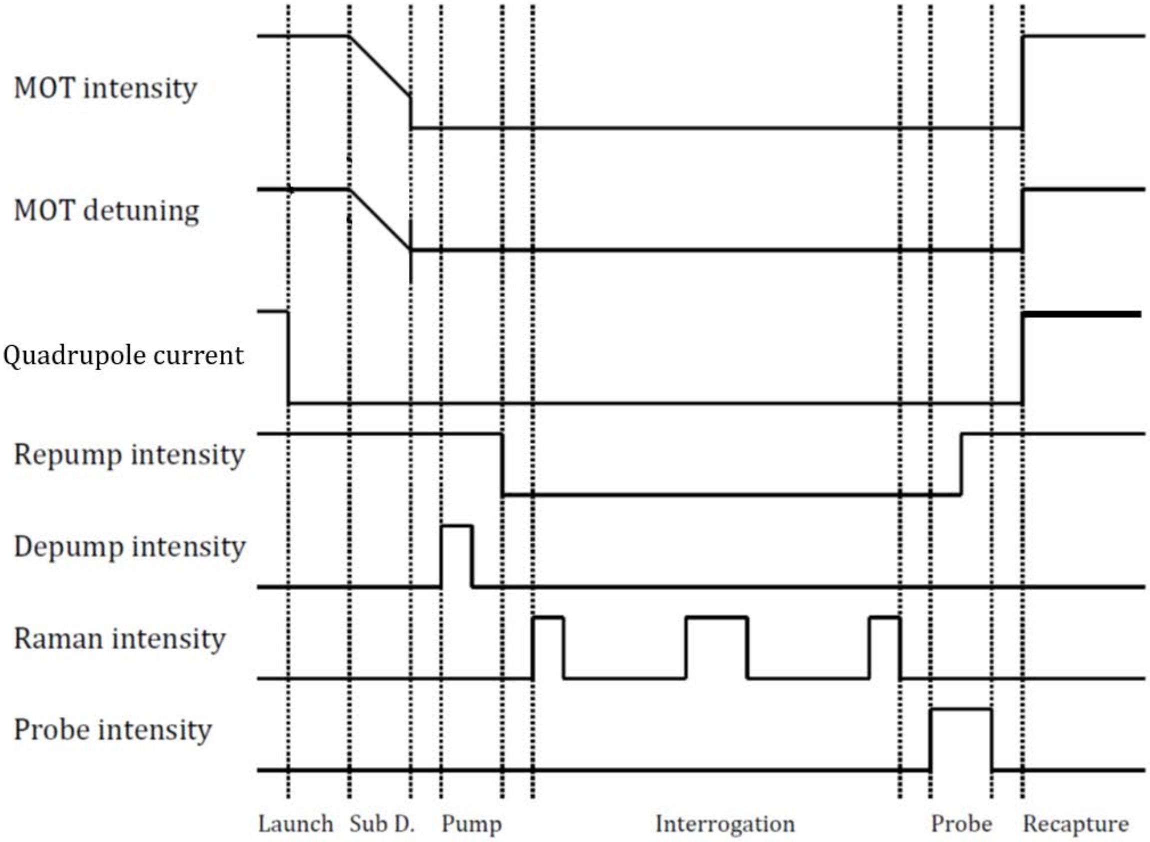

Figure F.1: This diagram shows the timing of key events in the experiment (not to scale). The full experiment duration is approximately 25 ms. This diagram was taken from the PhD thesis by A. Rakholia [122] and modified.

Cooling and optical pumping are complete 1.79 ms into the sequence.

F.1.3 Interferometry

There is a delay of 300 μs before starting interferometry to ensure that the magnetic fields have stabilised. At 2.09 ms we trigger the FPGA, which controls the duration and timing of the Raman pulses. The freefalling cloud is interrogated with three Raman pulses ($\tau_\pi = 8$ μs) separated by T-times $\sim$3 ms. In a typical experiment the atomic cloud has been in freefall for 7 ms and 9.09 ms has elapsed since the start of the cycle. For different experimental parameters this varies from 4 ms to in excess of 12 ms. Once the experiment is fully optimised, still longer interferometry times may yield the highest sensitivity. For the sake of clarity, the typical case with 7 ms of freefall will be assumed.

F.1.4 Detection

With interferometry complete, the quantisation axis is rotated to align with the detection beams by adjusting the bias fields. We switch these coils 10 μs before switching on the detection beam. The detection beams start 9.1 ms after the start of the cycle and $40\mu s$ later we record the atomic florescence with an APD (avalanche photodiode). The additional delay reduces our sensitivity to AOM rise time, and allows additional time for the magnetic fields to stabilise. We record florescence between 9.14 ms and 9.2 ms at which point we start the repump beam. This introduces the $F = 1$ population into the detection cycling transition and allows us to normalise against fluctuations in atom number. We wait another 40 μs before recording florescence for a further 60 μs. Taking the ratio of the two signals (after subtraction of backgrounds) yields the atom probability $P(F = 2)$. The detection sequence is complete at 9.3 ms.

F.1.5 Recapture and Loading

With the experiment complete we restart the cooling beams, repump, and quadrupole coils. This recaptures the majority of the atoms and then continues to load the MOT from background vapour. The experimental control system currently operates a fixed cycle time of 25 ms. In the typical case described above the MOT recapture and loading is allowed to run for 15.7 ms, but this time will vary with the chosen freefall time. This loading time is one of the parameters that will need to be adjusted to realise the maximum experimental performance. Several capture times, and the corresponding atoms numbers are described in appendix E.3.1.

LIST OF REFERENCES

[1] Rustin Nourshargh. A laboratory atom interferometer instrument. Technical report, Sandia National Lab.(SNL-NM), Albuquerque, NM (United States), 2018.

[2] Rustin Nourshargh, Sam Hedges, Mehdi Langlois, Kai Bongs, and Michael Holynski. Doppler compensated cavity for atom interferometry, 2020.

[3] R. Nourshargh, S. Lellouch, S. Hedges, M. Langlois, K. Bongs, and M. Holynski. Circulating pulse cavity enhancement as a method for extreme momentum transfer atom interferometry, 2020.

[4] Kai Bongs, Michael Holynski, Jamie Vovrosh, Philippe Bouyer, Gabriel Condon, Ernst Rasel, Christian Schubert, Wolfgang P Schleich, and Albert Roura. Taking atom interferometric quantum sensors from the laboratory to real-world applications. *Nature Reviews Physics*, pages 1–9, 2019.

[5] Alexander D. Cronin, Jörg Schmiedmayer, and David E. Pritchard. Optics and interferometry with atoms and molecules. *Reviews of Modern Physics*, 81(3):1051–1129, July 2009.

[6] J. M. McGuirk, G. T. Foster, J. B. Fixler, M. J. Snadden, and M. A. Kasevich. Sensitive absolute-gravity gradiometry using atom interferometry. *Physical Review A*, 65(3), February 2002.

[7] Yannick Bidel, Nassim Zahzam, Alexandre Bresson, Cédric Blanchard, Malo Cadoret, Arne V Olesen, and René Forsberg. Absolute airborne gravimetry with a cold atom sensor. *Journal of Geodesy*, 94(2):20, 2020.

[8] Xuejian Wu, Zachary Pagel, Bola S Malek, Timothy H Nguyen, Fei Zi, Daniel S Scheirer, and Holger Müller. Gravity surveys using a mobile atom interferometer. *Science advances*, 5(9):eaax0800, 2019.

[9] A. Hinton, M. Perea-Ortiz, J. Winch, J. Briggs, S. Freer, D. Moustoukas, S. Powell-Gill, C. Squire, A. Lamb, C. Rammeloo, B. Stray, G. Voulazeris, L. Zhu, A. Kaushik, Y.-H. Lien, A. Niggebaum, A. Rodgers, A. Stabrawa, D. Boddice, S. R. Plant, G. W. Tuckwell, K. Bongs, N. Metje, and M. Holynski. A portable magneto-optical trap with prospects for atom interferometry in civil engineering. *Philosophical Transactions of the Royal Society A: Mathematical, Physical and Engineering Sciences*, 375(2099):20160238, 2017.

[10] D. S. Durfee, Y. K. Shaham, and M. A. Kasevich. Long-term stability of an area-reversible atom-interferometer sagnac gyroscope. *Physical Review Letters*, 97(24), December 2006.

[11] Achim Peters, Keng Yeow Chung, and Steven Chu. Measurement of gravitational acceleration by dropping atoms. *Nature*, 400(6747):849–852, August 1999.

[12] D. S. Weiss, B. C. Young, and S. Chu. Precision measurement of $\hbar/m_{Cs}$ based on photon recoil using laser-cooled atoms and atomic interferometry. *Applied Physics B Lasers and Optics*, 59(3):217–256, September 1994.

[13] Malo Cadoret, Estefania de Mirandes, Pierre Cladé, Saïda Guellati-Khélifa, Catherine Schwob, François Nez, Lucile Julien, and François Biraben. Combination of bloch oscillations with a ramsey-bordé interferometer: New determination of the fine structure constant. *Physical Review Letters*, 101(23), December 2008.

[14] D. Schlippert, J. Hartwig, H. Albers, L. L. Richardson, C. Schubert, A. Roura, W. P. Schleich, W. Ertmer, and E. M. Rasel. Quantum test of the universality of free fall. *Physical Review Letters*, 112(20), May 2014.

[15] Michael A Hohensee, Holger Müller, and RB Wiringa. Equivalence principle and bound kinetic energy. *Physical review letters*, 111(15):151102, 2013.

[16] Chris Overstreet, Peter Asenbaum, Tim Kovachy, Remy Notermans, Jason M. Hogan, and Mark A. Kasevich. Effective inertial frame in an atom interferometric test of the equivalence principle. *Phys. Rev. Lett.*, 120:183604, May 2018.

[17] Peter Asenbaum, Chris Overstreet, Minjeong Kim, Joseph Curti, and Mark A. Kasevich. Atom-interferometric test of the equivalence principle at the 10^{-12} level. *Phys. Rev. Lett.*, 125:191101, Nov 2020.

[18] Richard H Parker, Chenghui Yu, Weicheng Zhong, Brian Estey, and Holger Müller. Measurement of the fine-structure constant as a test of the standard model. *Science*, 360(6385):191–195, 2018.

[19] Jeffrey B Fixler, GT Foster, JM McGuirk, and MA Kasevich. Atom interferometer measurement of the newtonian constant of gravity. *Science*, 315(5808):74–77, 2007.

[20] G. Lamporesi, A. Bertoldi, L. Cacciapuoti, M. Prevedelli, and G. M. Tino. Determination of the newtonian gravitational constant using atom interferometry. *Phys. Rev. Lett.*, 100:050801, Feb 2008.

[21] G. Rosi, F. Sorrentino, L. Cacciapuoti, M. Prevedelli, and G. M. Tino. Precision measurement of the newtonian gravitational constant using cold atoms. *Nature*, 510(7506):518–521, June 2014.

[22] Matt Jaffe, Philipp Haslinger, Victoria Xu, Paul Hamilton, Amol Upadhye, Benjamin Elder, Justin Khoury, and Holger Müller. Testing sub-gravitational forces on atoms from a miniature in-vacuum source mass. *Nature Physics*, 13(10):938–942, 2017.

[23] D. O. Sabulsky, I. Dutta, E. A. Hinds, B. Elder, C. Burrage, and Edmund J. Copeland. Experiment to detect dark energy forces using atom interferometry. *Phys. Rev. Lett.*, 123:061102, Aug 2019.

[24] Savas Dimopoulos, Peter W. Graham, Jason M. Hogan, Mark A. Kasevich, and Surjeet Rajendran. Atomic gravitational wave interferometric sensor. *Physical Review D*, 78(12), December 2008.

[25] S Hild et al. Sensitivity studies for third-generation gravitational wave observatories. *Classical and Quantum Gravity*, 28(9):094013, April 2011.

[26] W. Chaibi, R. Geiger, B. Canuel, A. Bertoldi, A. Landragin, and P. Bouyer. Low frequency gravitational wave detection with ground-based atom interferometer arrays. *Physical Review D*, 93(2), January 2016.

[27] Peter W Graham, Jason M Hogan, Mark A Kasevich, Surjeet Rajendran, and Roger W Romani. Mid-band gravitational wave detection with precision atomic sensors. *arXiv preprint arXiv:1711.02225*, 2017.

[28] B. Canuel, S. Abend, P. Amaro-Seoane, F. Badaracco, Q. Beaufils, A. Bertoldi, K. Bongs, P. Bouyer, C. Braxmaier, W. Chaibi, N. Christensen, F. Fitzek, G. Flouris, N. Gaaloul, S. Gaffet, C. L. Garrido Alzar, R. Geiger, S. Guellati-Khelifa, K. Hammerer, J. Harms, J. Hinderer, J. Junca, S. Katsanevas, C. Klempt, C. Kozanitis, M. Krutzik, A. Landragin, I. Làzaro Roche, B. Leykauf, Y. H. Lien, S. Loriani, S. Merlet, M. Merzougui, M. Nofrarias, P. Papadakos, F. Pereira, A. Peters, D. Plexousakis, M. Prevedelli, E. Rasel, Y. Rogister, S. Rosat, A. Roura, D. O. Sabulsky, V. Schkolnik, D. Schlippert, C. Schubert, L. Sidorenkov, J. N. Siemß, C. F. Sopuerta, F. Sorrentino, C. Struckmann, G. M. Tino, G. Tsagkatakis, A. Viceré, W. von Klitzing, L. Woerner, and X. Zou. Elgar – a european laboratory for gravitation and atom-interferometric research, 2019.

[29] L. Badurina, E. Bentine, D. Blas, K. Bongs, D. Bortoletto, T. Bowcock, K. Bridges, W. Bowden, O. Buchmueller, C. Burrage, J. Coleman, G. Elertas, J. Ellis, C. Foot, V. Gibson, M.G. Haehnelt, T. Harte, S. Hedges, R. Hobson, M. Holynski, T. Jones, M. Langlois, S. Lellouch, M. Lewicki, R. Maiolino, P. Majewski, S. Malik, J. March-Russell, C. McCabe, D. Newbold, B. Sauer, U. Schneider, I. Shipsey, Y. Singh, M.A. Uchida, T. Valenzuela, M. van der Grinten, V. Vaskonen, J. Vossebeld, D. Weatherill, and I. Wilmut. Aion: an atom interferometer observatory and network. *Journal of Cosmology and Astroparticle Physics*, 2020(05):011–011, May 2020.

[30] Yousef Abou El-Neaj et al. AEDGE: Atomic experiment for dark matter and gravity exploration in space. *EPJ Quantum Technology*, 7(1), March 2020.

[31] Louis De Broglie. *Recherches sur la théorie des quanta*. PhD thesis, Migration-université en cours d'affectation, 1924.

[32] Mark Kasevich and Steven Chu. Atomic interferometry using stimulated raman transitions. *Physical Review Letters*, 67(2):181–184, July 1991.

[33] David M. Giltner, Roger W. McGowan, and Siu Au Lee. Atom interferometer based on bragg scattering from standing light waves. *Physical Review Letters*, 75(14):2638–2641, October 1995.

[34] A. Trimeche, M. Langlois, S. Merlet, and F. Pereira Dos Santos. Active control of laser wavefronts in atom interferometers. *Phys. Rev. Applied*, 7:034016, Mar 2017.

[35] Romain Karcher, Almazbek Imanaliev, Sébastien Merlet, and F Pereira Dos Santos. Improving the accuracy of atom interferometers with ultracold sources. *New Journal of Physics*, 20(11):113041, 2018.

[36] Min-kang Zhou, Qin Luo, Le-le Chen, Xiao-chun Duan, and Zhong-kun Hu. Observing the effect of wave-front aberrations in an atom interferometer by modulating the diameter of raman beams. *Phys. Rev. A*, 93:043610, Apr 2016.

[37] Vladimir Schkolnik, Bastian Leykauf, Matthias Hauth, Christian Freier, and Achim Peters. The effect of wavefront aberrations in atom interferometry. *Applied Physics B*, 120(2):311–316, 2015.

[38] Jason M Hogan, David MS Johnson, Susannah Dickerson, Tim Kovachy, Alex Sugarbaker, Sheng-wey Chiow, Peter W Graham, Mark A Kasevich, Babak Saif, Surjeet Rajendran, et al. An atomic gravitational wave interferometric sensor in low earth orbit (agis-leo). *General Relativity and Gravitation*, 43(7):1953–2009, 2011.

[39] J. M. McGuirk, M. J. Snadden, and M. A. Kasevich. Large area light-pulse atom interferometry. *Physical Review Letters*, 85(21):4498–4501, November 2000.

[40] L. Zhou, Z. Y. Xiong, W. Yang, B. Tang, W. C. Peng, K. Hao, R. B. Li, M. Liu, J. Wang, and M. S. Zhan. Development of an atom gravimeter and status of the 10-meter atom interferometer for precision gravity measurement. *General Relativity and Gravitation*, 43(7):1931–1942, Jul 2011.

[41] Sheng wey Chiow, Tim Kovachy, Jason M. Hogan, and Mark A. Kasevich. Generation of 43 w of quasi-continuous 780 nm laser light via high-efficiency, single-pass frequency doubling in periodically poled lithium niobate crystals. *Opt. Lett.*, 37(18):3861–3863, Sep 2012.

[42] Martina Gebbe, Jan-Niclas Siemß, Matthias Gersemann, Hauke Müntinga, Sven Herrmann, Claus Lämmerzahl, Holger Ahlers, Naceur Gaaloul, Christian Schubert, Klemens Hammerer, Sven Abend, and Ernst M. Rasel. Twin-lattice atom interferometry, 2020.

[43] Amnon Yariv. *Quantum Electronics*. John Wiley & Sons, Incorporated, 1975, 2 edition, 1975.

[44] Paul Hamilton, Matt Jaffe, Justin M. Brown, Lothar Maisenbacher, Brian Estey, and Holger Müller. Atom interferometry in an optical cavity. *Phys. Rev. Lett.*, 114:100405, Mar 2015.

[45] P. Hamilton, M. Jaffe, P. Haslinger, Q. Simmons, H. Müller, and J. Khoury. Atom-interferometry constraints on dark energy. *Science*, 349(6250):849–851, 2015.

[46] Matt Jaffe, Victoria Xu, Philipp Haslinger, Holger Müller, and Paul Hamilton. Efficient adiabatic spin-dependent kicks in an atom interferometer. *Phys. Rev. Lett.*, 121:040402, Jul 2018.

[47] Sofus L. Kristensen, Matt Jaffe, Victoria Xu, Cristian D. Panda, and Holger Müller. Raman transitions driven by phase-modulated light in a cavity atom interferometer. *arXiv physics.atom-ph*, 2020.

[48] Victoria Xu, Matt Jaffe, Cristian D. Panda, Sofus L. Kristensen, Logan W. Clark, and Holger Müller. Probing gravity by holding atoms for 20 seconds. *Science*, 366(6466):745–749, 2019.

[49] I Riou, N Mielec, G Lefèvre, M Prevedelli, A Landragin, P Bouyer, A Bertoldi, R Geiger, and B Canuel. A marginally stable optical resonator for enhanced atom interferometry. *Journal of Physics B: Atomic, Molecular and Optical Physics*, 50(15):155002, jul 2017.

[50] M. Dovale-Álvarez, D. D. Brown, A. W. Jones, C. M. Mow-Lowry, H. Miao, and A. Freise. Fundamental limitations of cavity-assisted atom interferometry. *Phys. Rev. A*, 96:053820, Nov 2017.

[51] Miguel Dovale Álvarez. *Optical cavities for optical atomic clocks, atom interferometry and gravitational-wave detection*. Springer, 2019.

[52] Holger Müller, Sheng wey Chiow, Quan Long, Sven Herrmann, and Steven Chu. Atom interferometry with up to 24-photon-momentum-transfer beam splitters. *Physical Review Letters*, 100(18), May 2008.

[53] Sheng wey Chiow, Tim Kovachy, Hui-Chun Chien, and Mark A. Kasevich. $102\hbar$kLarge area atom interferometers. *Physical Review Letters*, 107(13), September 2011.

[54] Tim Kovachy, Sheng-wey Chiow, and Mark A. Kasevich. Adiabatic-rapid-passage multiphoton bragg atom optics. *Phys. Rev. A*, 86:011606, Jul 2012.

[55] Holger Müller, Sheng-wey Chiow, Sven Herrmann, and Steven Chu. Atom interferometers with scalable enclosed area. *Phys. Rev. Lett.*, 102:240403, Jun 2009.

[56] Martin Weitz, Brenton C. Young, and Steven Chu. Atomic interferometer based on adiabatic population transfer. *Phys. Rev. Lett.*, 73:2563–2566, Nov 1994.

[57] Christopher J. Foot. *Atomic physics*, volume 7. Oxford University Press, 2005.

[58] C. Antoine. Matter wave beam splitters in gravito-inertial and trapping potentials: generalized ttt scheme for atom interferometry. *Applied Physics B*, 84(4):585–597, Sep 2006.

[59] E Rocco, R N Palmer, T Valenzuela, V Boyer, A Freise, and K Bongs. Fluorescence detection at the atom shot noise limit for atom interferometry. *New Journal of Physics*, 16(9):093046, sep 2014.

[60] Xinan Wu. *Gravity gradient survey with a mobile atom interferometer*. PhD thesis, Stanford University, 2009. Chapter 3.2.

[61] Hermann Haken and Hans Christoph Wolf. *Atomic and quantum physics: an introduction to the fundamentals of experiment and theory*. Springer Science & Business Media, second edition edition, 1987.

[62] Peter W. Graham, Jason M. Hogan, Mark A. Kasevich, and Surjeet Rajendran. New method for gravitational wave detection with atomic sensors. *Physical Review Letters*, 110(17), Apr 2013.

[63] Takayuki Kurosu and Fujio Shimizu. Laser cooling and trapping of calcium and strontium. *Japanese Journal of Applied Physics*, 29(Part 2, No. 11):L2127–L2129, nov 1990.

[64] S. L. Campbell, R. B. Hutson, G. E. Marti, A. Goban, N. Darkwah Oppong, R. L. McNally, L. Sonderhouse, J. M. Robinson, W. Zhang, B. J. Bloom, and J. Ye. A fermi-degenerate three-dimensional optical lattice clock. *Science*, 358(6359):90–94, 2017.

[65] Liang Hu, Nicola Poli, Leonardo Salvi, and Guglielmo M. Tino. Atom interferometry with the sr optical clock transition. *Phys. Rev. Lett.*, 119:263601, Dec 2017.

[66] Robin Santra, Kevin V. Christ, and Chris H. Greene. Properties of metastable alkaline-earth-metal atoms calculated using an accurate effective core potential. *Physical Review A*, 69(4), April 2004.

[67] Sergey G. Porsev and Andrei Derevianko. Hyperfine quenching of the metastable $^3p_{0,2}$ states in divalent atoms. *Phys. Rev. A*, 69:042506, Apr 2004.

[68] Martin M Boyd. *High Precision Spectroscopy of Strontium in an Optical Lattice: Towards a New Standard for Frequency and Time*. PhD thesis, University of Colorado, 2007.

[69] Liang Hu, Enlong Wang, Leonardo Salvi, Jonathan N Tinsley, Guglielmo M Tino, and Nicola Poli. Sr atom interferometry with the optical clock transition as a gravimeter and a gravity gradiometer. *Classical and Quantum Gravity*, 37(1):014001, nov 2019.

[70] SS Sané, S Bennetts, JE Debs, CCN Kuhn, GD McDonald, PA Altin, JD Close, and NP Robins. 11 w narrow linewidth laser source at 780nm for laser cooling and manipulation of rubidium. *Optics express*, 20(8):8915–8919, 2012.

[71] Jan Rudolph, Thomas Wilkason, Megan Nantel, Hunter Swan, Connor M. Holland, Yijun Jiang, Benjamin E. Garber, Samuel P. Carman, and Jason M. Hogan. Large momentum transfer clock atom interferometry on the 689 nm intercombination line of strontium. *Phys. Rev. Lett.*, 124:083604, Feb 2020.

[72] C. J. Ballance, T. P. Harty, N. M. Linke, M. A. Sepiol, and D. M. Lucas. High-fidelity quantum logic gates using trapped-ion hyperfine qubits. *Phys. Rev. Lett.*, 117:060504, Aug 2016.

[73] Rodney Loudon. *The Quantum Theory of Light*. Clarendon Press, Oxford, 1973.

[74] R. Ozeri, C. Langer, J. D. Jost, B. DeMarco, A. Ben-Kish, B. R. Blakestad, J. Britton, J. Chiaverini, W. M. Itano, D. B. Hume, D. Leibfried, T. Rosenband, P. O. Schmidt, and D. J. Wineland. Hyperfine coherence in the presence of spontaneous photon scattering. *Phys. Rev. Lett.*, 95:030403, Jul 2005.

[75] R. A. Cline, J. D. Miller, M. R. Matthews, and D. J. Heinzen. Spin relaxation of optically trapped atoms by light scattering. *Opt. Lett.*, 19(3):207–209, Feb 1994.

[76] Akash V Rakholia, Hayden J McGuinness, and Grant W Biedermann. Dual-axis high-data-rate atom interferometer via cold ensemble exchange. *Physical Review Applied*, 2(5):054012, 2014.

[77] Mark Kasevich, David S Weiss, Erling Riis, Kathryn Moler, Steven Kasapi, and Steven Chu. Atomic velocity selection using stimulated raman transitions. *Physical review letters*, 66(18):2297, 1991.

[78] Harold J Metcalf and Peter Van der Straten. *Laser Cooling and Trapping.* Springer, 1999.

[79] Malte Schmidt. *A mobile high-precision gravimeter based on atom interferometry.* PhD thesis, Humboldt-Universität zu Berlin, Mathematisch-Naturwissenschaftliche Fakultät I, 2011.

[80] Hayden J McGuinness, Akash V Rakholia, and Grant W Biedermann. High data-rate atom interferometer for measuring acceleration. *Applied Physics Letters*, 100(1):011106, 2012.

[81] Quentin Bodart, Sébastien Merlet, Nicola Malossi, F Pereira Dos Santos, Philippe Bouyer, and Arnaud Landragin. A cold atom pyramidal gravimeter with a single laser beam. *Applied Physics Letters*, 96(13):134101, 2010.

[82] Sheng-wey Chiow, Tim Kovachy, Hui-Chun Chien, and Mark A Kasevich. $102\hbar k$ large area atom interferometers. *Physical review letters*, 107(13):130403, 2011.

[83] Anthony E Siegman. *Lasers.* University Science Books, 1986.

[84] Alexander Franzen. Component library. `http://www.gwoptics.org/ComponentLibrary/`. Licensed under a Creative Commons Attribution-NonCommercial 3.0 Unported License.

[85] H. Kogelnik and T. Li. Laser beams and resonators. *Appl. Opt.*, 5(10):1550–1567, Oct 1966.

[86] Koji Arai. On the accumulated round-trip gouy phase shift for a general optical cavity. *LIGO Technical Note*, 1300189:1–11, 2013.

[87] Cavitysim: a simple python package for cavity simulation. `https://doi.org/10.5281/zenodo.4884676`.

[88] Rustin Nourshargh. Frequency control of orthogonal polarisation modes in an optical cavity, August 2020. UK Patent Application No. GB2012043.2.

[89] Min-Kang Zhou, Le-Le Chen, Qin Luo, Ke Zhang, Xiao-Chun Duan, and Zhong-Kun Hu. Effect of the gaussian distribution of both atomic cloud and laser intensity in an atom gravimeter. *Phys. Rev. A*, 93:053615, May 2016.

[90] T. W. Hänsch. Repetitively pulsed tunable dye laser for high resolution spectroscopy. *Appl. Opt.*, 11(4):895–898, Apr 1972.

[91] Donatella Fiorucci, Ali Hreibi, and Walid Chaibi. Telescope-based cavity for negative ion beam neutralization in future fusion reactors. *Appl. Opt.*, 57(7):B122–B134, Mar 2018.

[92] Eric D. Black. An introduction to pound–drever–hall laser frequency stabilization. *American Journal of Physics*, 69(1):79–87, 2001.

[93] Olivier Carraz, Renée Charrière, Malo Cadoret, Nassim Zahzam, Yannick Bidel, and Alexandre Bresson. Phase shift in an atom interferometer induced by the additional laser lines of a raman laser generated by modulation. *Phys. Rev. A*, 86:033605, Sep 2012.

[94] Yaoting Wang, Ruihong Zhang, Wujun Li, Boyang Li, Wenjia Shi, and Yanchao Zhang. Experimental investigation on the eliminating astigmatism in off-axis parabolic mirror ring cavity. *Optics & Laser Technology*, 109:348 – 351, 2019.

[95] K. Dupraz, K. Cassou, A. Martens, and F. Zomer. The abcd matrix for parabolic reflectors and its application to astigmatism free four-mirror cavities. *Optics Communications*, 353:178 – 183, 2015.

[96] Robert W Boyd. *Nonlinear optics.* Academic press, 3 edition, 2008.

[97] Mark Fox. *Optical Properties of Solids.* Oxford University Press, 2 edition, 2008.

[98] Christopher C Davis. *Lasers and electro-optics: fundamentals and engineering.* Cambridge university press, 2 edition, 2014.

[99] T Kovachy, P Asenbaum, C Overstreet, CA Donnelly, SM Dickerson, A Sugarbaker, JM Hogan, and MA Kasevich. Quantum superposition at the half-metre scale. *Nature*, 528(7583):530, 2015.

[100] B Sathyaprakash et al. Scientific objectives of einstein telescope. *Classical and Quantum Gravity*, 29(12):124013, June 2012.

[101] J Aasi et al. Advanced LIGO. *Classical and Quantum Gravity*, 32(7):074001, March 2015.

[102] F Acernese et al. Advanced virgo: a second-generation interferometric gravitational wave detector. *Classical and Quantum Gravity*, 32(2):024001, December 2014.

[103] Asimina Arvanitaki, Peter W. Graham, Jason M. Hogan, Surjeet Rajendran, and Ken Van Tilburg. Search for light scalar dark matter with atomic gravitational wave detectors. *Physical Review D*, 97(7), April 2018.

[104] Peter W. Graham, Jason M. Hogan, Mark A. Kasevich, and Surjeet Rajendran. Resonant mode for gravitational wave detectors based on atom interferometry. *Phys. Rev. D*, 94:104022, Nov 2016.

[105] S. Abend, M. Gebbe, M. Gersemann, H. Ahlers, H. Müntinga, E. Giese, N. Gaaloul, C. Schubert, C. Lämmerzahl, W. Ertmer, W. P. Schleich, and E. M. Rasel. Atom-chip fountain gravimeter. *Physical Review Letters*, 117(20), November 2016.

[106] G. D. McDonald, C. C. N. Kuhn, S. Bennetts, J. E. Debs, K. S. Hardman, M. Johnsson, J. D. Close, and N. P. Robins. $80\hbar k$ momentum separation with bloch oscillations in an optically guided atom interferometer. *Physical Review A*, 88(5), November 2013.

[107] T. Mazzoni, X. Zhang, R. Del Aguila, L. Salvi, N. Poli, and G. M. Tino. Large-momentum-transfer bragg interferometer with strontium atoms. *Physical Review A*, 92(5), November 2015.

[108] Ichiro Ushijima, Masao Takamoto, Manoj Das, Takuya Ohkubo, and Hidetoshi Katori. Cryogenic optical lattice clocks. *Nature Photonics*, 9(3):185–189, February 2015.

[109] B. J. Bloom, T. L. Nicholson, J. R. Williams, S. L. Campbell, M. Bishof, X. Zhang, W. Zhang, S. L. Bromley, and J. Ye. An optical lattice clock with accuracy and stability at the 10-18 level. *Nature*, 506(7486):71–75, January 2014.

[110] T. L. Nicholson, S. L. Campbell, R. B. Hutson, G. E. Marti, B. J. Bloom, R. L. McNally, W. Zhang, M. D. Barrett, M. S. Safronova, G. F. Strouse, W. L. Tew, and J. Ye. Systematic evaluation of an atomic clock at 2×10^{-18} total uncertainty. *Nature Communications*, 6(1):6896, Apr 2015.

[111] Isao Tomita, Hiroaki Sanjoh, Eiichi Yamada, Hiroyuki Suzuki, and Yuzo Yoshikuni. Theoretical analysis of the generation of multiple wavelengths by pulsed serrodyne modulation. *Journal of Optics A: Pure and Applied Optics*, 7(12):701–705, oct 2005.

[112] Anthony Immarco, Mark A Steinhacker, Richard J Proebstl, and Harold M Stahl. Electro-optic q-switch using brewster angle cut pockels cell, February 16 1971. US Patent 3,564,450.

[113] Nitzan Akerman, Nir Navon, Shlomi Kotler, Yinnon Glickman, and Roee Ozeri. Universal gate-set for trapped-ion qubits using a narrow linewidth diode laser. *New Journal of Physics*, 17(11):113060, nov 2015.

[114] David P. Nadlinger. Entanglement between trapped strontium ions and photons. Master's thesis, ETH Zürich, 2016.

[115] Andrew D. Ludlow, Martin M. Boyd, Tanya Zelevinsky, Seth M. Foreman, Sebastian Blatt, Mark Notcutt, Tetsuya Ido, and Jun Ye. Systematic study of the ^{87}Sr clock transition in an optical lattice. *Phys. Rev. Lett.*, 96:033003, Jan 2006.

[116] F. et al. Acernese. Laser with an in-loop relative frequency stability of 1.0×10^{-21} on a 100-ms time scale for gravitational-wave detection. *Phys. Rev. A*, 79:053824, May 2009.

[117] Elizabeth A. Cummings, Malcolm S. Hicken, and Scott D. Bergeson. Demonstration of a 1-w injection-locked continuous-wave titanium:sapphire laser. *Appl. Opt.*, 41(36):7583–7587, Dec 2002.

[118] Susannah M. Dickerson, Jason M. Hogan, Alex Sugarbaker, David M. S. Johnson, and Mark A. Kasevich. Multiaxis inertial sensing with long-time point source atom interferometry. *Phys. Rev. Lett.*, 111:083001, Aug 2013.

[119] Grtschnk. Remove ir-filter from microsoft's hd 3000 webcam, Sep 2017.

[120] LLC G&H Ohio. Pockels cell alignment for single pass systems, 2012.

[121] Daniel A Steck. Rubidium 87 d line data, (revision 2.1. 5, 13 january 2015). `http://steck.us/alkalidata`, 2001.

[122] Akash Rakholia. *High Data-Rate Atom Interferometry for Measuring Dynamic Inertial Conditions.* PhD thesis, The University of New Mexico, 2015.

[123] Jeffrey Michael McGuirk. *High precision absolute gravity gradiometry with atom interferometry.* PhD thesis, PhD thesis, Stanford University, 2001.

[124] GD Boyd and DA Kleinman. Parametric interaction of focused gaussian light beams. *Journal of Applied Physics*, 39(8):3597–3639, 1968.

[125] Anthony E Siegman. *Lasers.* Chapter 17.1, Page 669, University Science Books, 1986.

[126] Daniel A Steck. Rubidium 85 d line data, (revision 2.1.6, 20 september 2013). `http://steck.us/alkalidata`, 2008.

[127] Theodor W Hänsch and Arthur L Schawlow. Cooling of gases by laser radiation. *Optics Communications*, 13(1):68–69, 1975.

[128] Alan L Migdall, John V Prodan, William D Phillips, Thomas H Bergeman, and Harold J Metcalf. First observation of magnetically trapped neutral atoms. *Physical Review Letters*, 54(24):2596, 1985.

[129] Steven Chu, Leo Hollberg, John E Bjorkholm, Alex Cable, and Arthur Ashkin. Three-dimensional viscous confinement and cooling of atoms by resonance radiation pressure. *Physical review letters*, 55(1):48, 1985.

[130] EL Raab, M Prentiss, Alex Cable, Steven Chu, and David E Pritchard. Trapping of neutral sodium atoms with radiation pressure. *Physical Review Letters*, 59(23):2631, 1987.

[131] Harold Metcalf. Magneto-optical trapping and its application to helium metastables. *JOSA B*, 6(11):2206–2210, 1989.

[132] C Chesman, EG Lima, FAM De Oliveira, SS Vianna, and JWR Tabosa. Two-and four-beam magneto-optical trapping of neutral atoms. *Optics letters*, 19(16):1237–1239, 1994.

[133] Jeffrey Michael Mcguirk, GT Foster, JB Fixler, MJ Snadden, and MA Kasevich. Sensitive absolute-gravity gradiometry using atom interferometry. *Physical Review A*, 65(3):033608, 2002.

[134] Yuan-Yu Jau and Jongmin Lee. Microfabricated waveguide atom traps. *Sandia National Laboratories*, 2017.

[135] E. Vetsch, D. Reitz, G. Sagué, R. Schmidt, S. T. Dawkins, and A. Rauschenbeutel. Optical interface created by laser-cooled atoms trapped in the evanescent field surrounding an optical nanofiber. *Phys. Rev. Lett.*, 104:203603, May 2010.

[136] A. Goban, K. S. Choi, D. J. Alton, D. Ding, C. Lacroûte, M. Pototschnig, T. Thiele, N. P. Stern, and H. J. Kimble. Demonstration of a state-insensitive, compensated nanofiber trap. *Phys. Rev. Lett.*, 109:033603, Jul 2012.

[137] Xinye Xu, V. G. Minogin, Kwanil Lee, Yuzhu Wang, and Wonho Jhe. Guiding cold atoms in a hollow laser beam. *Phys. Rev. A*, 60:4796–4804, Dec 1999.

[138] S. J. M. Kuppens, K. L. Corwin, K. W. Miller, T. E. Chupp, and C. E. Wieman. Loading an optical dipole trap. *Phys. Rev. A*, 62:013406, Jun 2000.

[139] Gregory W Hoth, Elizabeth A Donley, and John Kitching. Atom number in magneto-optic traps with millimeter scale laser beams. *Optics letters*, 38(5):661–663, 2013.